Fabrication and Design of Hybrid Monolithic Shape Memory Alloy Actuators

by

D. Ryan Walker

A thesis
presented to the University of Waterloo
in fulfillment of the
thesis requirement for the degree of
Master of Applied Science
in
Mechanical Engineering

Waterloo, Ontario, Canada, 2008

I hereby declare that I am the sole author of this thesis. This is a true copy of the thesis, including any required final revisions, as accepted by my examiners.

I understand that my thesis may be made electronically available to the public.

D. Ryan Walker

Abstract

Shape memory alloys (SMA) offer several advantages over traditional electro-mechanical devices, including: smooth, silent, clean operation; linear actuation; high power/weight ratio; scalability; and reduced part counts. These unique characteristics make them an attractive option when developing actuators, particularly at the meso- and micro-scales. However, SMAs do not typically display cyclic actuation and, therefore, require some reset force or bias mechanism in order to achieve this behaviour. Additionally, the micro-assembly of SMA material with a reset mechanism becomes increasingly difficult as the dimensions of actuators are scaled down. Therefore, actuators have been developed in which the actuation and reset mechanism are fabricated from a single piece of material. These actuators are referred to as *monolithic actuators*.

Monolithic actuators are fabricated from a single piece of SMA material in which local annealing is used to selectively impart the shape memory effect (SME), while the remainder of the material acts as the bias mechanism. This work proposes an extension to monolithic actuators that locally varies the material composition of the monolithic component to exhibit different mechanical properties in select regions. This eliminates the need for local annealing by introducing regions of material unaffected by the annealing process. Additionally, incorporating regions of superelastic material to act as the bias mechanism greatly increases the actuator's range of motion. These actuators are referred to as *hybrid monolithic actuators*.

The creation of hybrid monolithic SMA actuators requires the development of both a fabrication technique and design tool. Varying the composition locally is accomplished by utilizing powder metallurgy fabrication techniques, specifically tape casting. Tapes of different compositions are cut, stacked, and sintered resulting in a monolithic component with mechanical properties that

vary spatially. Tape casting NiTi from elemental powders is studied in this work, and tape recipes and sintering profiles are developed.

In order to model the SMA behaviour of complex geometries, a finite element implementation of an existing lumped-element SMA model is developed. This model is used to design and simulate a prototype hybrid monolithic actuator. The prototype is fabricated and its performance used to illustrate the advantages of hybrid design over typical monolithic actuators.

Acknowledgements

I would like to thank my supervisor, Professor Robert B.Gorbet for his guidance, support, and valuable feedback throughout my graduate research and education experience. I would also like to thank Professor Stephen Corbin for his valuable advice on my research and Professor Hamid Jahed for reviewing this thesis. Funding of this research was provided by Ontario Centres of Excellence and INCO.

My appreciation goes to my fellow colleagues and friends who supported me both at the university and during my free time. Without them the past few years would not have been as memorable as they were.

Finally, I am grateful for the support given to me by my parents over my entire university career.

Table of Contents

List of Figures

List of Tables

Chapter 1

Introduction

1.1 Motivation

Shape memory alloys (SMA) offer several advantages over traditional electro-mechanical devices: smooth, silent, clean operation; linear actuation; high power/weight ratio; scalability; and reduced part counts. These properties make SMAs an attractive option when developing actuators at the meso- and micro-scales, particularly their high power/weight ratio, scalability, and higher actuator bandwidth due to their increased surface area to volume ratio.

Much attention has been given to the fabrication of NiTi SMA actuators at the micro-scale level. Traditional micro-electromechanical system (MEMS) fabrication techniques, such as vapour deposition and sputtering, have proven adequate in the formation of NiTi devices. However, at the meso-scale[1] the fabrication of SMA actuators remains a challenge. At these scales, MEMS fabrication techniques are no longer viable and existing bulk NiTi forms, such as springs and wires, prove difficult or impossible to use. Of particular difficulty are the mechanical connections required for the assembly of the reset force mechanisms necessary in typical SMA actuator designs. The assembly of actuation and reset force mechanisms requires a high level of precision in order to achieve the required accuracy and actuator strain. Despite such draw backs, the high energy density of SMAs make them one of the only viable options for actuation within increasingly miniature

[1] Meso, meaning "in the middle", denotes here dimensions between "macro-scale" and "micro-scale" (MEMS) devices, typically on the order of a few millimeters.

devices. One example is the next generation of ingestible medical devices for capsule endoscopy. Current devices offer only a passive journey through the digestive tract with no control over position, orientation, or rate of travel. If these devices could stop, rotate, or crawl within the intestinal tract it would be a great improvement. With the volume constraints imposed by the ingestible capsule, SMAs are often proposed as a possible solution to the problem. For example, Menciassi et al. [1] proposed a clamping device for immobilizing a capsule in the gastrointestinal tract using a compliant clamp actuated by discrete SMA wires (Figure 1). Menciassi et al. [2] also proposed SMA-actuated "legs" which are again actuated by discrete SMA wires routed over several tiny pulleys, shown in Figure 2.

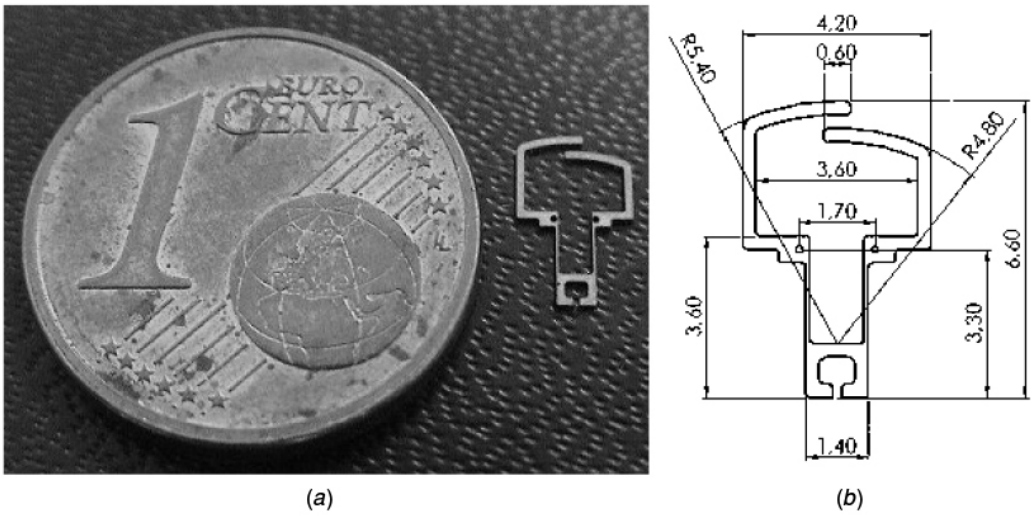

Figure 1: Prototype for the gripper (a), and dimensions (in mm) (b). [1]

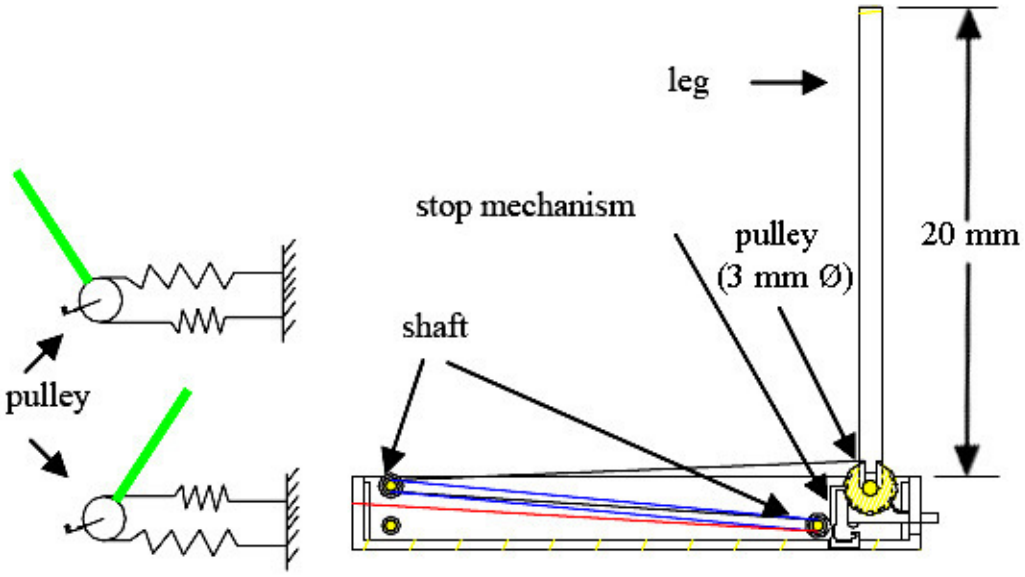

Figure 2: SMA leg actuation. Working principle (left). Design of the SMA wire-based actuator and the leg (right). [2]

The long term motivation of this research is to develop design and fabrication techniques for hybrid monolithic meso-scale SMA actuators. Monolithic actuators are those in which the actuation and reset force mechanism are fabricated from a single piece of material, thus eliminating the difficulty of micro-mechanical connections and assembly. Such actuators exist, however their range of motion is minimal in comparison to that achievable by SMAs [3] [4]. Powder metallurgy fabrication techniques, specifically tape casting, allow the creation of monolithic actuators with regions of various material compositions. Such actuators can potentially extend the capabilities, particularly range of motion, of current monolithic designs as regions of material are not limited to a single SMA composition. The incorporation of superelastic SMA regions greatly increases the range of recoverable strain of the reset force mechanism. This idea will be referred to as hybrid monolithic SMA actuators, and will be discussed in detail in Chapter 5 of this thesis.

1.2 Goals

The long-term goal of this research is to improve upon current meso-scale SMA actuators through the development of a hybrid monolithic SMA actuator. In order to achieve this goal, it is first necessary to develop the tools required for the actuator's design and fabrication. Therefore, this research can be broken down into three major aspects:

- **Material Fabrication:** The approach investigated in this thesis is a powder metallurgy (PM) fabrication technique, with a specific focus on tape casting. This work aims to develop a greater understanding of the technique, and its potential to create monolithic components with varying material compositions, referred to here as hybrid components.
- **Development of Design Tools:** Lumped-element techniques used by previous students for modeling SMAs are inadequate for handling more complex geometries, modes of actuation, and hybrid compositions. A finite element (FE) implementation of an existing lumped-model is to be developed utilizing the COMSOL Multiphysics software package.
- **Actuator Design:** Using the knowledge obtained from the PM fabrication investigation and the developed FE modeling tool, a prototype hybrid monolithic actuator is to be designed and built. The design is to be based on a previous actuator design, with the intent of illustrating the improvements made possible by the implementation of hybrid design techniques.

The advancement of PM fabrication of NiTi and the development of a FE model are not only necessary for the design of the hybrid monolithic actuator proposed in this research, but on their own stand to further the development of NiTi devices. This introduces a secondary goal to this research,

which is to develop tools for the future design of NiTi SMA devices. The above goals are discussed in detail in their respective chapters of this thesis.

1.3 Scope

The scope of this thesis is to introduce the idea of hybrid monolithic actuators and provide sufficient evidence to their feasibility and potential advantages over current monolithic designs. Future research is necessary in order to fully understand and refine the PM tape casting techniques in order to produce NiTi with material properties comparable to those obtained from conventional fabrication techniques. Additionally, alternative modeling and design techniques with improved usability and flexibility are necessary for the development of more complex hybrid monolithic actuator designs.

1.4 Overview

This work introduces the concept and outlines the development of a hybrid monolithic shape memory alloy (SMA) actuator. Following this introductory chapter, the thesis is outlined as follows.

- Chapter 2 provides background information and related work on the behaviour, fabrication, modeling, and design of SMAs and SMA actuators.
- Chapter 3 details the development of a powder metallurgy tape casting fabrication technique for the creation of NiTi based hybrid monolithic actuators. Tape recipes and sintering profiles are developed and the resulting specimens analyzed.
- Chapter 4 details a finite element modeling technique for the design and simulation of SMAs and SMA actuators. The model is developed and validated with experimental data.

- Chapter 5 introduces the concept of hybrid monolithic actuators, including a discussion of their advantages and unique design. A prototype is designed and fabricated to illustrate the advantages of hybrid actuators.
- Finally, Chapter 6 details the conclusions.

Chapter 2

Background

The following sections provide a detailed background of shape memory alloys (SMAs) and the shape memory effect (SME). Both the microscopic origins and the macroscopic behaviour is discussed, as well as their complex non-linear stress-strain-temperature relationships. Additionally, fabrication methods of SMAs are discussed with a focus on powder metallurgy (PM) and tape casting technologies. Finally, background is provided on current SMA lumped model and finite element (FE) modeling techniques.

2.1 Shape Memory Alloys

Shape memory alloys are a class of materials that, when processed appropriately, exhibit what is known as the shape memory effect. This effect, in general, allows the material to recover its initial shape after plastic deformation. Shape recovery is done by heating the SMA material above a transformation temperature predetermined by the material composition and processing history. SMAs with transformation temperatures above their operating temperature (often room temperature) exhibit the SME described above. SMAs with transformation temperatures below operating temperature exhibit what is known as pseudoelasticity, or sometimes called superelasticity, and are referred to as superelastic. SMAs in the superelastic state are capable of recovering their previous shape after the removal of even relatively high applied strains. This differs from the SME in that the

deformation from an applied load is not plastic and shape recovery is achieved isothermally on unloading.

Due to their unique properties, SMAs have become an attractive solution for applications where conventional actuators cannot provide the desired operation characteristics. They are lightweight, powerful, scalable, and offer smooth, silent, clean operation. These unique properties make SMA actuators ideal for motion generation at the meso- and micro-scales. Conventional actuator technologies are unable to match the high power to weight ratio offered by SMAs. A comparison of various actuator technologies is provided schematically in Figure 3.

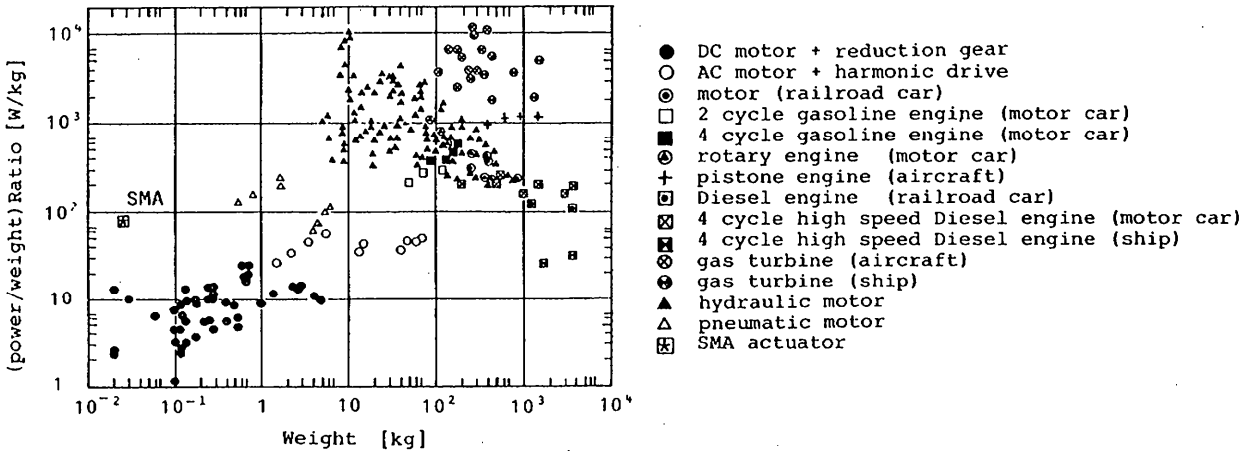

Figure 3: Power density versus power/weight ratio of several actuators [5]

Several alloys have been discovered that exhibit the shape memory effect [6], and are summarized in Table 1 below. The majority of these alloys can be generalized into three major categories: Ni-Ti-based, Cu-based, and those containing precious metals. Of these alloys, only the Cu-Zn-Al, Cu-Al-Ni, and Ni-Ti alloys are presently of commercial importance [6]. Ni-Ti-based alloys have gained much attention due to their relatively high electrical resistance, better shape

memory properties, and better corrosion resistance in comparison to Cu-based alloys [6]. Despite the higher cost of NiTi-based alloys in comparison to Cu-based alloys, they are still less expensive than those alloys containing precious metals. Their higher electrical resistance, in comparison to Cu-based alloys, allows them to be Joule heated by passing electrical current through the actuator, giving them a significant advantage over other SMA alternatives in actuator applications. Additionally, despite its nickel content, NiTi is a biocompatible material exhibiting good corrosion properties and low cytotoxicity, thereby lending its actuation capabilities for applications within the medical field [7].

Table 1: Alloys exhibiting the shape memory effect [6]

Alloy	Austenite Structure
Au-Cd	B2
Cu-Zn	B2
In-Ti	FCC
Ni-Ti	B2
Cu-Zn-Al	B2, DO_3
Ti-Nb	BCC (disordered)
Au-Cu-Zn	No data
Cu-Zn-Sn	B2
Cu-Zn-Si	B2
Cu-Al-Ni	DO_3
Ag-Cd	No data
Cu-Sn	B2
Cu-Zn-Ga	B2
Ni-Al	B2
Fe-Pt	LI_2
U-Nb	BCC (disordered)
Ti-Pd-Ni	B2
Fe-Mn-Si	FCC (disordered)

The following sections of this thesis detail the properties of SMAs on both the micro- and macroscopic scale and how these properties make them an ideal choice for the development of meso-scale actuators.

2.2 Shape Memory Effect

2.2.1 One-way Shape Memory Effect

The SME allows an alloy to return to its previous shape after undergoing plastic deformation by heating it above its transformation temperature. Typically, bulk material undergoes cold working in order to produce products of particular shapes and sizes [8]. This processing leaves the material in a cold-worked state wherein its mechanical properties are altered and the alloy does not exhibit the SME [3]. Therefore, before an alloy capable of exhibiting this effect can achieve this behaviour it must first undergo a heat treatment process. This process has been studied extensively [9], and for this particular research the process described in [10] is used.

The heat treatment is necessary for undoing the cold work imparted on the material during fabrication and recovering the material's SME capability. This process is also known as shape-setting or training since the geometry of the component during the heat treatment is that which an unconstrained material will return to at temperatures above its transformation temperature. To achieve the desired "memorized" geometry the material must be constrained to this particular shape during the heat treatment. This research will cover in detail both the advantages and disadvantages of this process when it comes to the design of monolithic actuators.

Typically the heat treatment brings the constrained material to a peak temperature of 450^{o}C to 550^{o}C, holds it at this temperature, then rapidly cools it back to room temperature. The peak hold time is decided by the size and geometry of the component and die used for dimensional constraint. The hold time ensures the entire component reaches the desired temperature. Rapid cooling is typically achieved by a water quench. Heating methods include the use of an air or vacuum furnace, salt bath, sand bath, heated die, or laser. The method used is determined by the size of the SMA

component, its function, and equipment availability. Variations in the peak hold temperature have been shown to have an effect on the tensile strength of the finished material [9].

2.2.2 Two-way Shape Memory Effect

The two-way shape memory effect (TWSM) differs from the one-way shape memory effect in that there is a spontaneous shape change on cooling as well as on heating. In effect, the material remembers both a high temperature shape and a low temperature shape. In order to achieve the two-way behaviour the material must undergo a special thermomechanical treatment [6] wherein micro-stresses are introduced in the material. These micro-stresses bias the nucleation and growth of martensite causing some variants to form preferentially [6].

This phenomenon may appear preferable to the one-way shape memory effect in that it has two memorized geometries and thus is capable of performing cyclic actuation. However, the TWSM has several disadvantages in comparison to the one-way shape memory effect, such as a limited reversible strain in the range of 2%, and lower transformation forces on cooling [6]. Due to the reduced performance of the SME in TWSM materials and the additional processing necessary to set up the material, this work will focus solely on the one-way shape memory effect.

2.3 Shape Memory Alloy Microscopic Behaviour

The SME is made possible by a SMA's ability to exist in three distinct crystallographic structures: martensite, austenite, and R-phase. Which phase exists at any given time is determined by the material temperature, stress, and temperature-stress history. It is the transitions between the weaker martensite phase, and the stiffer austenite phase at the microscopic level that are responsible for the

SME at the macroscopic scale. The various phases and crystallographic structures that make possible the unique properties of SMAs will be discussed in the following sections.

2.3.1 Austenite Phase

The austenite phase of NiTi is often referred to as having a body-centred cubic (BCC) structure; however, technically it is not BCC and instead has what is known as a B2 structure with body centred symmetry [6]. The B2 austenite structure of NiTi consists of Ti atoms situated at the vertices of the cube with a single Ni atom in the centre. Figure 4 provides a two-dimensional representation of the NiTi austenite phase with the Ti atoms represented as dark circles, and the Ni as light circles. An important property of the B2 austenite structure is that its highly symmetric lattice is inherently univariant [11], meaning it can only exist in one distinct crystallographic structure.

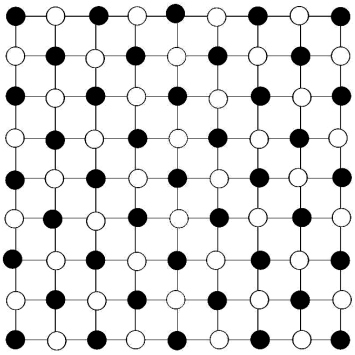

Figure 4: Two-dimensional representation of B2 structure in austenitic NiTi

2.3.2 Martensite Phase

SMAs at low temperatures exist in the martensite phase which has a monoclinic lattice structure [11]. Martensite is formed by a displacive athermal transformation upon cooling from the higher temperature austenite phase under low or no stress [6]. The displacive athermal transformation refers

to one in which atoms are cooperatively rearranged into a new more stable structure, without a change in the chemical nature of the material, and progresses in a time-independent fashion [6]. When the new phase is formed an accommodation method must exist that allows the preservation of the external macroscopic dimensions of the material [6] [11]. In SMAs this accommodation is achieved by a mechanism known as twinning, which is capable of accommodating shape changes in a reversible way [6]. Figure 5 provides two-dimensional schematics of the various states of martensite. In three dimensions the situations are more complex, and monoclinic martensite can exist in 24 variants as opposed to the two variants shown in Figure 5. Martensite can also be formed by the application of stress to a material in the austenite phase [11]. At some critical level of stress austenite becomes unstable and begins to form stress-induced martensite.

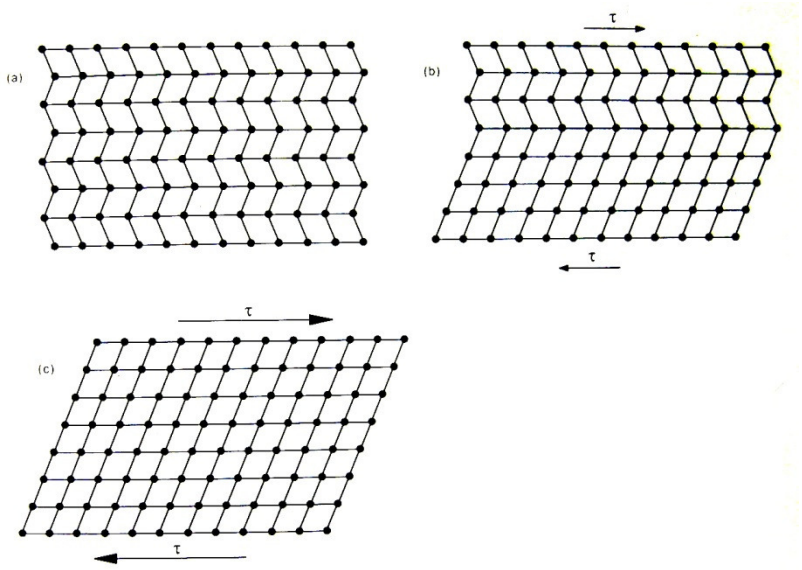

Figure 5: Two-dimensional representation of martensitic NiTi. a) fully tiwnned b) partially [6]

Twinning allows for the formation of energy equivalent configurations called variants that exist in lattices with a low degree of symmetry, such as monoclinic [11]. The variants are arranged

randomly in martensite produced by cooling from austenite, whereas in stress-induced martensite a single preferential variant occurs according to the direction of the applied stress [11]. Application of stress to the twinned structure results in the movement of twin boundaries, or detwinning. As no permanent deformation occurs at sub-critical stresses (~450 Mpa for Memry Corporation's SE-BA [12]), deformation resulting from detwinning is entirely recoverable.

It should also be noted that martensite inherits the composition and atomic order of its austenite parent phase, thus martensitic NiTi has an ordered atomic structure as described previously for austenite.

2.3.3 R-Phase

The third phase that can exist in NiTi SMA alloys is the R-phase. The R-phase appears upon cooling, prior to the martensitic transformation as a rhombohedral lattice structure [6]. Unlike the austenite-martensite phase transformation that has a temperature hysteresis in excess of 10^{o}C, the austenite-R-phase transformation is associated with a temperature hysteresis as small as 1.5^{o}C [6]. The R-phase is a martensitic-like phase and exhibits both the shape memory and superelastic effect, this makes it suitable for actuation devices that demand a small thermal hysteresis [6]. However, the maximum recoverable strain is much lower than a typical martensitic transformation, with strains reaching only 1% [6]. A differential scanning calorimetry thermogram for NiTi showing the various phases upon heating and cooling, including the R-phase, is presented in Figure 6. Differential scanning calorimetry is a thermoanalytical technique in which the difference in the amount of heat required to increase the temperature of a sample and reference is measured as a function of temperature. When a sample undergoes a physical transformation such as a phase transition, more (or less) heat will need

to flow to it than the reference to maintain both at the same temperature. Whether more or less heat must flow to the sample depends on whether the process is exothermic or endothermic.

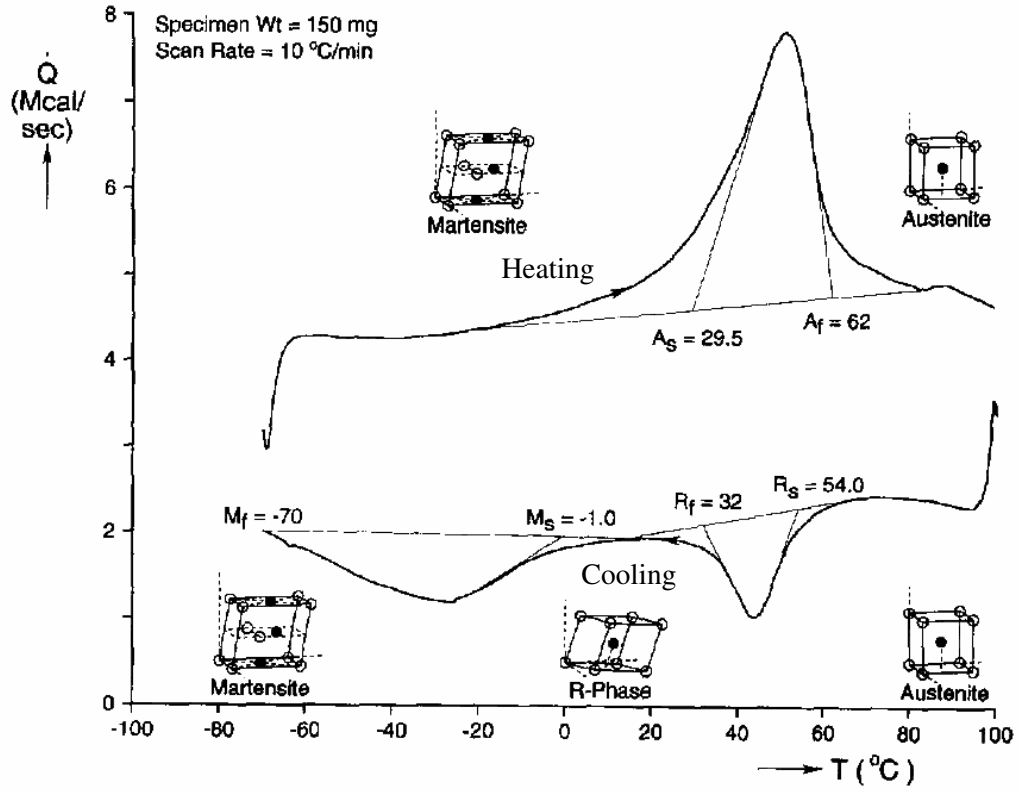

Figure 6: Differential scanning calorimetry thermogram of NiTi [11]

2.3.4 Temperature-Phase Relationship

As mentioned previously the phase that exists at any given time is dictated by the stress, temperature, and stress-temperature history. Temperature plays the key role, and for any given SMA there are four transformation temperatures (not including the R-phase) that define the phases of the material. These transformation temperatures are the martensite finish temperature (M_f), martensite start temperature (M_s), austenite start temperature (A_s), and austenite finish temperature (A_f). Figure 7 demonstrates

the relationship between temperature and phase in the absence of an applied stress. As can been seen in Figure 7, the temperature phase relationship exhibits a hysteretic behaviour.

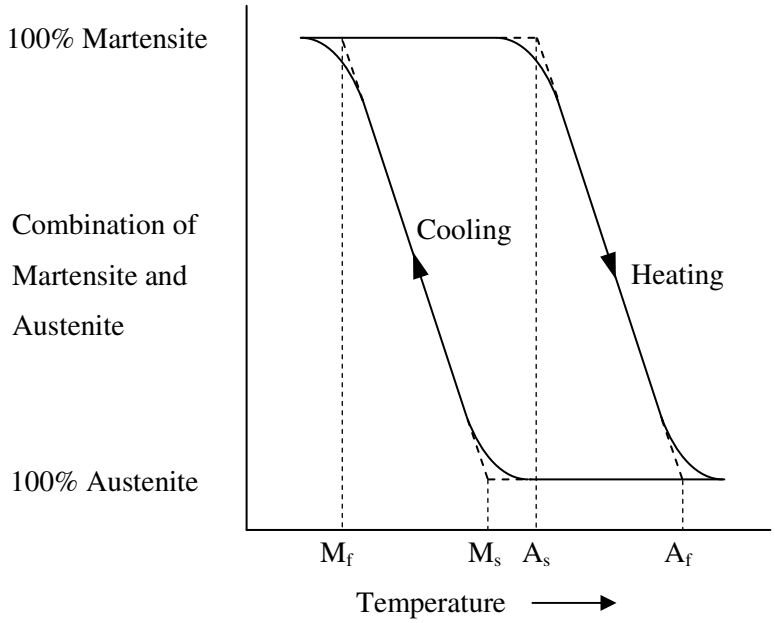

Figure 7: Temperature-Phase Relationship

The no-load transformation temperatures for a particular alloy vary over a range of temperatures depending upon the material constituents and processing history [6]. For Ni-Ti based SMAs the temperature range for the martensite start temperature is from approximately -150°C to 150°C and is strongly dependent upon the composition, particularly in Ni-rich alloys [6]. The relationship between composition and transformation temperature is provided in Figure 8. The transformation temperatures are also dependent on applied stress, and this is discussed in Section 2.3.6.

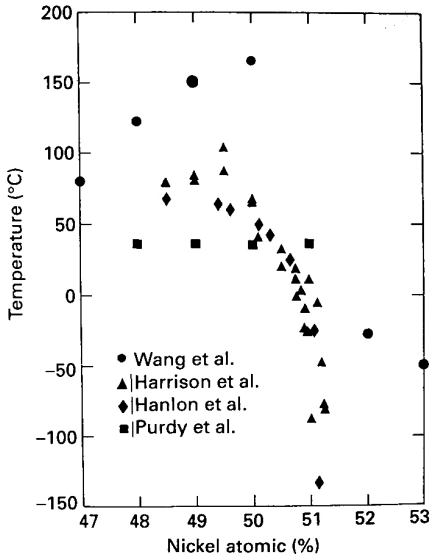

Figure 8: Dependence of transformation temperature on composition [6]

2.3.5 The Origin of Shape Memory

As previously stated, the SME is made possible by a SMA's ability to exist in three distinct crystallographic structures: martensite, austenite, and R-phase. Particularly, it is the transition from the less-symmetric martensite to the more-symmetric austenite that allows the material to return to its original shape [6]. The less-symmetric twinned microstructure of the martensite phase allows the SMA to form with several rhombus variants, thus accommodating various macroscopic geometries generated by applied stresses. However, there are no variants in the austenite phase and, therefore, when returned to austenite the material must return to its original microstructure, eliminating the geometry accommodated by the rhombus variants of the martensite [6]. Figure 9 provides a two-dimensional representation of the above described process in which only two martensite rhombus variants exist.

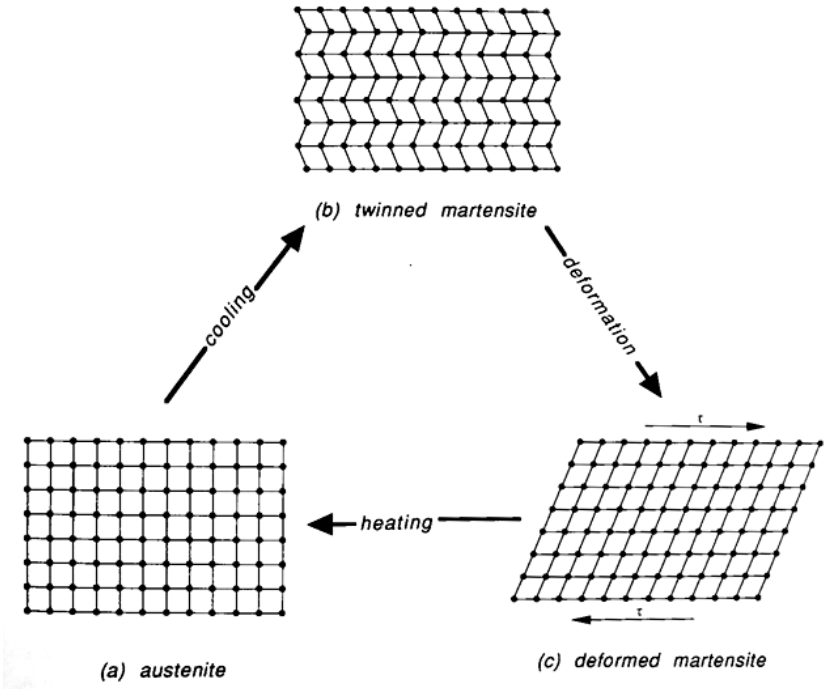

Figure 9: Microscopic origin of the shape memory alloy [6]

2.3.6 Stress-Phase Relationship

In order to accurately model the SMA behaviour it is necessary to account for the effect of applied stress on the transformation temperatures. An increase in applied stress shifts the transformation temperatures higher, thus shifting the entire hysteresis curves as shown in Figure 10 [6]. Experimental data for a Cu-Zn-Al-Mn SMA thermally cycled at different stress levels is provided in Figure 11. As expected, the transformation temperatures increase with increasing applied stress.

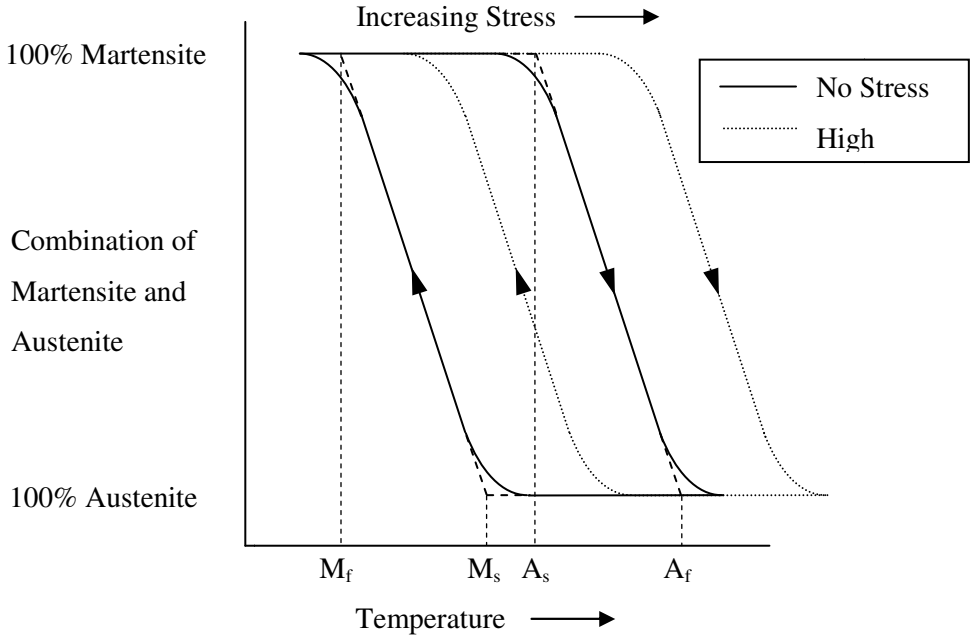

Figure 10: Stress effect on transformation temperatures

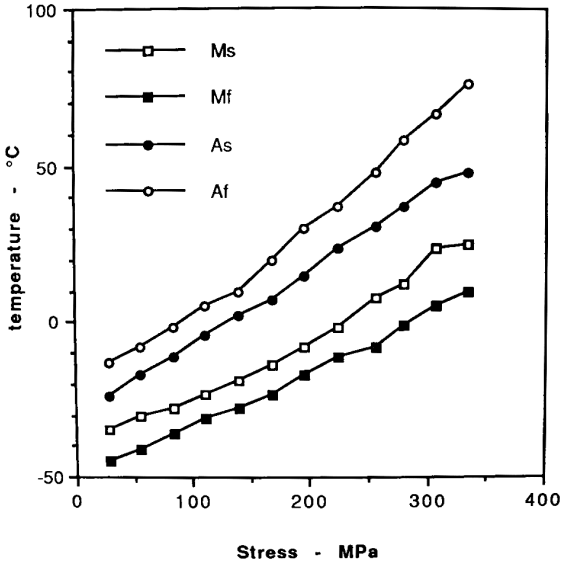

Figure 11: Stress versus transformation temperatures in a Cu-Zn-Al-Mn SMA [6]

2.3.7 Hysteresis Curves

In addition to temperature and stress, the temperature-stress history is also necessary to determine what phases are present at any given time. The solid line in Figure 12 represents the major hysteresis loop which occurs when the material is cycled between the extreme transformation temperatures M_f and A_f. However, if the material is switched from heating to cooling (or vice versa) within these extreme transformation temperatures, a minor hysteresis loop is developed. The dashed lines in Figure 12 show two possible minor hysteresis loops that could result from partial temperature cycling.

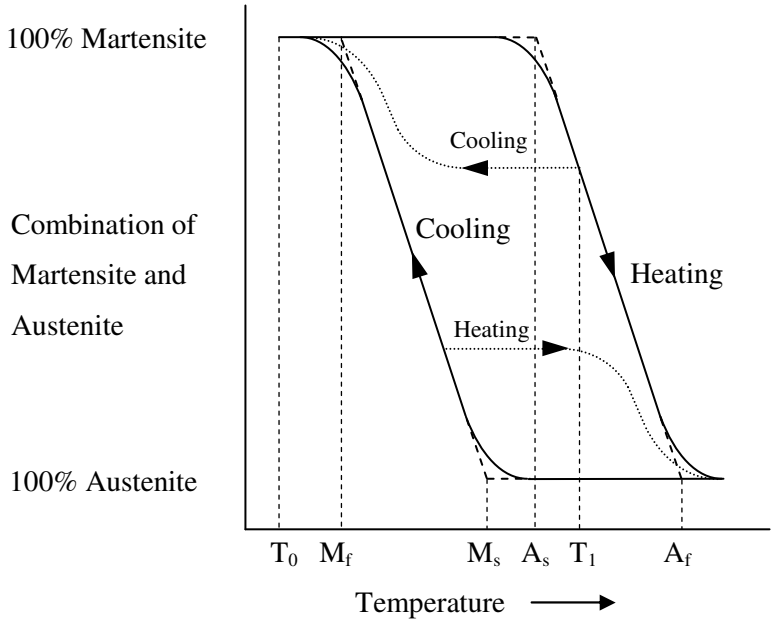

Figure 12: Minor loop behaviour

The effect of temperature history and partial cycling becomes evident when one considers an alloy heated from $T_0 < M_f$ to $A_s < T_1 < A_f$, then cooled to $T = M_s$. The resulting phase composition will differ from that of the same alloy heated from $T_0 < M_f$ to $T = M_s$.

2.4 Shape Memory Alloy Macroscopic Behaviour

We have explained that the SME is caused by the temperature-stress-phase relationship at the microscopic scale, however for the purposes of design we are more interested in the macroscopic behaviour of the material. Therefore it is necessary to characterize the performance of SMAs by analyzing their stress-strain-temperature relationship.

The stress, strain, and temperature of SMAs have a complex interdependent relationship. This differs from most metallic materials for which it is assumed that stress and strain are independent of temperature, and that stress and strain are linearly related by the following equation:

$$\boldsymbol{E = \frac{\sigma}{\epsilon}} \qquad \textbf{Equation 1}$$

In the equation above σ represents stress, ϵ represents strain, and E represents the elastic, or Young's modulus. The elastic modulus is a measure of the stiffness of a material, with stiffer materials having a higher modulus. However, this relationship is insufficient to describe the macroscopic behaviour of SMAs. Instead, more advanced models have been developed to describe the complex non-linear behaviour of SMAs, and will be discussed in Section 2.6 of this thesis.

The complexity in modeling SMAs stems from the dependence of the elastic modulus on both temperature and stress, and the inherent nonlinearity due to differences in the physical properties of austenite and martensite. As mentioned previously, the phase fraction is dependent on phase fraction (and hence on temperature and stress). The modulus is dependent on the relative phase fraction of martensite and austenite present in the material. Therefore, the modulus is dependent on temperature and stress and the above equation is no longer valid. The stress-strain-temperature relationship can best be described by Figure 13.

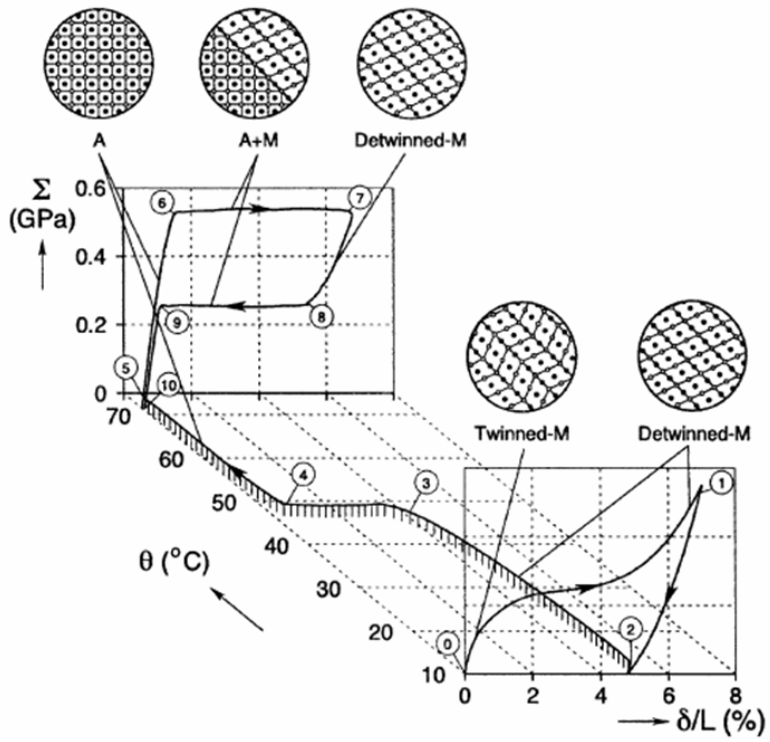

Figure 13: Three-dimensional SMA characteristic curve [13]

2.4.1 Martensite

For a material in the martensite phase ($T < M_f$), the stress-strain behaviour can be seen on the $\theta = 10^oC$ plane of Figure 13. This martensite stress-strain relationship can be approximated by several piece-wise continuous segments, illustrated in Figure 14. Within the first continuous segment the material undergoes linear elastic deformation with a constant elastic modulus, as in Figure 14 (segment 1). The stress eventually reaches a level capable of detwinning the martensite's twinned microstructure into a variant that better accommodates the applied stress, resulting in the second continuous segment. This segment has a much lower elastic modulus due to the relative ease with which twin boundaries move, and appears as a plateau in Figure 14 (segment 2). Finally, once the

material is fully detwinned we enter the last continuous segment in Figure 14 (segment 3), where we have elastic deformation of the detwinned rhombic crystalline structure.

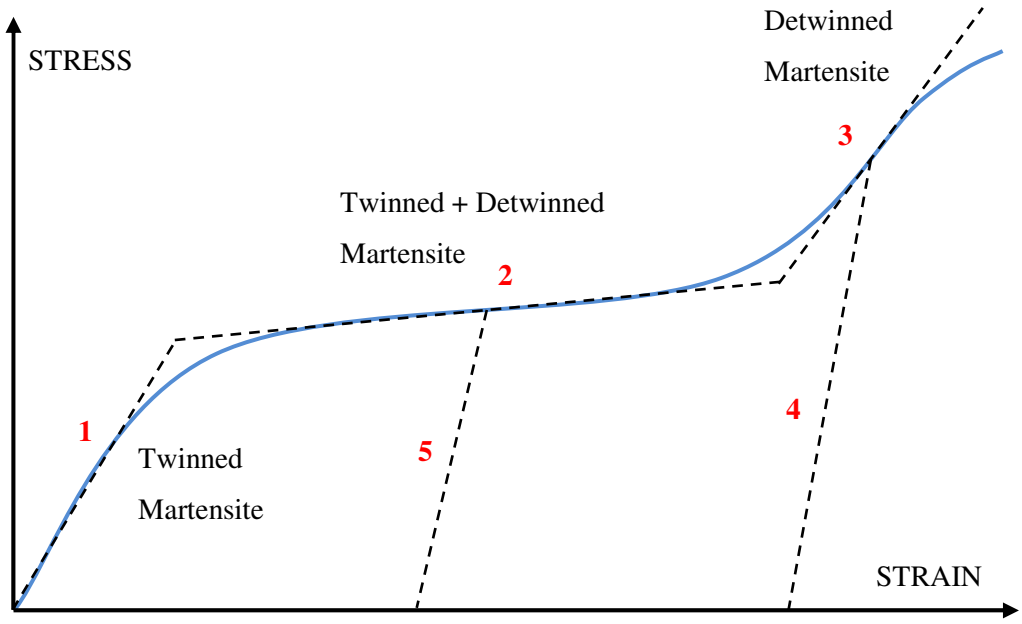

Figure 14: Loading, unloading, and reloading behaviour of martensite

The unloading behaviour of martensite is dependent upon which piece-wise continuous segment the material is in when unloading occurs. When the material is fully twinned (Figure 14 - segment 1), the unloading is elastic and follows the loading curve. When the material is fully detwinned (Figure 14 – segment 3), the unloading follows segment 4 in Figure 14. This curve may have an elastic modulus that differs from that of detwinned elastic loading (Figure 14 – segment 3). Finally, if the material is a combination of twinned and detwinned martensite (Figure 14 – segment 2), unloading follows a curve with a modulus proportional to the fraction of twinned and detwinned martensite at the point of unloading (Figure 14 – segment 5). As seen in Figure 14, unloading from segments 2 and 3 results in a residual strain or deformation in the material. However, this residual

strain can be removed by raising the material temperature above that of the austenite finish temperature (A_f). This is shown in the $\theta - \delta/L$ plane of Figure 13, where strain is recovered as temperature rises above ~50°C.

Finally, we must account for loading that occurs after unloading has been initiated. This type of loading will be referred to as reloading. When reloading occurs in the martensite phase, the material follows its respective unloading curves until it joins the original loading curve. At this point the reloading follows the loading curves as described previously.

2.4.2 Austenite

Consider now a SMA that is above T_{Af} and therefore fully austenite, with a response as shown in the plane of $\theta = 70^oC$ in Figure 13. Again the stress-strain behaviour can be approximated as piece-wise continuous, starting with a linear elastic region as shown in Figure 15 (segment 1). In this case, the stress eventually reaches a level at which stress induced martensite (SIM) is formed. Increasing stress effectively increases the transformation temperatures (Figure 10) high enough that the martensite start temperature (M_s) is greater than the operating temperature, thus initiating the formation of martensite. This can also be thought of as increasing the temperature required to stabilize austenite over martensite. As the austenite is converted into SIM there is a reduction in the elastic modulus and a plateau develops (Figure 15 - segment 2). Once the SMA is completely converted into stress induced martensite, there is an increase in the elastic modulus as elastic deformation of the detwinned rhombic crystalline structure occurs (Figure 15 - segment 3).

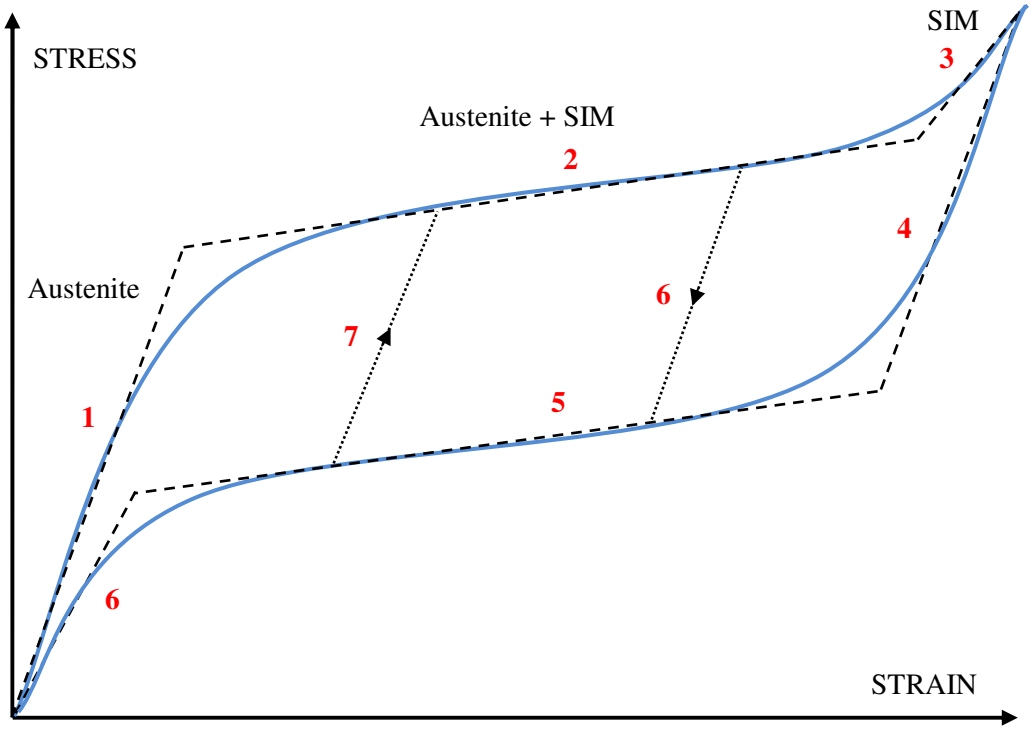

Figure 15: Loading, unloading, and reloading behaviour of austenite

As with martensite, the unloading behaviour of austenite is dependent upon which piece-wise continuous segment the material is in when unloading occurs. When the material is within the first linear elastic region (Figure 15 – segment 1), unloading is elastic and follows the same curve as loading. When the material is unloaded after being loaded beyond the first critical stress (Figure 15 – segments 2 and 3), the material exhibits what is known as the superelastic (or pseudoelastic) effect. If the material is unloaded from fully stress-induced martensite (SIM) (within segment 3 of Figure 15), it follows segments 4, 5, and 6 in Figure 15. This pathway exhibits three distinct piece-wise continuous segments similar to that observed in loading. If unloading occurs when the material is partially SIM (Figure 15 – segment 2), unloading follows segment 6 in Figure 15 until it intersects with the unloading plateau of segment 5 in Figure 15. At this point unloading follows the path as

described for unloading of fully SIM. The modulus of this unloading line (Figure 15 – segment 6) is proportional to the fraction of SIM present at the time of unloading.

The reloading behaviour of austenite shares some similarities with that of martensite. If the material were reloaded within the initial linear elastic region (Figure 15 – segment 1), it acts as a linear elastic material and follows the same path as loading and unloading. If the material is reloaded when it is on some portion of the superelastic unloading loop (Figure 15 – segments 4, 5, and 6), including both unloading from fully SIM and partially SIM (Figure 15 – segments 2 and 3), then the reloading follows a new path, segment 7 in Figure 15, until it intersects with the loading curve (Figure 15 – segment 2 or 3) where it then continues along the loading curve. This reloading path (Figure 15 – segment 7) has a modulus that is proportional to the fraction of SIM present in the material at the point of reloading.

2.5 Fabrication Methods

2.5.1 Current Techniques of NiTi Fabrication

As more NiTi products are developed and produced at larger scales, it becomes increasingly important for manufacturers to deliver materials with consistent performance. However, SMA properties are extremely sensitive to initial composition as well as the subsequent processing. NiTi's resistance to deformation, significant work-hardening rate, and high titanium content also contribute to the difficulty of fabrication. In particular, the high concentration of titanium present in the alloy makes molten NiTi highly reactive, therefore it must be processed in a vacuum.

Typically, commercially available bulk NiTi is formed by both vacuum induction melting (VIM) and vacuum consumable arc re-melting (VAR). As the names suggest, both methods involve the melting of a metal under vacuum conditions. With VIM an electromagnetic induction coil

induces electrical eddy currents in the metal which heat and eventually melt the charge. VAR works by creating an arc of direct current between an electrode and the alloy to be re-melted, again heating and eventually melting the charge. These processes are both time consuming and expensive. Other methods have been used at smaller scales including non-consumable arc melting, electron beam melting, and plasma melting. Once the ingot has been formed it is rolled at an elevated temperature into a bar or slab. Following hot working, the NiTi alloys undergo a series of cold working steps to arrive at the desired final dimensions. Cold working of NiTi is difficult due to its high rate of work-hardening. Finally, heat treatments are performed to obtain the desired mechanical and shape memory properties. Wire, rod, sheet, and tubing are routinely manufactured using the above processes [8].

Thin film fabrication techniques have also been used for the manufacture of micro electromechanical systems (MEMS). NiTi is deposited on a silicon or glass substrate by sputter deposition and then fabricated into commercial components by photolithographic techniques [14].

In recent years porous NiTi has received attention for its potential as a biomedical implant material due to its high biocompatibility [15] and unique mechanical properties similar to longbones [16]. Matching the physical properties of load bearing implants with that of the remaining bone prevents what is known as stress shielding, which causes re-absorption of the bone necessary for anchorage and eventual failure of the implant [16]. In addition, porous NiTi encourages high levels of bone in-growth, again resulting in improved fixation [16]. Therefore, techniques for the fabrication of porous NiTi have also been developed. The most common method of manufacturing porous NiTi is powder metallurgy (PM), and the activation of combustion synthesis.

2.5.2 Powder Metallurgy

Various powder metallurgy processes have been developed with the goal of producing near net shape components and more accurate control of transformation temperatures. Both pre-alloyed and elemental powders have been used. PM's ability to produce near net shape components and accurate control of transformation temperatures make PM an attractive approach for fabricating planar NiTi actuators at the meso-scale where machining can be difficult and composition important in developing the desired motion within its operating temperature. In addition, PM in the form of tape casting can potentially create components with non-uniform compositions and is elaborated upon in Section 2.5.3. However, it has proven difficult to obtain a dense, homogenous, oxygen free component using PM techniques. These factors degrade the mechanical properties of NiTi and its SME, thus degrading the performance of actuators fabricated using these techniques.

In order to produce a component using PM, the powders are blended, compacted, and sintered. Compaction has been done using isostatic pressing [17], uniaxial die compression [18], direct powder rolling [19], metal injection moulding (MIM), and consolidation by atmospheric pressure [20].

As mentioned previously, the powders used in the production of NiTi can either be pre-alloyed or elemental. Mixing pre-alloyed powders with different transformation temperatures in the appropriate ratio can produce SMAs with predictable intermediate transformation temperatures with good precision [17]. Substantial work has also been performed on PM processing of elemental nickel and titanium powders. Using elemental powders avoids the additional and costly processing associated with the fabrication of pre-alloyed powders.

Once compacted, a sintering process is necessary to fuse the powders into the final component. The fusion of Ni and Ti is highly exothermic and this heat of fusion can be used to fabricate NiTi. Self propagating high-temperature sintering (SHS) is described for elemental powders

by Itin [21]. The elemental powders are either ignited by a localized high temperature source and the reaction is allowed to propagate through the sample, or by heating the entire sample until ignition is reached. SHS results in highly porous NiTi, suitable for medical implants and shock energy absorption. However, porosity is undesirable from the perspective of actuator design. In order to obtain dense components the ignition temperature of SHS must be avoided, and the sintering process must rely solely on solid state diffusion.

Hot isostatic pressing (HIP) has proven to be the most effective at obtaining a dense component with densities of up to 95 percent reported [18]. HIP subjects the component to both elevated temperature and isostatic gas pressure in a high pressure containment vessel. Samples produced by HIP with both elemental and pre-alloyed powders reveal dense components with high reproducibility of transformation behaviour, but the fracture strain of the samples was found to be low. Fractures strains were found to have a maximum of 2.2 percent for pre-alloyed powders and 1.0 percent for elemental powders [22]. Oxide phases are believed to be responsible for the decrease in mechanical properties by embrittlement of the matrix [22]. Despite sintering in an oxygen free atmosphere, oxygen contamination can still result from contamination of the original powder(s). Examination of the fracture surface by Kato [23] and Schüler [22] have found mixed brittle and ductile fracture modes, where brittle fracture is described as a result of oxides on the particle surface. The presence of Ni_3Ti phase may also weaken the specimen microstructure by lowering the strength, thus contributing to the poor mechanical properties [22].

Vacuum sintering at atmospheric pressure has also been used to produce homogenous NiTi with densities of up to 96 percent of theoretical density [24]. However, this process experiences the same problems with oxygen contamination as the HIP process mentioned above with lower densities. The decrease in mechanical properties associated with PM fabrication still remains a barrier to producing components suitable for actuator applications.

2.5.3 Tape Casting

Tape casting, also known as doctor blading or knife coating, is a manufacturing technology used to create thin films of material on a substrate. The technique has long been used in the paint industry, and has been more recently adapted for the creation of thin sheets of ceramics and metallics in the semiconductor industry [25]. The process allows for the creation of large, thin, flat parts that would otherwise be virtually impossible to press or extrude [25].

For metallic materials, the typical tape casting process involves the mixing of a metal powder with a polymer solution to create a slurry, or slip. Details on slurry recipes for Ni and Ti powders are provided in Section 3.1.2 of this document. The slurry is then poured into a reservoir and cast onto a moving substrate as shown in Figure 16. The slurry is pulled under the gap between the doctor blade and substrate as the substrate moves at a uniform rate in the direction indicated in Figure 16. The wet film is allowed to dry, the solvents evaporate, and the polymer-suspended metallic matrix is left behind.

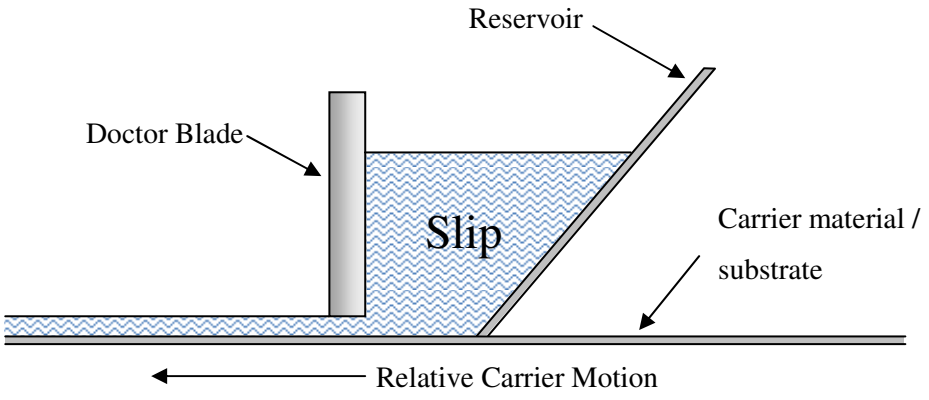

Figure 16: Principle of the tape casting process

This polymer sheet with embedded metallic powder can be cut, stacked, and pressed into various geometries. These dry tapes, or green compacts, then undergo sintering techniques similar to those described previously with the addition of a burnout stage. The burnout involves heating the green compact in atmosphere to burn away the polymer, leaving behind the metallic matrix to be sintered into the final component.

The advantages of tape casting are the ability to create more complex geometries as compared to dry powder pressing and the ability to produce components with regions of varying compositions by mixing or stacking several tapes into a single component.

2.6 Modeling Techniques

2.6.1 Lumped-Element Modeling of Shape Memory Alloys

Several different strategies for modeling SMAs have been developed over the past 15 years including thermodynamics, micromechanics, thermomechanical, and phenomenological. The majority of these models are limited to simple geometries, however, the implementation of these models within the finite element method (FEM) allows for their extension into complex two and three dimensional geometries. Therefore, the FEM is the choice design tool in this research for developing relatively complex two and three dimensional SMA actuators.

Thermodynamic SMA models have been developed by Achenbach [26], and later extended by Seelecke and Mueller [27]. Boyd and Lagoudas [28], and Ivshin and Pence [29] also developed models based on thermodynamic principles. A micromechanics-based Helmholtz free energy was obtained by Goo and Lexcellent [30] and used within an irreversible thermodynamics framework to develop a kinetic relationship, and martensitic nucleation and variant reorientation criterion.

Phenomenological models have also been developed to describe the complex behaviour exhibited by SMAs. The advantages of phenomenological models stem from the fact that they directly describe the observed behaviour of the material being modeled. Thus they are generally simpler, making them computationally faster. This property makes phenomenological models ideal for controls applications and computationally intensive modeling such as FEM.

Preisach [31] developed a phenomenological model that describes hysteretic behaviour as a summation of weighted hysteresis relays. While this model is commonly used, its disadvantage lies in the requirement of identifying a large number of variables. Phenomenological models used to describe SMAs were also developed by Tanaka et al. [32], and Liang and Rogers [33]. This work was later extended by Brinson [34], with the separation of temperature- and stress-induced martensite, and the addition of twinned and detwinned martensite. Similar work to Tanaka was also developed by Ikuta et al. [35], and later extended by Madill and Wang [36], and finally Pai and Gorbet [37]. The Madill model added minor loop behaviour to the Ikuta model, however, it still lacked the ability to model variable stress. This functionality was eventually developed by Pai [38] in conjunction with a mechanical model that describes the complete loading, unloading, and reloading behaviour of SMAs.

2.6.2 Finite Element Modeling of Shape Memory Alloys

The lumped-element modeling techniques described in the previous section are incapable of simulating the behaviour of NiTi components with complex geometries. As devices containing SMA elements become more elaborate, tools that can incorporate SMA materials with other mechanical units will become increasingly necessary. The implementation of these constitutive equations into a finite element procedure offers a solution to these limitations. Early work by Brinson and Lammering

[39] implemented the constitutive relations developed by Brinson [34], based on previous work by Liang and Rogers [33], and Tanaka et al. [32] into a FEM. The constitutive model used in this work was developed on a thermomechanical basis. The Brinson and Lammering FEM implementation accurately described the SMA behaviour, but was limited to one dimensional analysis. Similar FEM implementations have been developed by Boubaker et al. [40], and Trochu and Qian [41].

More recently Peultier et al. [42], and Wang and Yue [43] have developed three-dimensional micromechanical FEMs based on the Gibbs free energy expression. Their work includes implementation into commercially available finite element software (ABAQUS) and validation with experimental data. Such models offer a powerful tool towards the development of complex SMA actuators and components. However, due to software availability and familiarity, and concurrent work on a Matlab implementation of a lumped-element SMA model [38], an alternative FE implementation was developed.

2.7 Shape Memory Alloy Actuator Design

As illustrated previously in Figure 13, the stress-strain relationship of martensite and austenite differ, enabling the design of shape memory alloys (SMAs) exhibiting the shape memory effect (SME). The austenite phase is stiffer than that of martensite, therefore under a constant load a specimen that is fully austenite will have a smaller strain than one that is fully martensite. Consider the constant load actuator design provided in Figure 17 which utilizes an SMA spring vertically suspending a constant mass under the force of gravity.

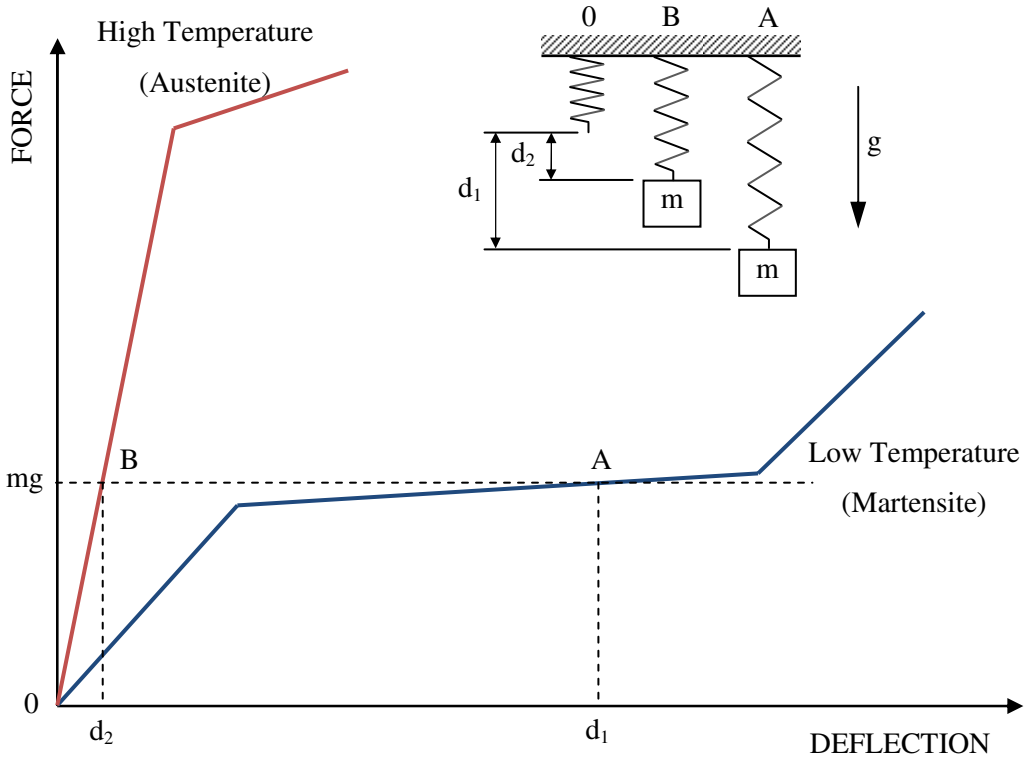

Figure 17: SMA spring under constant load. Adapted from [6].

At low temperatures the spring in Figure 17 is fully martensite and the spring deflects a distance of d_1 corresponding to its respective force-displacement curve due to the force of gravity acting on the attached mass, m (point A in Figure 17). As the temperature is increased above the austenite finish temperature (A_f) and the spring is transformed into austenite the deflection of the spring decreases to d_2, again corresponding to its respective force-displacement curve due to the force of gravity acting on the attached mass, m (point B in Figure 17). Therefore, as the spring is transformed from martensite to austenite work in the amount of $mg(d_1-d_2)$ is performed as the mass, m, is moved over a distance of d_1-d_2 against gravity. When the spring is allowed to cool below the martensite finish temperature (M_f) the spring transforms back into martensite and gravity acting on the mass resets the actuator.

An alternative, and often more practical SMA actuator design, utilizes a conventional spring rather than gravity acting on a mass to provide the bias force necessary to reset the actuator in its low temperature martensite state. Figure 18 illustrates the operating principle of the spring-biased SMA actuator. A compression spring is shown, although designs incorporating tension springs are common as well. When the SMA spring is in its low temperature martensite state the force generated by the conventional spring acts against the SMA resulting in an equilibrium displacement, d_1. As the temperature of the SMA spring is increased and is transformed into austenite it exerts a greater force against the conventional compression spring resulting in a new equilibrium displacement, d_2. Again, work is performed as the SMA spring acts against the conventional spring, simultaneously storing potential energy that will be utilized to restore the actuator when returned to its low temperature martensite state. The overall displacement generated by this actuator is denoted by Δx in Figure 18.

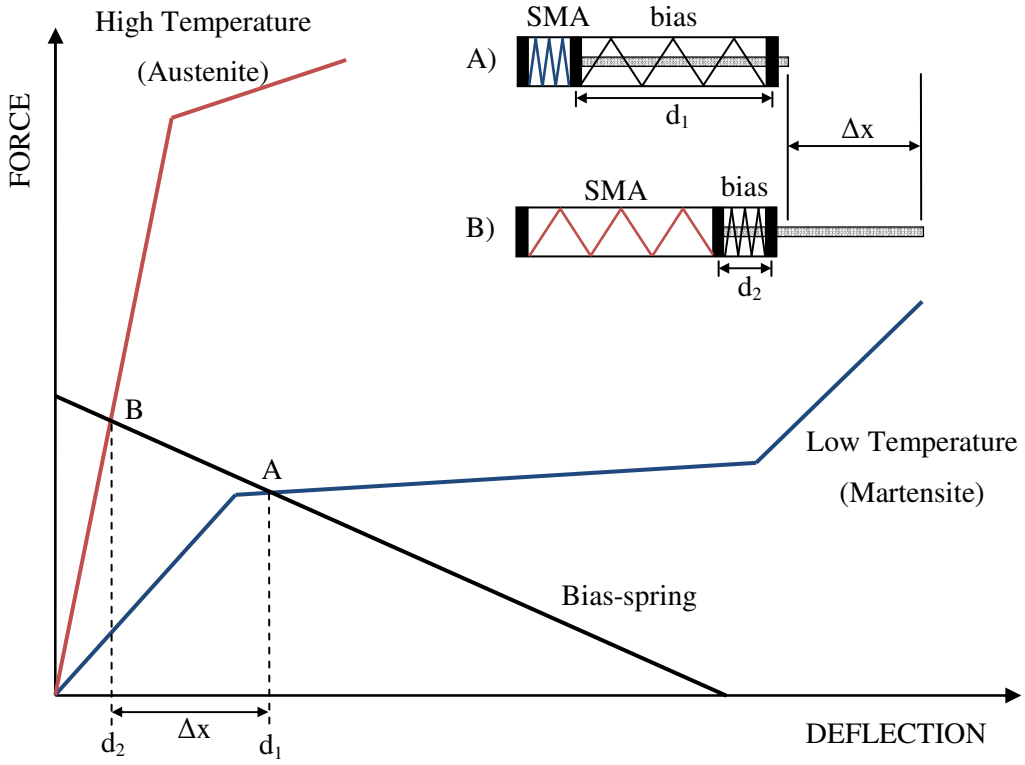

Figure 18: Spring-biased SMA actuator. Adapted from [6].

Finally, in many instances it is desirable that some of the work generated by the actuator be used to perform some external function. The spring-biased actuator in Figure 18 is not loaded, and therefore does not utilize any of its work to perform an external function. Figure 19, however, illustrates a spring-biased actuator that acts against a force, F, when actuated. The amount of displacement decreases since the new high-temperature equilibrium point occurs where the sum of the bias spring and the external load equal the force generated by the SMA spring. Hence, ΔF is the net force which the spring-biased SMA actuator can exert on a load mg with a displacement of Δx.

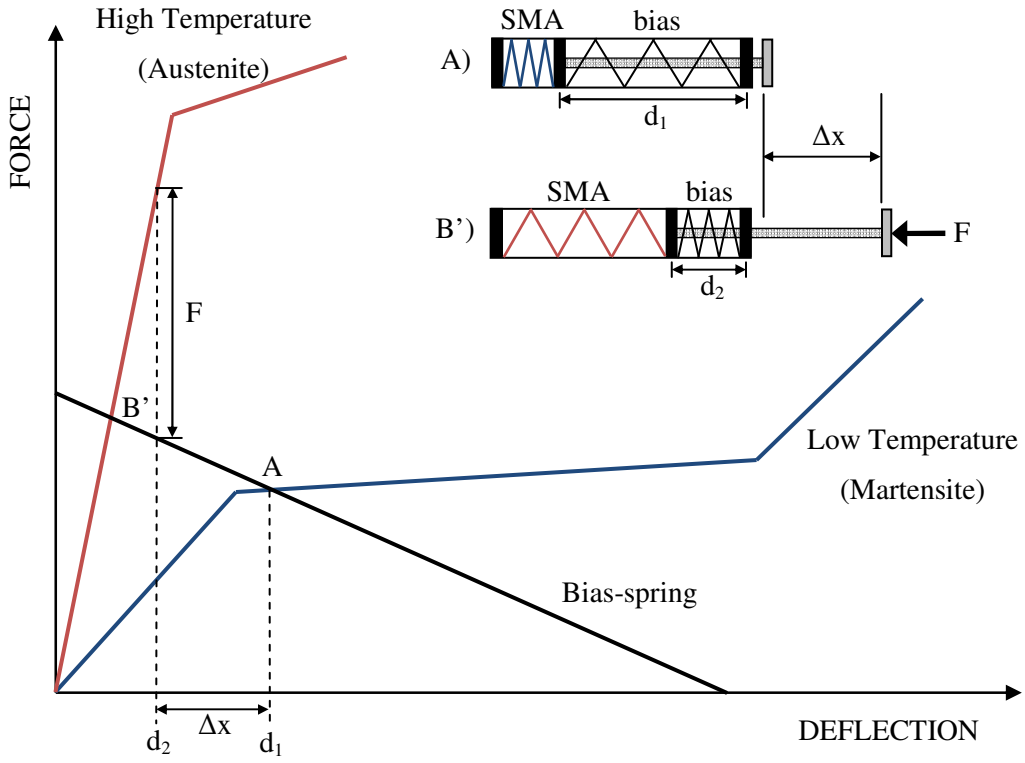

Figure 19: Spring-biased SMA actuator with external load. Adapted from [6].

2.7.1 Monolithic Shape Memory Alloy Actuator

As demonstrated in the previous section, SMA actuators require a bias force to reset their shape in order to achieve cyclic motion. Two methods were illustrated including a hanging mass and spring force as a means of storing energy generated during the high temperature austenite state to be used later to reset the actuator when returned to its low temperature martensite state. Both reset mechanisms require physical attachment of some device to the SMA material in order to achieve the desired bias force. This assembly step becomes increasingly difficult as devices are miniaturized, thus making conventional reset mechanisms difficult or impossible to implement. One solution to

this problem is the development of monolithic actuators, which are single-piece mechanical devices capable of generating motion.

With SMA materials this can be accomplished by a process of selective annealing. SMA material after processing does not exhibit the SME prior to an annealing procedure. Therefore, selectively annealing regions of a piece of SMA material results in those regions exhibiting the SME, while the remaining non-annealed regions demonstrate elastic behaviour. These non-annealed elastic regions act as the bias force reset mechanisms providing cyclic actuator operation from a single, monolithic, piece of material. Several methods have already been developed to locally anneal the SMA material including direct Joule heating, laser heating, and local contact heating [3] [4]. The ability to localize the annealing is critical, since the non-annealed portions of the material are required to act as a restoring bias force and must not demonstrate the SME. Several examples of monolithic SMA actuators are shown below; because of the typical geometries, the starting material is usually as-received NiTi ribbon.

Direct Joule heating was applied by Bellouard et al. [3] to a one-axis translation stage as seen in Figure 20. The structure was first laser cut from a ribbon of as-received non-annealed SMA to produce the desired geometry. An electrical current was then passed through the left set of springs as indicated in Figure 20, heating them to the annealing temperature, thus locally imparting the SME. During the annealing the right set of springs remained at room temperature, thus remaining in the non-annealed state. Once cooled the springs on both sides were pre-strained along the x-axis and fixed in place. Therefore, when the left set of springs are at high temperature the stage is pushed to the right, and when cooled the stage is returned to the left by the non-annealed set of springs on the right.

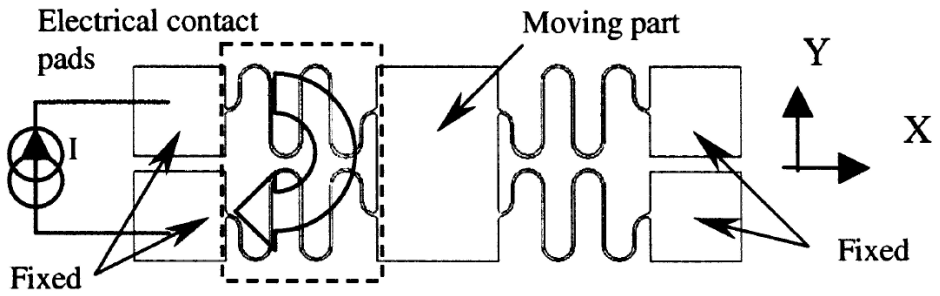

Figure 20: One-axis monolithic translation stage with four leaf springs. Dimensions: 6.5 x 20 mm^2. Spring thickness: 60 µm. Strip thickness: 150 µm [3].

In order for direct Joule heating to be an effective technique, the design of the actuator must be such that a suitable electrical path is created through the region that is to be locally annealed. This path must also be of consistent cross-sectional area as the thinnest section will anneal first due to its higher resistance [3].

Another method applied by Bellouard et al. [3] is laser heating. A laser beam is used to locally heat any region of an as-received non-annealed SMA ribbon to its annealing temperature. This method eliminates the necessity of incorporating an electrical path of consistent cross-sectional area into the design of the region to exhibit the SME. The gripper design in Figure 21 is first laser cut from a strip of as-received non-annealed SMA [3]. The laser is then used to heat the semi-circular hinge of the arm (Figure 21), which locally anneals the hinge and imparts the SME. At room temperature, the gripper arm is then deformed beyond its elastic limit in order to define the open position. Upon heating, the gripper closes due to the recovery force generated by the phase transformation in the annealed circular hinge.

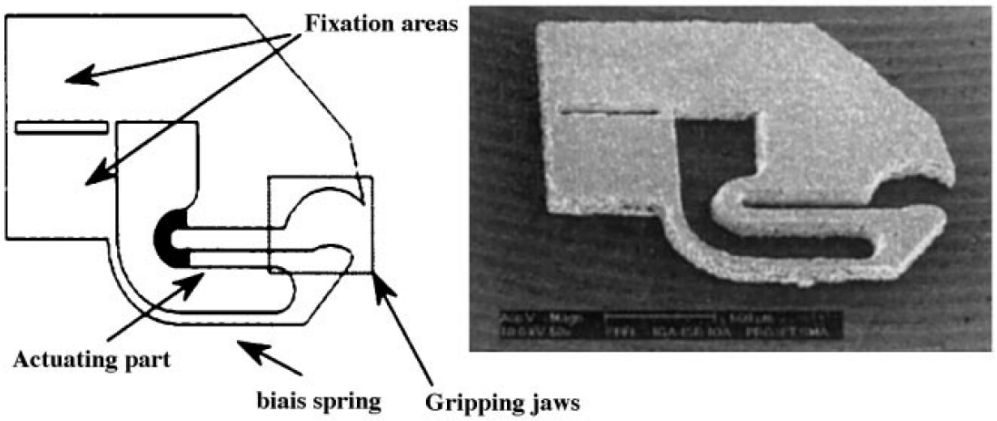

Figure 21: SMA gripper design and realization. The black area represents the locally-annealed area. Dimensions: 1.4 x 1.8 mm^2 [3].

A final method developed by Toews [4] was local heating of the region to be annealed by direct contact with a Joule heated Nichrome strip. The planar monolithic actuator design presented in Figure 22 is constrained in a curved position by an aluminum die with the centre region in contact with a Nichrome strip. As the Nichrome is heated the centre beam is annealed, while the side members remain below the annealing temperature.

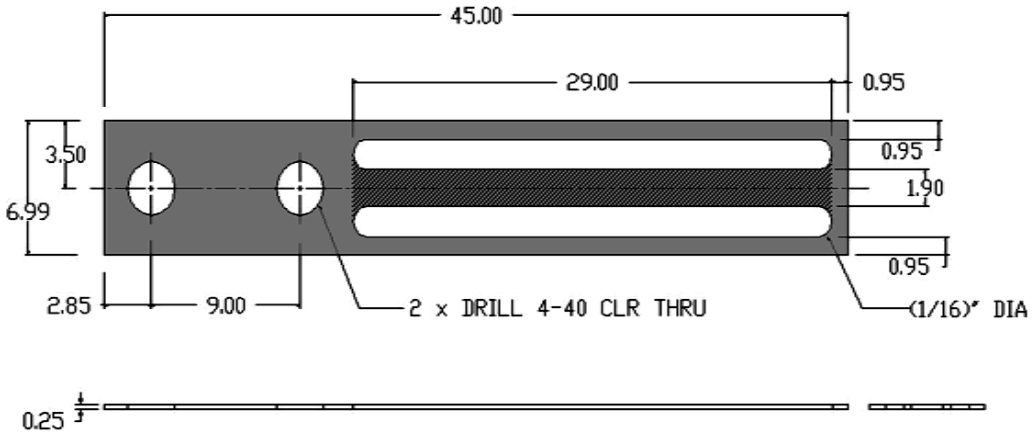

Figure 22: Planar monolithic actuator design [4]

The remaining non-annealed material acted as the bias mechanism, storing energy during out-of-plane deformation used to reset the actuator in its low temperature martensite state, thus providing cyclic actuator operation as illustrated in Figure 23. Position 'd' represents the non-annealed initial state, position 'a' represents the constrained SMA annealing state, and positions 'b' and 'c' represent the equilibrium austenite and martensite actuation states respectively. However, the range of motion of all designs was limited by the mechanical properties of the as-received, non-annealed material. In order to act as the reset bias mechanism, the non-annealed regions had to remain within their elastic limits. The typical range of recoverable strain in NiTi exhibiting the SME is 7% [6], whereas that of non-annealed NiTi is only 1% [44]. Additionally, local annealing becomes increasingly difficult as the overall size of the device is reduced.

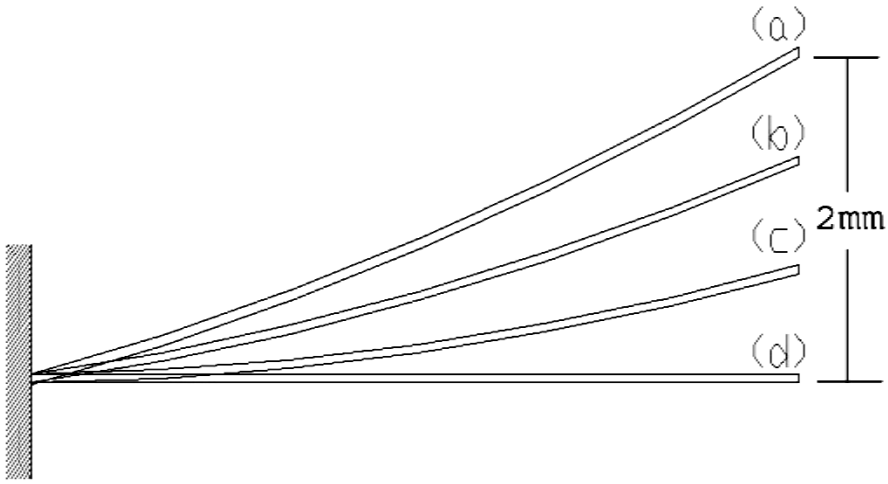

Figure 23: Conceptual actuator operation [4]

Chapter 3

Powder Metallurgy and Tape Cast Fabrication

Fabrication of NiTi by powder metallurgy tape casting techniques offers several advantages over conventional fabrication techniques. The process is less expensive than standard vacuum induction melting (VIM) and vacuum arc re-melting (VAR) technologies, allows for the direct fabrication of planar components with complex geometry, and allows for the creation of functionally graded components.

This section outlines the potential benefits of PM tape cast fabrication as it pertains to the development of planar hybrid monolithic SMA actuators, and presents some preliminary results from PM tape casting experiments. Problems with the current technique are discussed and direction for future development is provided.

PM tape cast components offer the capability of creating functionally graded, or hybrid components. Hybrid components are formed by casting two or more green tapes with different NiTi compositions, thus each having different transformation temperatures. These tapes are then cut, combined, and pressed to form a single green compact with regions of various NiTi compositions. These compacts are then sintered to form a single continuous (or monolithic) component with a functionally graded composition.

3.1 NiTi Tape Recipe

3.1.1 Powder Selection

The first step in the fabrication of a NiTi green tape is the selection of the powder or powders that will determine the final composition of the sintered component. Elemental powders were used so that the exact composition of the final NiTi alloy could be controlled. Additionally, the use of elemental powders is cheaper, as the costly manufacture of NiTi by VIM and VAR is not required. Powder sizes were selected based on previous and ongoing studies at the University of Waterloo investigating the NiTi sintering process [45]. A single titanium powder size was chosen and used to create two tapes with different nickel powder sizes in the appropriate weight ratio for the creation of NiTi. The powder sizes and compositions are provided in Table 2.

Table 2: Powder size and ratios

	Powder Type	Powder Size (μm)	Composition (wt.%)
Tape #1	Titanium	< 44 (-325 mesh)	45.4
	Inconel 123 (nickel)	3.5 – 4.5	54.6
Tape #2	Titanium	< 44 (-325 mesh)	45.4
	Inconel 110 (nickel)	1.0 – 2.0	54.6

3.1.2 Slip Recipe

Tape casting is a fluid forming process, and therefore requires that the powder behave as a fluid. In order to achieve this behaviour the powder is suspended in a liquid, commonly referred to as the "solvent". In addition to acting as a suspension for the powder, the solvent acts to homogenously distribute the other ingredients of the tape recipe. The majority of tape casting solutions are made

with non-aqueous solvents [25]. As mentioned previously, the solvent must be capable of dissolving the other ingredients of the tape formula; multiple solvents are often used to achieve this. For the NiTi tape used in this work, a mixture of both toluene and ethanol was used as the solvent. The full tape recipe is summarized in Table 3.

Table 3: NiTi tape ingredients

Ingredient	Weight (grams)
Blown Manhaden Fish Oil	0.375
Ethanol (~95%)	2.63
Toluene (~95%)	3.86
Polyvinyl Butyral (B79 Binder)	0.81
Butyl Benzyl Phthalate (S-160 Type I Plasticizer)	1.52
Nickel Powder	25.16
Titanium Powder	20.59

When individual powder particles are left in close proximity with each other they often tend to form loosely bound groups due to their inherent electrostatic forces or other interparticulate forces. These groups of powder particles are referred to as flocs. When the powders are suspended in a fluid, these flocs can form as the suspension attempts to lower its free energy by reducing the solid-liquid interface area. Flocs can be detrimental to the properties of the tape, and therefore an additional additive must be included in the recipe to break them up.

The main function of a deflocculant, or dispersant, is to surround the individual powder particles and keep them apart. In addition to preventing the formation of flocs and providing a more homogenous tape solution, deflocculants separate and hold the primary particles to allow uniform coating by the polymer binder agent. In this work, blown menhaden fish oil (MFO) was used as the

dispersant. MFO is one of the most commonly used dispersants in tape casting due to its large variety of fatty acid esters, allowing it work well with many powder mixtures. It acts as a steric hinderance deflocculant by coating each particle and thus preventing direct physical contact with another particle.

The final ingredient of the tape casting solution is the binder. The binder is typically added at a later stage in the mixing process so that the deflocculant first has a chance to coat the powder particles. The binder is responsible for holding the solution and powder matrix together for further processing. Essentially, the green tape can be thought of as a polymer matrix made up of the binder material that has been impregnated with the powder material. The binder used in this work was a combination of B79 binder agent (polyvinyl butyral) and S-160 Type I plasticizer (butyl benzyl phthalate). The role of the plasticizer is to make the binder material more flexible. This polymer solution provided sufficient strength and flexibility for the cutting, stacking, and pressing necessary for fabricating simple planar geometries.

3.2 Fabrication Procedure

3.2.1 Mechanical Mixing

The powders, solvent, and deflocculant were measured and placed in a cylindrical plastic container filled with ceramic milling balls. The mixture was then milled continuously for seven hours to ensure the deflocculant completely coated the individual powder particles. Once complete, the polymer material as indicated in Table 3 was added to the mixture and milled for an additional 18 hours. The same milling schedule was used for the creation of both tape mixtures to ensure consistency and to avoid the introduction of another variable. The milling apparatus is presented in Figure 24.

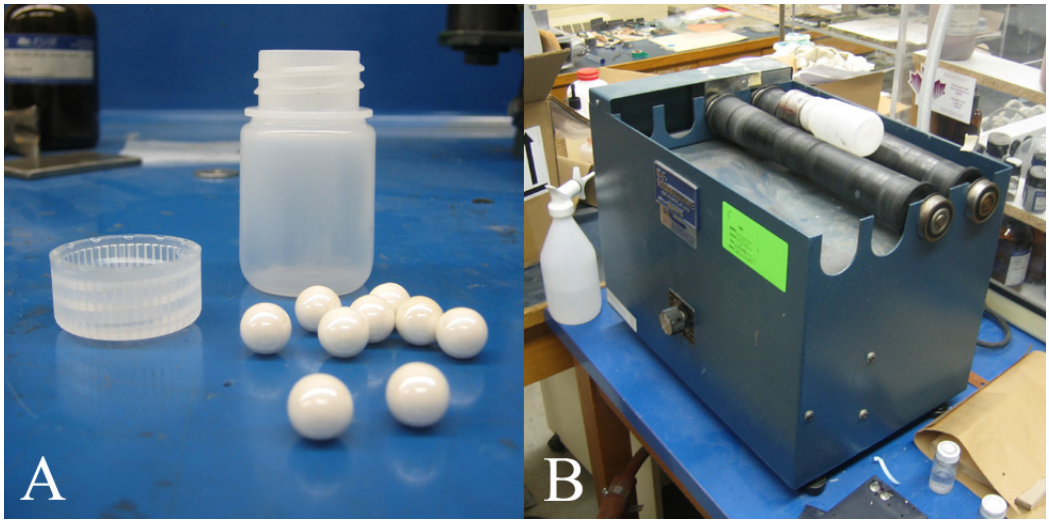

Figure 24: Mechanical milling apparatus. A - milling container and ceramic milling balls. B – mill.

3.2.2 Casting

Once milled, the tapes were cast using equipment purchased from Richard E. Mistler Incorporated, as shown in Figure 25. The tapes were cast onto a silicon coated mylar sheet moving at a continuous rate. The initial rate was set based on the viscosity of the slurry and later adjusted in order to achieve a tape thickness as consistent as possible. After the tapes were cast they were allowed to air dry over night to allow sufficient time for all the solvent to evaporate. The finished tapes were 110 mm wide, and approximately 280 mm long. An example cast is provided in Figure 26, and the casting apparatus is presented in Figure 25.

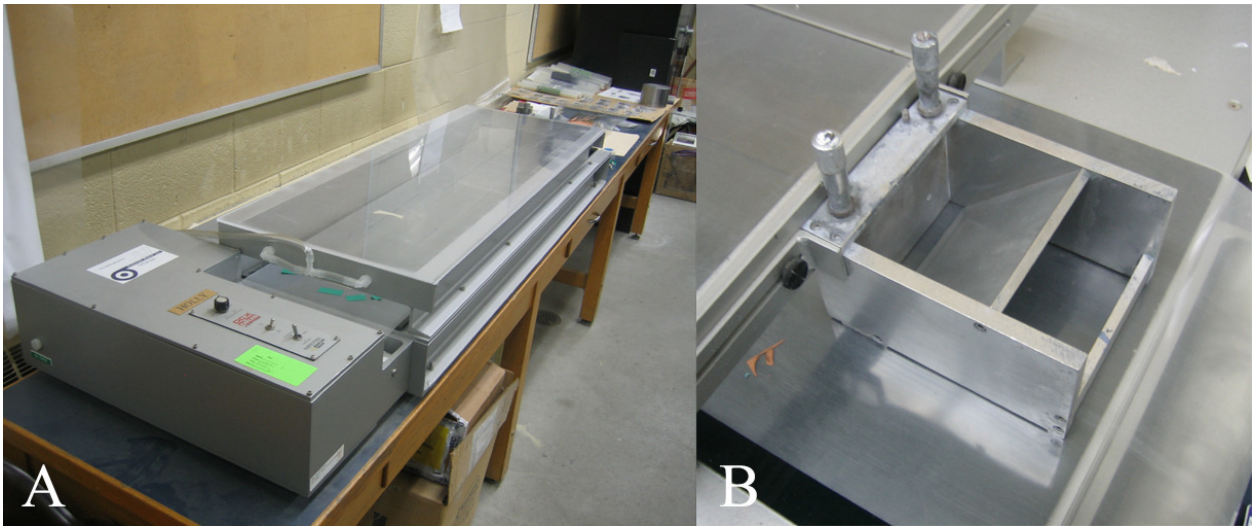

Figure 25: Casting apparatus. A - tape casting machine. B - slip reservoir and adjustable doctor blade.

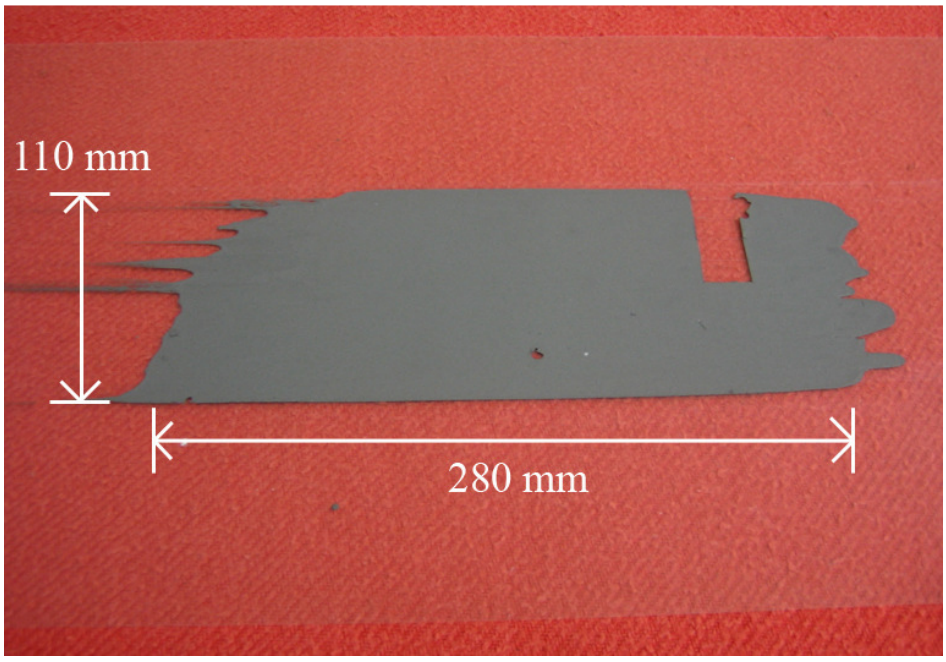

Figure 26: NiTi tape cast sheet

3.2.3 Cutting, Stacking, Pressing

From each of the two tapes a thin rectangular sample consisting of a single layer of tape was cut and pressed at a compaction load of 10000 lbs. A thick rectangular sample was also made from each tape by cutting, stacking, and pressing three layers of green compact together again under a 10000 lb load. The samples were held in a custom rectangular die corresponding to the dimensions of the rectangular samples and pressed using a Carver Laboratory Press (Model C) hydraulic hand press. The dimensions of the pre-sintered pressed samples are summarized in Table 4. The cutting, stacking, and pressing apparatus is presented in Figure 27.

Table 4: Pre-sintered sample mass and dimensions

Tape	Mass (mg)	Thickness (mm)	Length (mm)	Width (mm)
Tape #1 (thick)	791.9	0.84	20.22	12.02
Tape #1 (thin)	240.4	0.26	20.22	12.02
Tape #2 (thick)	594.3	0.58	20.22	12.02
Tape #2 (thin)	203.0	0.22	20.22	12.02

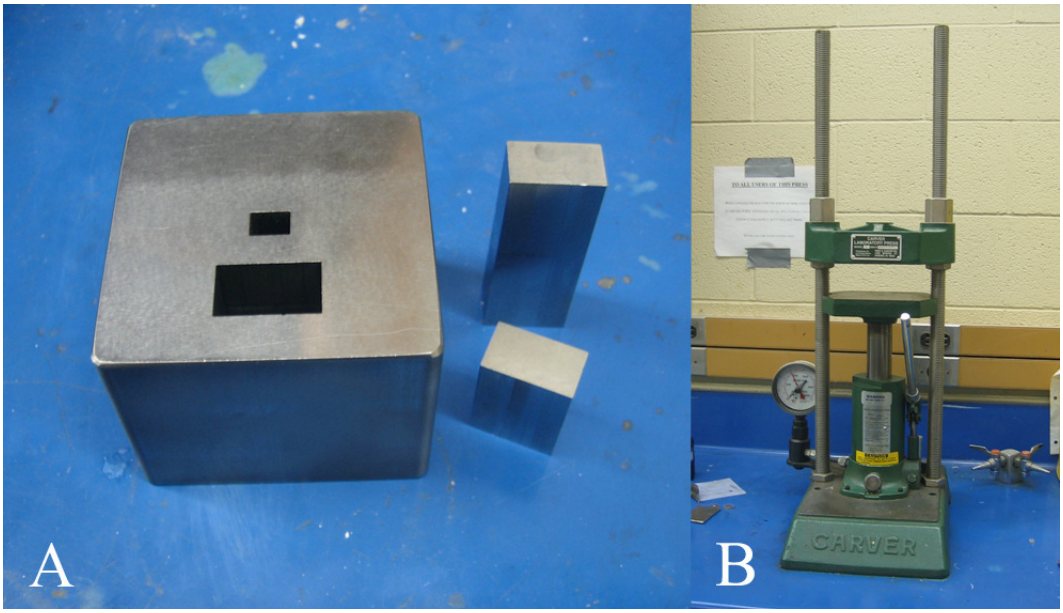

Figure 27: Pressing apparatus. A - rectangular die. B - hydraulic hand press.

The dimensions of the samples were chosen based on availability of equipment and materials. The samples were kept sufficiently small to conserve powders and limit the required compaction forces. Exact dimensions were based on the availability of a suitable die. The samples sizes, provided in Table 4, were large enough to obtain scanning electron microscope (SEM), energy dispersive spectrometer (EDS), and differential scanning calorimetry (DSC) results, as well as provide basic qualitative data on mechanical properties.

3.2.4 Sintering

Sintering was performed in a vacuum furnace manufactured by Centorr Associates Inc. (Model No. 50-4X8-W-A-04S4-H-25) capable of reaching a pressure of $6x10^{-5}$ torr, as shown in Figure 28. Previous studies have shown improved density with hot isostatic pressing (HIP) over conventional vacuum sintering [24], however it was desirable to improve upon the densities of the samples

achievable without the use of HIP. Equipment availability was also a consideration in the decision to use conventional vacuum sintering.

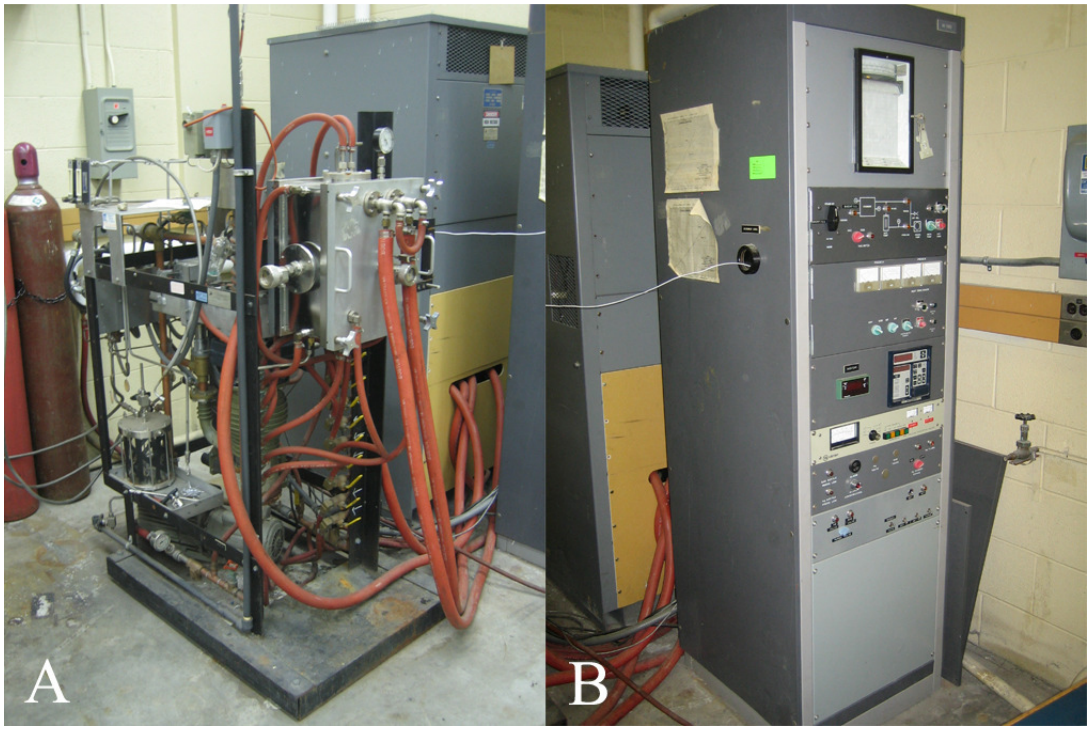

Figure 28: Vacuum furnace. A - chamber, heater, and diffusion pump. B – controller.

Prior to running the sintering profile on the green compacts, a bake out procedure was run within atmosphere to remove the polymer binder. The samples were heated to 400°C and held for five minutes before evacuating the chamber and initiating the sintering profile. The sintering profile used was based on work by Zhang et al. [10]. The complete sintering profile can be found schematically in Figure 29. The samples were first heated to 700°C over a duration of 10 minutes then increased from 700°C to 900°C over a duration of 100 minutes. The heating rate was slowed between 700°C and 900°C in order to avoid combustion synthesis which takes place at direct interfaces of elemental nickel and elemental titanium. Combustion synthesis of NiTi is a relatively

low exothermic reaction that forms NiTi from elemental nickel and titanium and occurs in two modes: self-propagating high-temperature synthesis (SHS), and thermal explosion [46]. Initiation of this reaction is undesirable as combustion synthesis leads to highly porous NiTi, with porosities of 60 vol.% reported by Li et al. [47] utilizing the SHS mode. A lower heating rate allows sufficient time for the formation of intermediate intermetallics thereby suppressing combustion synthesis.

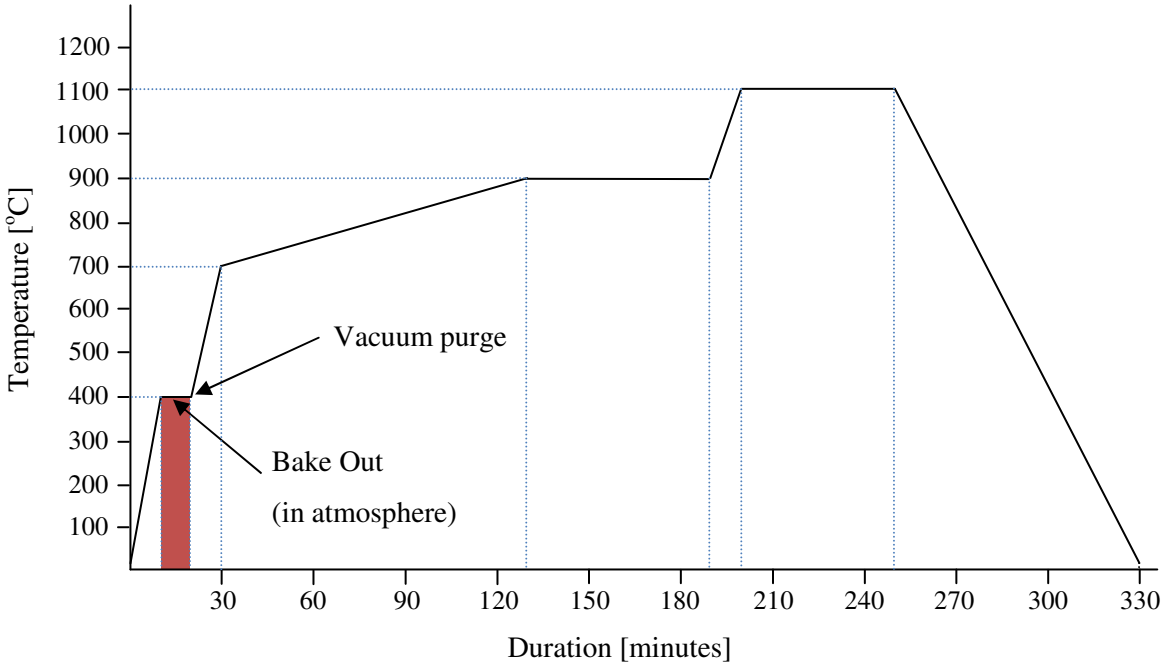

Figure 29: Sintering profile

The samples were then held at 900°C for one hour. Referring to the nickel-titanium phase diagram in Figure 30, 900°C is below the lowest eutectic of βTi and Ti_2Ni at 942°C, thus avoiding the formation of any liquid phase. Finally, the temperature was raised from 900°C to 1100°C over a duration of 10 minutes and held for one hour. Holding at a higher temperature decreased the time required for complete homogenization and could potentially form a transient liquid phase. Referring

again to Figure 30, any Ti_2Ni remaining in the matrix would melt at 984°C, however the NiTi peritectic exists at 1310°C, thus avoiding complete melting. Due to the prior hold time at 900°C, a NiTi matrix will have already formed thus preventing the formation of secondary pores in the presence of the transient liquid phase. Additionally, some of the original pores may be filled by capillary action thus contributing positively to overall density. The samples were then allowed to cool to room temperature over several hours.

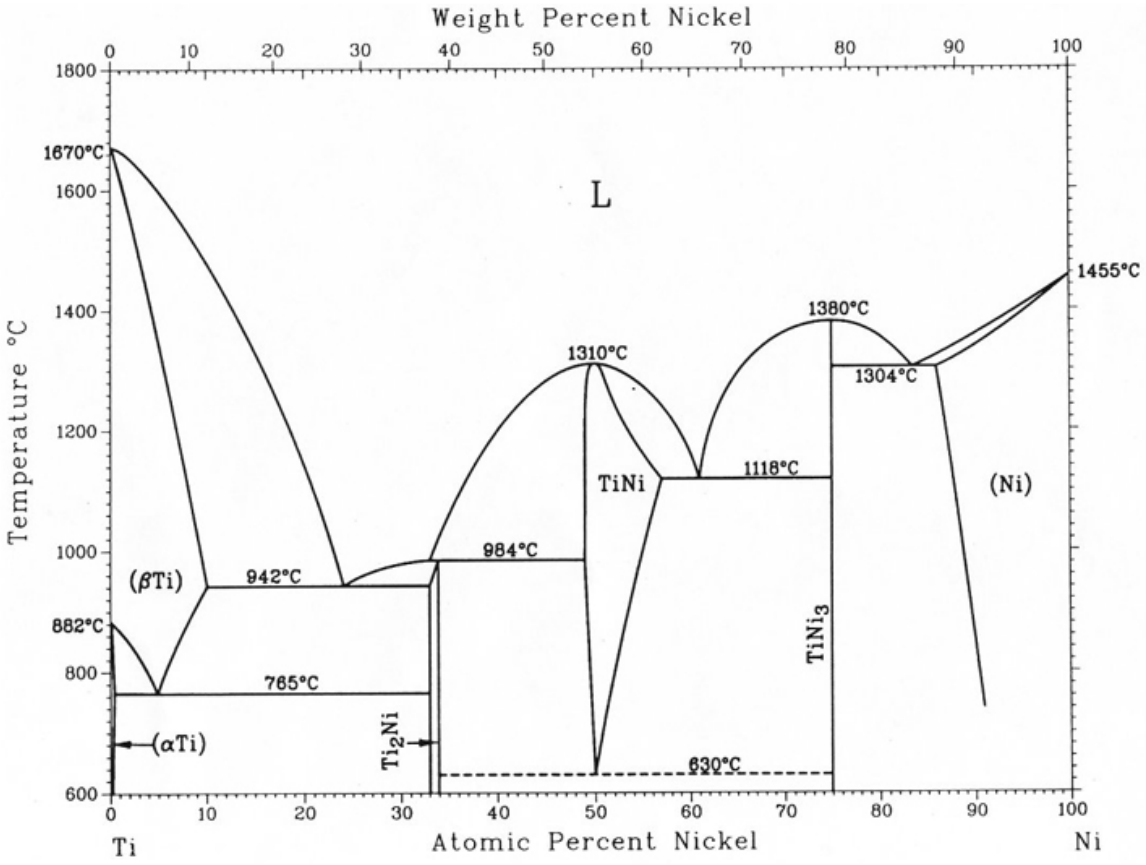

Figure 30: NiTi phase diagram

3.3 Results and Discussion

The following sections present the tape casting and sintering results of the NiTi samples. The physical characteristics of both the pre- and post-sintered compacts are provided in addition to SEM, EDS, and DSC analysis results. The SEM was utilized to obtain pore size and density results and its EDS capabilities were utilized to obtain compositional data of the samples to check for intermediate intermetallic phases and NiTi homogeneity. Finally, the DSC was able to verify the existence of the shape memory effect at the microscopic level in addition to providing a quantitative estimate of the transformation temperatures.

3.3.1 Green Tape and Compacts

The mass and dimensions of all samples were measured after pressing. Three measurements were taken for each dimension using digital calipers and averaged to produce the results summarized in Table 4. A green tape was also pressed and mounted for analysis with the SEM and EDS. The EDS capabilities of the SEM were able to provide verification of the overall relative nickel and titanium composition of 53.4 weight percent nickel, with the scanned region of the NiTi green compact provided in Figure 31. The green tape composition was lower than the initial powder mixture of 54.6 weight percent nickel. This difference may have been due to measurement errors during the initial powder mixing or due to partial separation of the elemental powders. The finer nickel powders may have had a higher affinity to the reservoir and mixing container walls resulting in a slight decrease in nickel from dry powders to cast tape.

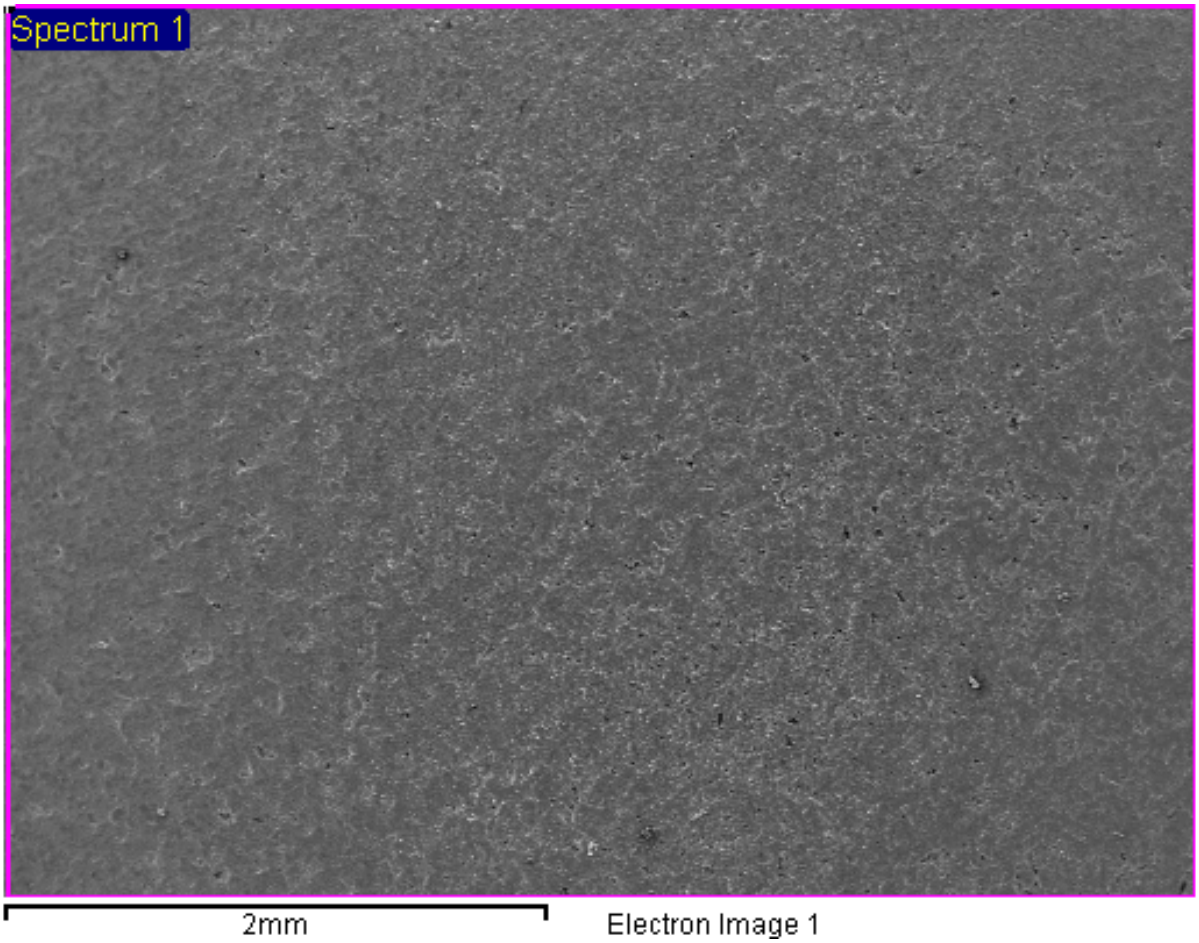

Figure 31: SEM image of green tape compact

3.3.2 Vacuum Sintering Results

The mass and dimensions of all samples were measured after the sintering procedure was complete and used to calculate the post-sintered densities. Three measurements were taken for each dimension using digital calipers and averaged to produce the results summarized in Table 5. The post-sintered dimensions were the same as the pre-sintered dimensions indicating that densification did not occur and a slight decrease in mass occurred likely due to the loss of the polymer binder material.

Table 5: Post-sintered sample mass, dimensions, and densities

Tape	Mass (mg)	Thickness	Length (mm)	Width (mm)	Percent Dense
Tape #1	766.3	0.84	20.22	12.02	85-90
Tape #1 (thin)	236.1	0.26	20.22	12.02	85-90
Tape #2	575.9	0.58	20.22	12.02	87-92
Tape #2 (thin)	199.6	0.21	20.22	12.02	87-92

The post-sintered samples had clearly oxidized on their outer surfaces as seen in Figure 32. Despite operating within a vacuum of $6x10^{-5}$ torr, oxygen was still present during the sintering process which is known to negatively impact the mechanical properties of the NiTi [48] [22]. The oxygen contamination may have originated from the samples themselves due to oxides on the powders prior to tape formation [24], or have been pulled from the alumina stage on which the samples rested during the sintering process. Qualitative analysis revealed that the samples had poor mechanical properties as they were extremely brittle as compared with commercial grade NiTi, possibly due to the oxygen contamination. Samples prepared by elemental PM processes in other studies [10] [48] have also reported lower maximum strains in comparison to conventional fabrication techniques.

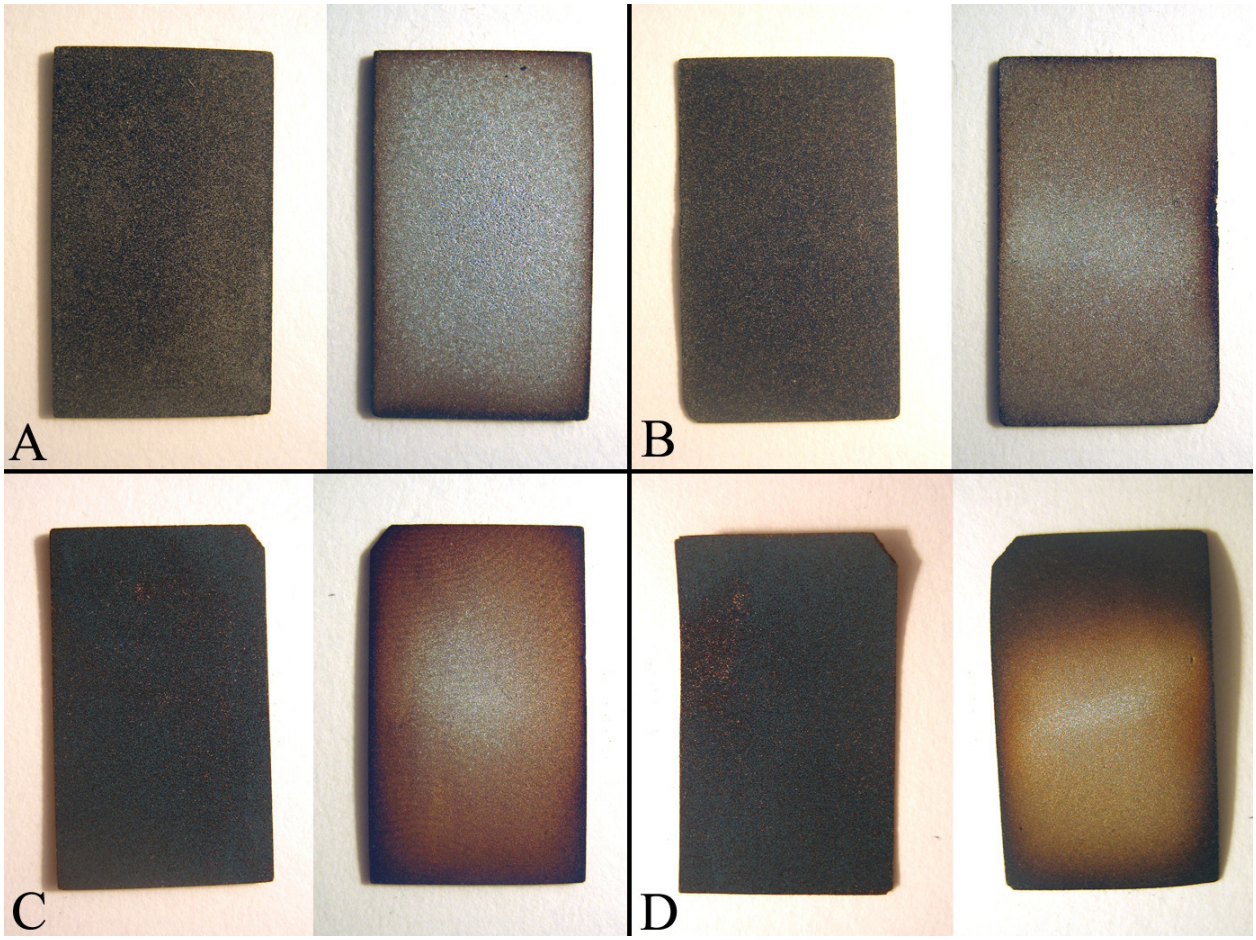

Figure 32: Post-sintered samples with visible oxidation. A - Tape #1 thick sample. B - Tape #1 thin sample. C - Tape #2 thick sample. D - Tape #2 thin sample

3.3.3 SEM and EDS Results

SEM and EDS analysis were performed on the thick samples for each of the tapes. The SEM images at lower magnifications provided insight into the pore size and an additional means of estimating the density of the samples. Utilizing image analysis software (Image Pro), the densities of the Inconel 123 and Inconel 110 samples were estimated to be between 85 to 90 percent dense and 87 to 92 percent dense respectively. This data is summarized in Table 5 and correlates well with samples

prepared by Zhang et al. [10] that utilized a similar process. SEM images of both samples at 50 times magnification are provided in Figure 33.

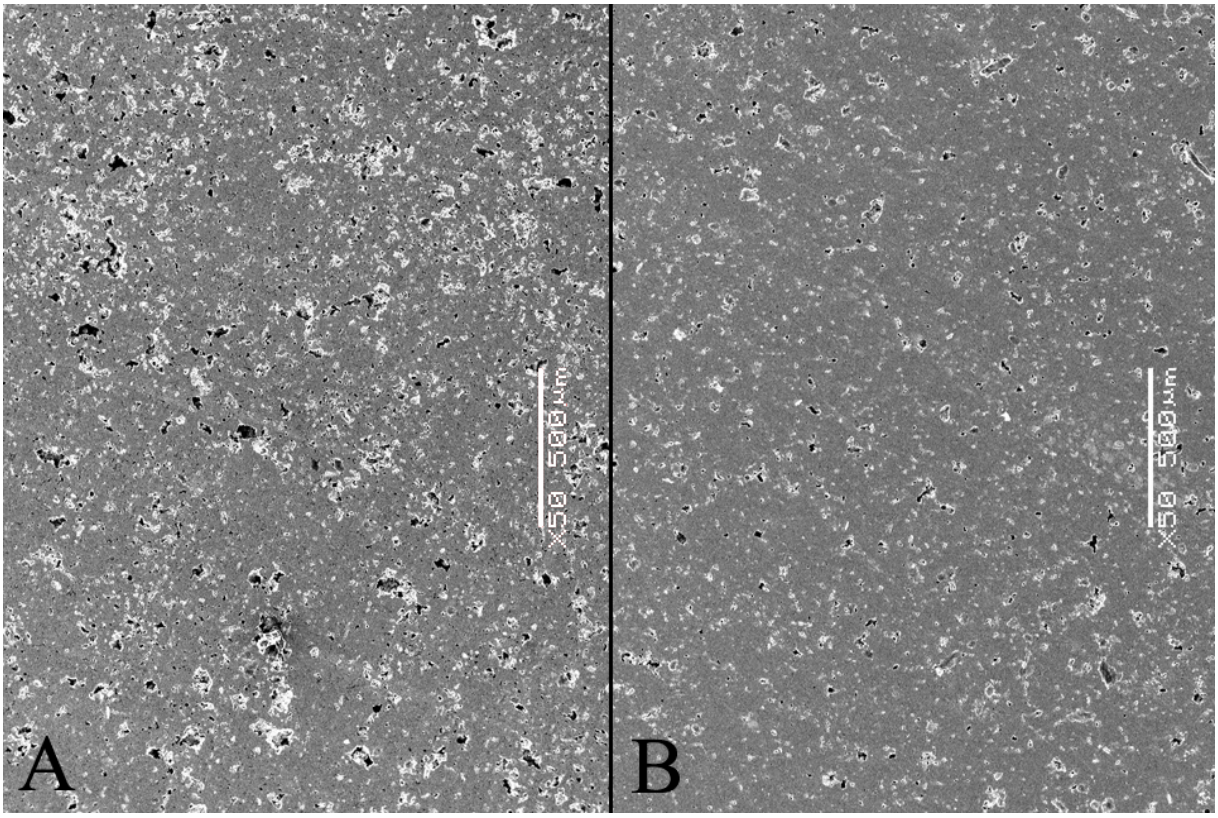

Figure 33: SEM micrographs at 50x magnification. A - Tape #1 Inconel 123. B - Tape #2 Inconel 110.

The SEM's EDS capabilities were used to identify the bulk composition and the phases present in the two thick tape samples. EDS scans were performed over the entire areas shown in Figure 33 and the bulk composition of Tape #1 was found to be 53.6 weight percent nickel and 46.4 weight percent titanium. Tape #2 was found to have a composition of 53.2 weight percent nickel and 46.8 weight percent titanium. These compositions are just outside the range for pure NiTi to form,

and therefore it was expected that some small traces of Ti_2Ni would be found in the analysis. It should also be noted that these compositions differ slightly from the initial powder mixture, but correspond well with the compositions observed in the green tape SEM scans.

EDS scans were performed at areas of interest at higher magnifications for both tape samples. Small, dark, titanium-rich regions were found in both tapes and shown in Figure 34 and Figure 35 with atomic percent compositions corresponding to Ti_2Ni as expected. The presence of the Ti_2Ni intermetallic phase is believed to contribute to the poor mechanical properties of the samples [24]. Despite small regions of Ti_2Ni, both samples were nearly completely homogenous NiTi with no other intermetallic or elemental phases present. EDS scan results for both tape samples are provided in Figure 34 and Figure 35, and Table 6 and Table 7.

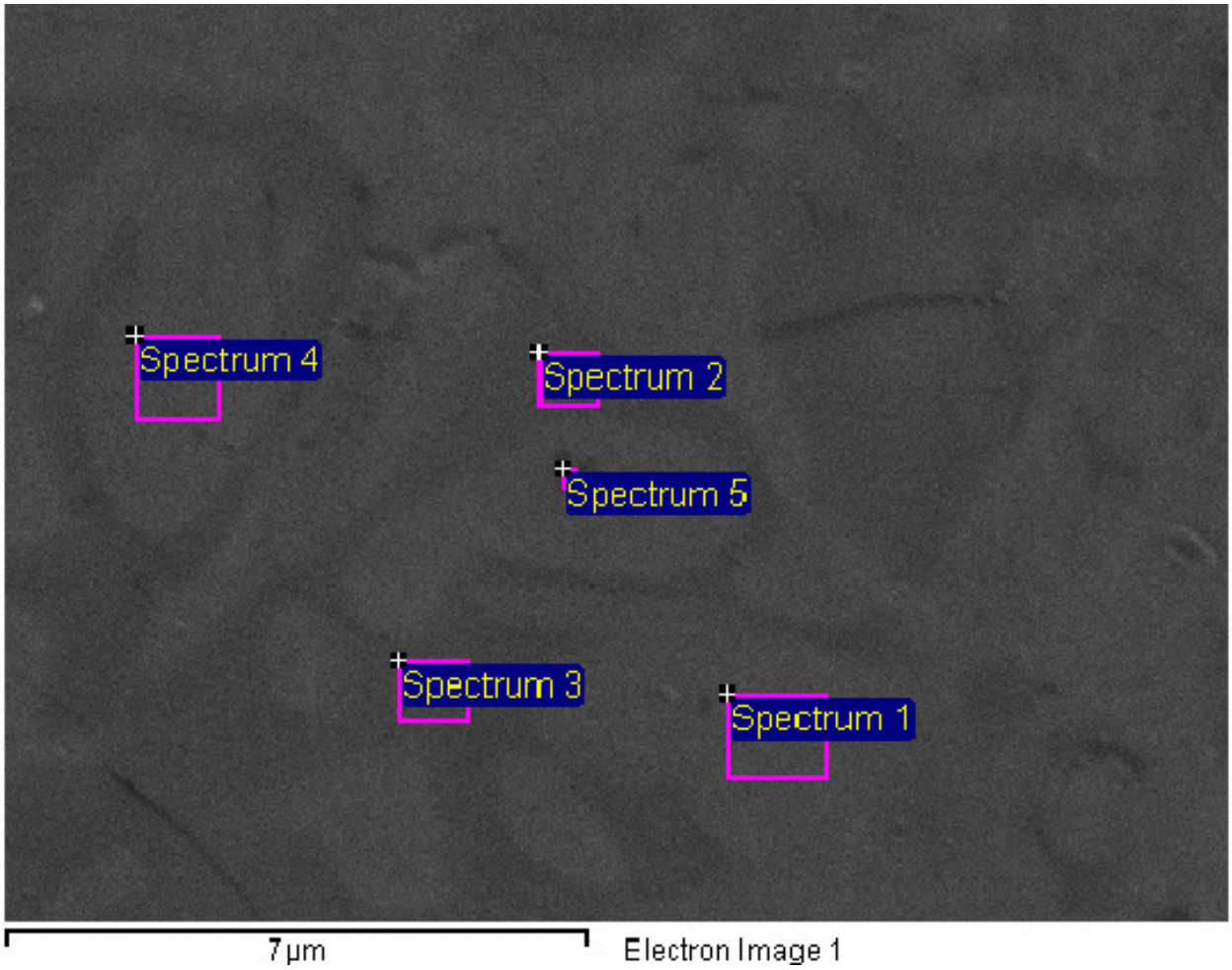

Figure 34: EDS scan of Tape #1

Table 6: Figure 34 EDS scan results for Tape #1

Spectrum	Titanium (atomic %)	Nickel (atomic %)
Spectrum 1	52.85	47.15
Spectrum 2	64.01	35.99
Spectrum 3	62.65	37.35
Spectrum 4	57.97	45.03
Spectrum 5	55.36	44.64

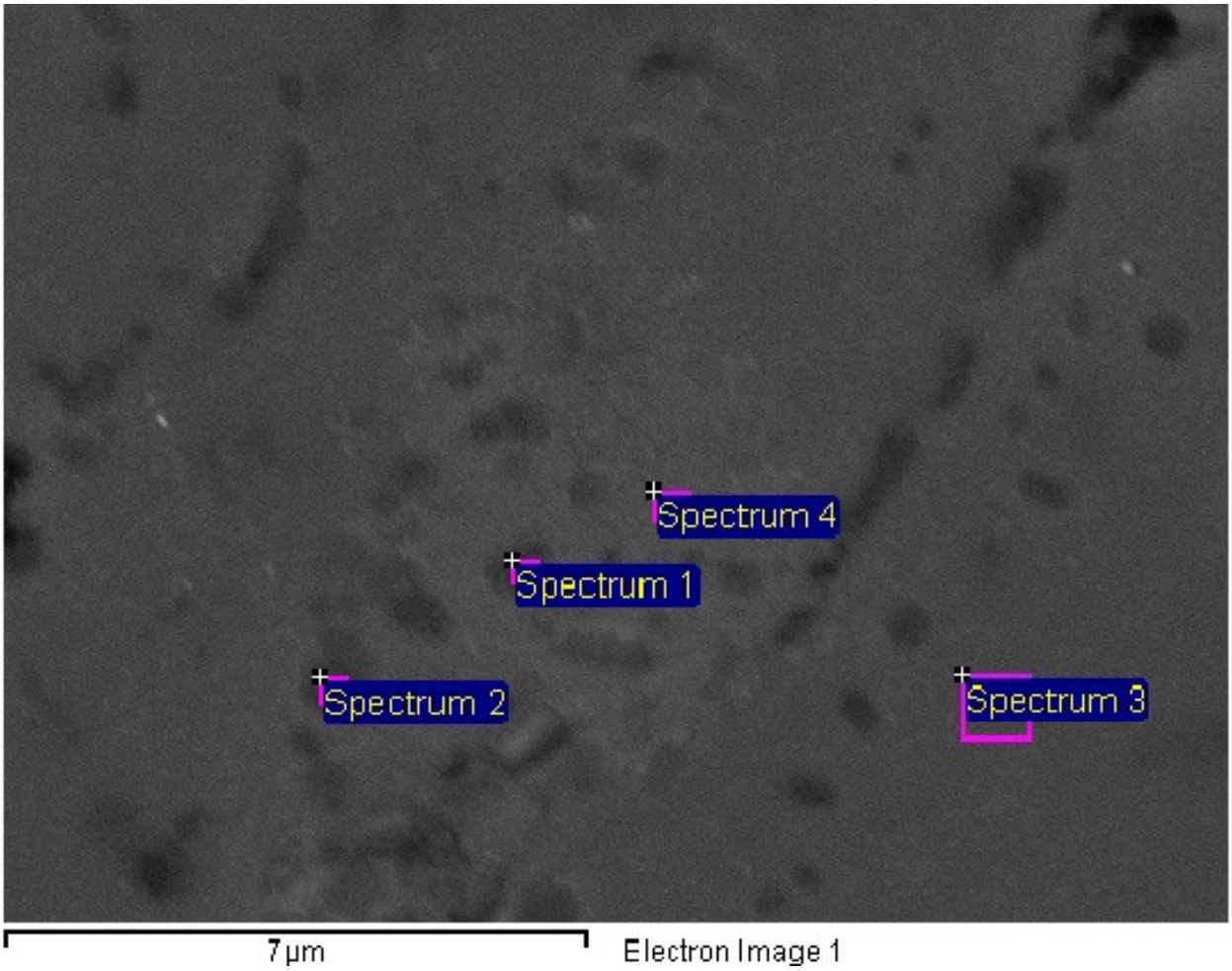

Figure 35: EDS scan of Tape #2

Table 7: Figure 35 EDS scan results for Tape #2

Spectrum	Titanium (atomic %)	Nickel (atomic %)
Spectrum 1	62.67	37.33
Spectrum 2	62.31	37.69
Spectrum 3	49.23	50.77
Spectrum 4	50.64	49.36

3.3.4 DSC Results

DSC scans of both tapes did not result in any useful data pertaining to the existence of the shape memory effect (SME) or the existence of any transformation temperatures. However, the DSC apparatus used to analyze the sintered tapes was only capable of scanning temperatures above room temperature. Therefore, it is possible that the SME did exist, but with an austenite finish temperature (A_f) below room temperature. Further DSC analysis below room temperature is recommended for future work.

3.4 Future Development

The PM results provide a preliminary effort into the fabrication of planar hybrid monolithic SMA actuators. Significant research is still necessary to refine the PM fabrication process in order to achieve SMA materials with mechanical and shape memory properties comparable to those of commercially available bulk alloy. Major obstacles include improved densities, reduction of intermediate phases, reduction of oxygen contamination, and precise control of NiTi composition. This research is focused on the design and feasibility of planar hybrid monolithic SMA actuators and the research necessary to overcome these boundaries is beyond the scope of this work.

For planar geometries, HIP has been proven capable of producing NiTi with higher densities than those obtained in the experiments presented in this research [24]. HIP is also a well established manufacturing technique and it is recommended that the necessary equipment be made available and future tape sintering be performed using this technology rather than standard vacuum sintering.

Currently, work is being performed at the University of Waterloo to verify that oxygen contamination is responsible for the poor mechanical properties of the PM NiTi samples fabricated from standard vacuum and inert atmosphere sintering. X-ray diffraction (XRD), capable of

identifying oxides in the samples, will be employed for this task. Furthermore, studies have also been able to reduce oxygen contamination in powder sintered components through the introduction of a reducing atmosphere during the sintering process [49] and through the use of high-purity pre-alloyed NiTi powders [22]. Based on the results obtained from the XRD analysis, it is recommended that the equipment be made available for the introduction of a reducing atmosphere or reducing agent during the sintering process in an attempt to lower oxygen contamination and improve mechanical properties.

Whitney [45] is studying the underlying processes involved in the fabrication of NiTi from elemental powders and standard sintering techniques. This work should help in the development of a sintering profile capable of obtaining nearly homogenous NiTi without the formation of undesired intermetallic phases. This work may also yield an alternative to HIP if suitable densities can be obtained with transient liquid phase sintering.

Once a NiTi component can be manufactured in-house exhibiting suitable mechanical properties and accurate transformation temperatures, work can then proceed towards the development of hybrid planar components. Tapes of different NiTi compositions can then be pressed together and sintered to form a monolithic component with regions of various compositions (ie. hybrid). However, it is only after we can obtain suitable NiTi properties from a single tape that we will be able to begin analysis of hybrid structures. Therefore, concurrent to the development of PM fabrication techniques a modeling technique was developed to predict the behaviour of first generation hybrid monolithic components that could theoretically be fabricated, and is presented in detail in Chapter 4 of this document.

Chapter 4

Finite Element Modeling and Simulation

4.1 Background and Motivation

The SMA behaviour has been implemented into finite element models numerous times, most notably by Brinson and Lammering [39]. The finite element (FE) approach is not a model in itself, but rather a modeling technique that relies on the numerical integration of a previously developed model of the SMA constitutive behaviour. The SMA constitutive equations, to be readily useful in numerical analysis, must not only accurately describe the material behaviour but, be in a form amenable to numerical procedures. Brinson and Lammering [39] utilized the SMA constitutive equations developed by Brinson [34], based on previous work by Liang, and Tanaka [33] [32]. This thermodynamic constitutive relationship has a relatively simple mathematical expression containing only quantifiable engineering variables and material parameters, thus making it suitable for finite element implementation. Brinson and Lammering [39] provide the derivation and description of the equations necessary for the numerical study of SMAs, resulting in a formulation that differs from the standard finite element formulation for nonlinear truss members only by a simple multiplicative factor. However, this multiplicative factor is still dependent on the various transformation cases that exist, and must be calculated using an additional procedure external to the original finite element routine. This approach to FE implementation of SMA behaviour is similar to other published work [39]. For detailed derivation and implementation of the work done by Brinson and Lammering, refer to the original publication [39].

In this research, rather than deriving the equations for the numerical study of SMAs, all SMA constitutive behaviour was handled external to the finite element solver in conjunction with a commercially available structural mechanics finite element software package. The motivation for this approach was based upon concurrent research by Pai [38], the availability of COMSOL, and its intimate relationship with Matlab. This approach was able to use the same lumped model code developed by Pai [38] in conjunction with the standard solid mechanics finite element formulation provided within COMSOL. Essentially, this approach utilized the COMSOL FE software as a tool for implementing a lumped-element SMA model for the analysis of complex two and three dimensional geometries without significant modification of the FE solid mechanics solver or the original lumped model.

4.2 Shape Memory Alloy Finite Element Integration

The following sections outline the procedure used to integrate Pai's [38] phenomenological SMA lumped model into the COMSOL Multiphysics finite element (FE) environment. Background theory is provided for both the FE structural mechanics routine and the SMA constitutive equations implemented in Matlab.

4.2.1 Finite Element Structural Mechanics Background

The finite element routines are handled by COMSOL Multiphysics's solid stress-strain, static analysis application module. The following sections describe the strain-displacement and stress-strain relationships utilized by the solid stress-strain, static analysis mechanics model and their

implementation into the FE solver. For more details, refer to the COMSOL Multiphysics Modeling Guide [50].

Strain-Displacement Relationship

It is possible to completely describe the strain at any point in a solid using the deformation components and their derivatives. The x, y, and z deformation components are defined as u, v, w respectively. The normal and shear strain components are defined below following the small-displacement assumption.

$$\varepsilon_x = \frac{\delta u}{\delta x} \quad \textbf{Equation 2} \qquad \varepsilon_{xy} = \frac{\gamma_{xy}}{2} = \frac{1}{2}\left(\frac{\delta u}{dy} + \frac{\delta v}{\delta x}\right) \quad \textbf{Equation 3}$$

$$\varepsilon_y = \frac{\delta v}{\delta y} \quad \textbf{Equation 4} \qquad \varepsilon_{yz} = \frac{\gamma_{yz}}{2} = \frac{1}{2}\left(\frac{\delta v}{dz} + \frac{\delta w}{\delta y}\right) \quad \textbf{Equation 5}$$

$$\varepsilon_z = \frac{\delta w}{\delta z} \quad \textbf{Equation 6} \qquad \varepsilon_{xz} = \frac{\gamma_{xz}}{2} = \frac{1}{2}\left(\frac{\delta u}{dz} + \frac{\delta w}{\delta x}\right) \quad \textbf{Equation 7}$$

The strain can then be written in tensor form containing both the shear and normal strain components.

$$\varepsilon = \begin{bmatrix} \varepsilon_x & \varepsilon_{xy} & \varepsilon_{xz} \\ \varepsilon_{xy} & \varepsilon_y & \varepsilon_{yz} \\ \varepsilon_{xz} & \varepsilon_{yz} & \varepsilon_z \end{bmatrix} \quad \textbf{Equation 8}$$

Stress-Strain Relationship

The stress in the material is described using three normal stresses and three shear stresses, assuming symmetric shear stress. These six stresses are arranged into the symmetric stress tensor defined as follows.

$$\sigma = \begin{bmatrix} \sigma_x & \tau_{xy} & \tau_{xz} \\ \tau_{yx} & \sigma_y & \tau_{yz} \\ \tau_{zx} & \tau_{zy} & \sigma_z \end{bmatrix} \qquad \textbf{Equation 9}$$

$$\tau_{xy} = \tau_{yx} \qquad \textbf{Equation 10}$$

$$\tau_{xz} = \tau_{zx} \qquad \textbf{Equation 11}$$

$$\tau_{yz} = \tau_{zy} \qquad \textbf{Equation 12}$$

The stress-strain relationship in linear form can then be written as:

$$\sigma = D\varepsilon \qquad \textbf{Equation 13}$$

Where D is the 6x6 elasticity matrix, and the stress and strain components are written in vector form containing the six stress and six strain components, defined as:

$$\sigma = \begin{bmatrix} \sigma_x \\ \sigma_y \\ \sigma_z \\ \tau_{xy} \\ \tau_{yz} \\ \tau_{xz} \end{bmatrix} \qquad \textbf{Equation 14} \qquad \varepsilon = \begin{bmatrix} \varepsilon_x \\ \varepsilon_y \\ \varepsilon_z \\ \gamma_{xy} \\ \gamma_{yz} \\ \gamma_{xz} \end{bmatrix} \qquad \textbf{Equation 15}$$

The elasticity matrix D, or more commonly used, the flexibility or compliance matrix D^{-1} are defined below for an isotropic material. Where E is the modulus of elasticity and ν is Poisson's ratio.

$$D = \frac{E}{(1+\nu)(1-2\nu)} \begin{bmatrix} 1-\nu & \nu & \nu & 0 & 0 & 0 \\ \nu & 1-\nu & \nu & 0 & 0 & 0 \\ \nu & \nu & 1-\nu & 0 & 0 & 0 \\ 0 & 0 & 0 & \frac{1-2\nu}{2} & 0 & 0 \\ 0 & 0 & 0 & 0 & \frac{1-2\nu}{2} & 0 \\ 0 & 0 & 0 & 0 & 0 & \frac{1-2\nu}{2} \end{bmatrix} \qquad \textbf{Equation 16}$$

$$D^{-1} = \frac{1}{E}\begin{bmatrix} 1 & -\nu & -\nu & 0 & 0 & 0 \\ -\nu & 1 & -\nu & 0 & 0 & 0 \\ -\nu & -\nu & 1 & 0 & 0 & 0 \\ 0 & 0 & 0 & 2(1+\nu) & 0 & 0 \\ 0 & 0 & 0 & 0 & 2(1+\nu) & 0 \\ 0 & 0 & 0 & 0 & 0 & 2(1+\nu) \end{bmatrix} \qquad \textbf{Equation 17}$$

Implementation

The implementation of the above relations are based on the equilibrium equations expressed in the global stress components, given as:

$$-\frac{\delta\sigma_x}{\delta x} - \frac{\delta\tau_{xy}}{\delta y} - \frac{\delta\tau_{xz}}{\delta z} = F_x \qquad \textbf{Equation 18}$$

$$-\frac{\delta\tau_{xy}}{\delta x} - \frac{\delta\sigma_y}{\delta y} - \frac{\delta\tau_{yz}}{\delta z} = F_y \qquad \textbf{Equation 19}$$

$$-\frac{\delta\tau_{xz}}{\delta x} - \frac{\delta\tau_{yz}}{\delta y} - \frac{\delta\sigma_z}{\delta z} = F_z \qquad \textbf{Equation 20}$$

Where F_x, F_y, and F_z denote the respective body forces.

The stress-strain, and strain-displacement relationships are then substituted into the above equilibrium equations resulting in Navier's equation expressed in the displacement.

4.2.2 Finite Element SMA Implementation

In the finite element solid mechanics routines in the previous section, the elastic modulus (E) is a constant value expressed within the compliance matrix. This relationship is suitable for linear elastic material, however, SMAs are not linear elastic. As described in Section 2.4, they exhibit a complex stress-strain relationship with a nonlinear elastic modulus that is dependent upon temperature, stress, and the material stress-temperature history.

Previous finite element implementations of SMA behaviour [39] [51] aimed to redevelop the solid mechanics routines to account for this nonlinear elasticity behaviour. Due to the interdependence of the elastic modulus and stress, these implementations still required an iterative solution approach wherein the model would be broken into small increments of displacement or load. Within each increment the modulus could be updated based on the solution of the previous iteration.

In this research, rather than deriving and implementing the SMA constitutive equations necessary for a numerical study like Brinson and Lammering [39], all of the SMA behaviour was kept external to the FE solver. The standard solid mechanics model for a linear elastic material was utilized in conjunction with a series of Matlab routines capable of predicting the elastic modulus of the SMA under the given conditions. Much like standard FE nonlinear solution techniques, the applied load or displacement was applied over a series of small increments wherein the material properties of the SMA were assumed constant. Between each iteration, the elastic modulus of each element was calculated based on the current FE solution using an external Matlab routine containing the SMA constitutive relationships. This set of updated elastic modulus values was then used within the next iteration of the FE solution. Therefore, the only real change to the standard FE solid mechanics routine was updating the elastic modulus for each element after each iteration. All SMA constitutive behaviour was handled external to the FE solver. For this particular research, the Matlab SMA routines were based on the phenomenological lumped-model developed by Pai [38].

This method was chosen due to the availability and understanding of the Matlab implementation of the phenomenological SMA lumped-model developed by Pai [38], and its ability to be integrated into the COMSOL FE Matlab function environment. The FE architecture developed to work with the external SMA constitutive behaviour could be used with any future MATLAB implementations of SMA behaviour. Therefore any updates or changes to the SMA model could easily be integrated with the FE method. The external SMA behaviour routines compute a two or

three dimensional matrix pertaining to the model geometry containing the distribution of the material's elastic modulus given the temperature-strain data provided by the FE solver after each iteration.

The SMA phenomenological model was implemented as a series of Matlab functions by Pai [38] and utilized as a lumped element model for SMA wire control applications. This code was modified to interact with the COMSOL FE routines provided with the COMSOL Multiphysics software package. A solid stress-strain static analysis model under the structural mechanics module of COMSOL was used as the basic foundation for the SMA FE model. A more detailed explanation of the SMA phenomenological model developed by Pai [38] used in this research can be found in Section 4.3.

4.2.3 COMSOL Integration of SMA Behaviour

The model geometry, material properties, and solver settings are set up in the typical manner as described in the COMSOL Multiphysics documentation with the exception of the elastic modulus. For those elements exhibiting the superelastic or shape memory effect an interpolation function based on external data is used in place of a fixed modulus value. This elastic modulus data encompasses the SMA behaviour and is handled external to the FEM environment by a set of Matlab routines. These Matlab routines are an implementation of the phase and mechanical models described in Section 4.3.

The general approach for implementing the mechanical and phase models describing the SMA behaviour within the FE environment is presented Figure 36. This flow chart describes the key elements and concepts involved, and will be expanded upon further within this chapter.

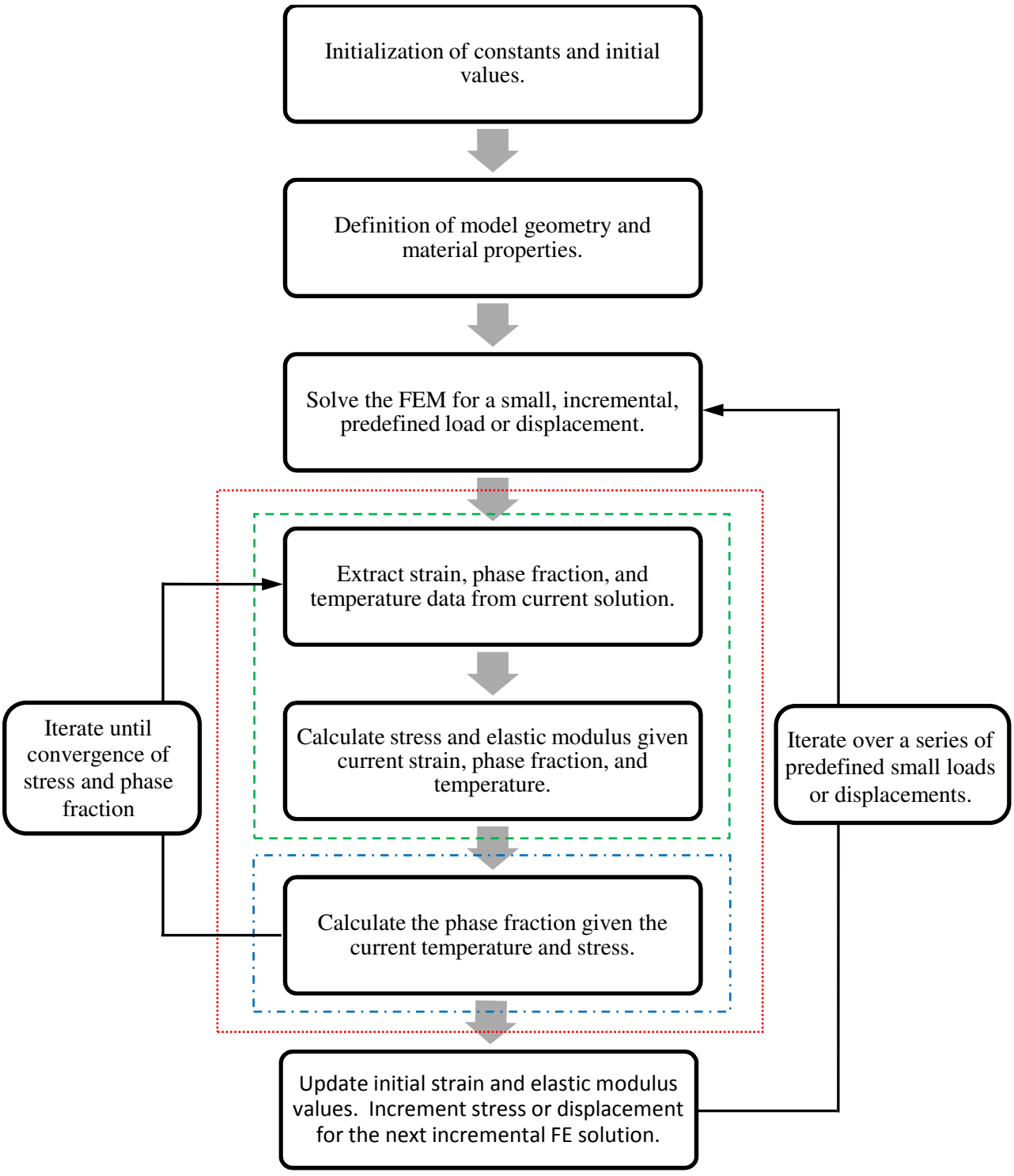

Figure 36: FEM general approach

The entire FE model is run incrementally over a series of small predefined loads or displacements wherein the elastic modulus is assumed constant. This process is necessary due to the complex non-linear behaviour of SMA materials. After each increment, the temperature, strain, and martensite phase fraction from the current FE iteration are used by the mechanical model to compute the stress, and elastic modulus. Since the martensite phase fraction and stress are interdependent, an iterative approach is necessary at every step of the incremental FEM solution. The new stress and temperature values are then passed into the phase model to compute the new phase fraction of martensite. This new phase fraction is then passed back into the mechanical model along with the strain and temperature to re-compute the stress and modulus. This process of passing values between the mechanical model and phase model is performed until convergence is reached. The converged modulus values are then used to update the interpolation functions for the next FEM increment. Poisson's ratio is assumed constant for the entire simulation.

4.2.4 Descriptive Model Flow

1. Initialization

All of the material constants are defined in an initialization function. The SMA material properties, initial state of the material, and program flags are defined and initialized here. Variables of particular interest are the initial strain, elastic modulus, phase fraction, and temperature. It should be noted that all constants, variables, and flags are defined as a matrix of values corresponding to the physical geometry of the material. This grid spacing is defined in step 3, and the values defined here are used to populate the initial grid conditions.

2. Model Geometry

The model geometry is defined within COMSOL Multiphysics' graphical user interface. Information regarding this process can be found within the COMSOL documentation. For the purposes of this work, the entire modeling procedure was run within the Matlab environment. Therefore, once the model geometry is complete it is exported as a COMSOL script and saved as a Matlab function.

3. Interpolation Function Setup

The elastic modulus and strain data that is passed into the FE environment from the Matlab SMA routines is stored and applied to the model as a set of discrete values, distributed over the volume (or area) of the model in the form of a uniformly distributed grid. This grid spacing is defined to be smaller than that of the FE mesh used by the COMSOL solid mechanics solver. The grid spacing and initialization is performed within a custom Matlab function.

4. Definition of External Forces

In order to accommodate the nonlinear SMA behaviour the FE model must be run over a series of small incremental solutions wherein the material properties, particularly the elastic modulus, are considered constant but not necessarily spatially uniform. Therefore it is necessary to define the series of small loads, or displacements, that the series of FE solutions will follow. They can be defined as either constant values or functions depending on the desired application.

5. FEM Setup and Solution

The next stage is the initial setup of the FE solid mechanics application mode. Contained within the FE structure are the boundary conditions, material properties, and initial conditions. The majority of

these values are populated using the constants and initial conditions defined within the initialization routine. Once complete, the FEM solver is called and the first solution corresponding to the first incremental load or displacement is computed.

6. Mechanics Model

The strain values from FE model solution data are extracted as a series of values corresponding to the grid defined in step 3. These values, in addition to the phase fraction, strain rate, temperature, and various program variables are passed into the SMA mechanical model as described in Section 4.3.2. The mechanical model, implemented as a Matlab function, iterates over the entire set of data and returns the stress, elastic modulus, and program variables corresponding to each of the grid points defined in step 3.

7. Phase Model

The current temperature, material constants, and phase fraction, in addition to the stress calculated by the mechanics model in step 6 are passed into the phase model described in Section 4.3.1. The new phase fractions, which correspond to each of the grid points defined in step 3, are returned by the Matlab implementation of the phase model. Since the stress and phase fraction are interdependent, the updated phase fraction value is passed back into the mechanics model in step 6 and new values for the stress and elastic modulus are returned. Steps 6 and 7 are iterated until their corresponding variables converge within a predefined convergence limit.

8. Updating and Saving

The newly calculated elastic modulus and current strain values for every grid point defined in step 3 are then saved and used to prepare the initial conditions for the next step in the series of incremental FEM solutions. The elastic modulus values are stored within the interpolation functions defined in step 3, thus updating the elastic modulus distribution for the next solution. The strain values are passed directly into the initial conditions for the next step in the incremental solution set. The applied load or displacement, as defined in step 4, is updated and the modeling procedure is returned to step 5. This process is repeated until the all desired increments are complete.

9. Solution

Upon completion of the process described in steps 1 through 8, the solution data is exported and presented graphically for analysis.

4.3 Phenomenological Model Description

The phenomenological SMA lumped-model developed and coded into Matlab by Pai [38] was used in conjunction with commercially available FE software (COMSOL). Pai's model is an extension of Madill's model [36] which was based on earlier work by Ikuta [35]. The same properties that make this model an appropriate choice for real-time controls applications make it appropriate for the FE implementation developed in this work. The model has relatively few parameters, matches experimental data well, and is not computationally intensive. The block diagram in Figure 37 and the following sections provide an overview of this phenomenological model.

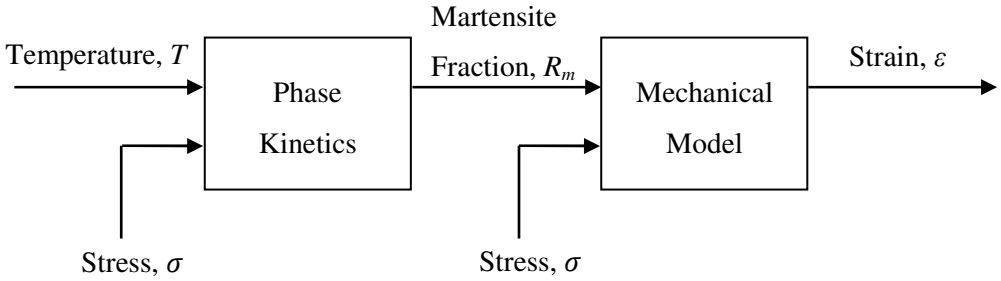

Figure 37: Block diagram of SMA model

4.3.1 Phase Model

The foundation of the phase kinetics model is taken directly from the work done by Ikuta [35], which is a phenomenological model based on the observed behaviour of major hysteresis curve behaviour. Exponential functions were used to describe this behaviour, and material parameters are taken directly from the experimental major loop data. This model was later extended by Madill [36] with the addition of minor loop behaviour and the ability to handle switching between heating and cooling to ensure a continuity of the martensite fraction.

The Ikuta [35] phase model with Madill's extension [36] is provided below.

$$R_m^C(\theta,t) = \frac{R_{ma}^C}{(1+\exp[\mathrm{k_m^C}(\theta-\beta^C)])} + R_{mb}^C \qquad \textbf{Equation 21}$$

$$R_m^H(\theta,t) = \frac{R_{ma}^H}{(1+\exp[\mathrm{k_m^H}(\theta-\beta^H)])} + R_{mb}^H \qquad \textbf{Equation 22}$$

$$\beta^C = \frac{1}{2}\left(M_s + M_f\right) - T_\infty + c_m\sigma \qquad \textbf{Equation 23}$$

$$\beta^H = \frac{1}{2}\left(A_s + A_f\right) - T_\infty + c_m\sigma \qquad \textbf{Equation 24}$$

Where,

c_m : reciprocal of stress rate

k_m^C , k_m^H : cooling and heating constants

$\theta = T - T_\infty$: T is the input temperature and T_∞ is the ambient temperature

R_m^C , R_m^H : martensite fraction when the SMA is cooling and heating respectively

This model was later extended by Pai [38] with the incorporation of time varying stress. This required the re-derivation of the continuity conditions when switching between heating and cooling in order to accommodate the addition of time varying stress. The initial conditions are presented below, along with a visual presentation in Figure 38 of the hysteresis curves with different R_{ma} and R_{mb} values. $R_{mb}(0)$ and $R_{ma}(0)$ are determined from the shape of the major hysteresis loop.

Initial Conditions

$$R_{ma}^C(0) = R_{ma}(0)\left[1 + \exp\left(-k_m^C \beta^C(0)\right)\right] \quad \textbf{Equation 25}$$

$$R_{ma}^H(0) = R_{ma}(0)\left[1 + \exp\left(-k_m^H \beta^H(0)\right)\right] \quad \textbf{Equation 26}$$

$$R_{mb}^C(0) = R_{mb}(0) \quad \textbf{Equation 27}$$

$$R_{mb}^H(0) = R_{mb}(0) \quad \textbf{Equation 28}$$

$$\beta^C(0) = \frac{1}{2}\left(M_s + M_f\right) - T_\infty + c_m \sigma(0) \quad \textbf{Equation 29}$$

$$\beta^H(0) = \frac{1}{2}\left(A_s + A_f\right) - T_\infty + c_m \sigma(0) \quad \textbf{Equation 30}$$

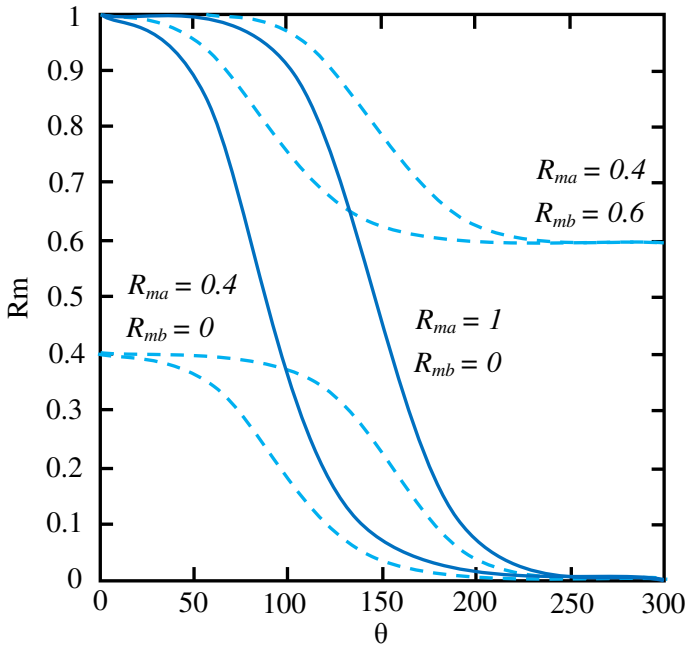

Figure 38: R_{ma} and R_{mb} values for various hysteresis loops

Switching Conditions: Heating to Cooling

$$R_{mb}^{C}(t_s^+) = R_{ma}(0) + R_{mb}(0) - R_{ma}(t_s^+)$$ **Equation 31**

$$R_{ma}(t_s^+) = [R_m^H(\theta_s, t_s^-) - R_{ma}(0) - R_{mb}(0)]\left[\frac{(1+\exp[k_m^C(\theta_s-\beta^C)])}{\exp[-\beta^C k_m^C]-\exp[k_m^C(\theta_s-\beta^C)]}\right]$$ **Equation 32**

Switching Conditions: Cooling to Heating

$$R_{mb}^{H}(t_s^+) = R_{mb}^{C}(t_s^-)$$ **Equation 33**

$$R_{ma}(t_s^+) = [R_m^C(\theta_s, t_s) - R_{mb}^H(t_s^+)]\left[\frac{(1+\exp[k_m^H(\theta_s-\beta^H)])}{(1+\exp[-k_m^H\beta^H])}\right]$$ **Equation 34**

4.3.2 Mechanical Model

The mechanical model is necessary to calculate the elastic modulus and stress of the material given the martensite fraction and strain. The model and code developed by Pai [38] uses the variable sublayer model of Ikuta [35] which was also used by Madill [36]. The Madill model was used to determine the strain in a given material under a constant stress. This was extended by Pai [38] to include pseudoelastic and unloading behaviour. Rather than accepting the martensite fraction and stress as inputs and returning strain as an output, the model was rearranged within the FE code environment to accept the martensite phase fraction and strain as inputs and return the corresponding stress. These values were then utilized to calculate and return the corresponding elastic modulus. The variable sublayer model, which is the core of the mechanical model, is presented in Figure 39. The martensite and austenite are modeled as parallel layers, and the applied stress is distributed while enforcing constant strain.

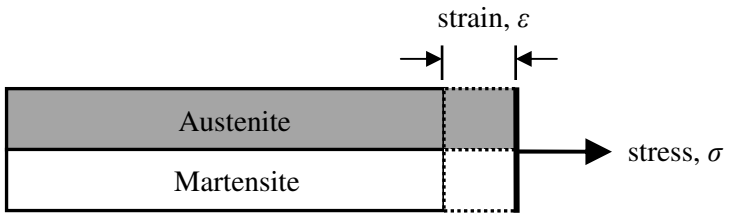

$$\sigma = R_m\sigma_m + (1\text{-}R_m)\sigma_a$$

Figure 39: Variable sublayer model

Within the mechanical model the martensite can be entirely twinned, entirely detwinned, or a combination of both, depending on the applied stress or strain. Similarly, austenite can be pure austenite, stress induced martensite, or a combination of both. As seen in Figure 40, at any given stress or strain there exist several possible regimes wherein various combinations of martensite and

austenite can coexist depending upon the martensite fraction. These regimes, or cases, as numbered in Figure 40 determined the effective modulus of a given state. These cases are outlined as they are implemented within the external software portion of the FE solver. Complete model descriptions and derivations can be found in works published by Pai et al. [37] [38].

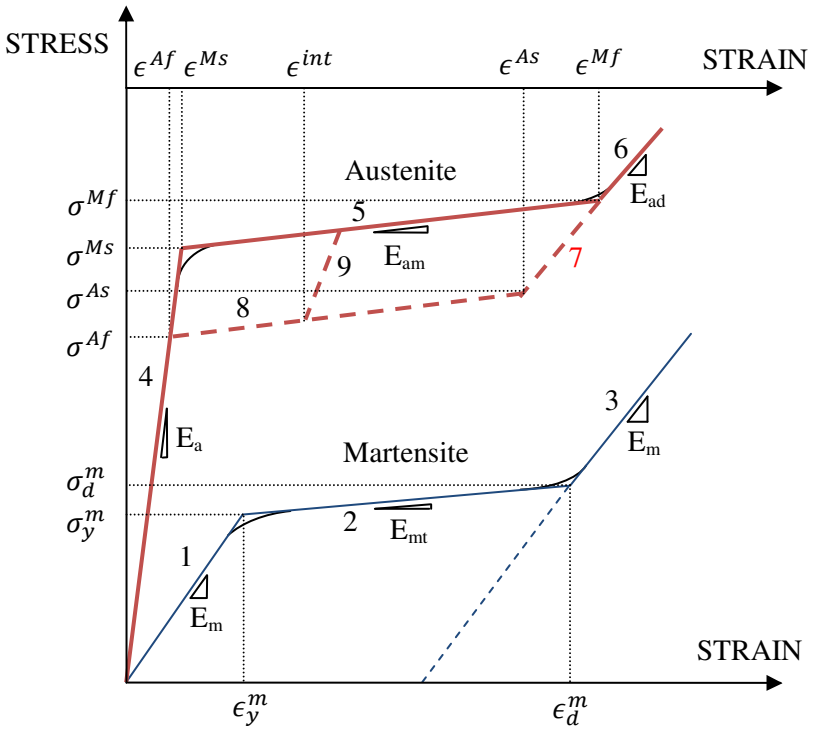

Figure 40: SMA stress-strain-temperature curves

Martensite Loading (1-3)

1: $\varepsilon \leq \varepsilon_y^m$ - martensite fully twinned **(Equation 35)**

$E_{mart} = E_m$

2: $\varepsilon_y^m < \varepsilon < \varepsilon_d^m$ - martensite is a combination of twinned and detwinned **(Equation 36)**

$E_{mart} = E_d$

3: $\varepsilon \geq \varepsilon_d^m$ - martensite fully detwinned **(Equation 37)**

$E_{mart} = E_d$

Austenite Loading (4-6)

4: $\varepsilon \leq \varepsilon^{Ms}$ - no stress induced martensite **(Equation 38)**

$E_{aust} = E_a$

5: $\varepsilon^{Ms} < \varepsilon < \varepsilon^{Mf}$ - combination of austenite and stress induced martensite **(Equation 39)**

$E_{aust} = E_{am}$

6: $\varepsilon > \varepsilon^{Mf}$ - all stress induced martensite **(Equation 40)**

$E_{aust} = E_d$

Before we can introduce the conditions involved with unloading, it is first necessary to define some additional variables. At the point of unloading, we can define the current stress and strain in the material as σ_{unload} and ε_{unload} respectively. The fraction of twinned martensite, fraction of detwinned martensite, fraction of pure austenite, and fraction of stress induced martensite are defined as $R_m^T, R_m^D, R_a, and\ R_{sim}$ respectively.

Martensite Unloading (1-3)

$$E_{mart} = \begin{cases} E_m, & \varepsilon_{unload} \leq \varepsilon_y^m \\ R_m^T E_m + R_m^D E_d, & \varepsilon_y^m < \varepsilon_{unload} < \varepsilon_d^m \\ E_d, & \varepsilon_{unload} \geq \varepsilon_d^m \end{cases} \qquad \textbf{Equation 41}$$

Unloading in 4, 6, 7, 9 - combination of austenite and stress induced martensite

$$E_{aust} = \begin{cases} E_a, \ \varepsilon_{unload} \leq \varepsilon^{Ms} \\ R_a E_a + R_{sim} E_d, \ \varepsilon^{Ms} < \varepsilon_{unload} < \varepsilon^{Mf} \\ E_d, \ \varepsilon_{unload} \geq \varepsilon^{Mf} \end{cases} \quad \textbf{Equation 42}$$

Unloading along 8 - conversion of stress induced martensite into austenite

$E_{aust} = E_{am}$ **Equation 43**

Unloading along 4 (after 8) - elastic unloading of austenite for $\varepsilon \leq \varepsilon^{Af}$

$E_{aust} = E_a$ **Equation 44**

4.4 Validation Simulations

In order to assess the validity of the modeling approach described earlier is this chapter, the FE model is used to predict the behaviour of previously determined SMA geometries. The first and most general test is that of a standard tensile specimen. Secondly, a more complex geometry consisting of a three dimensional SMA actuator designed by Toews [4] is modeled and compared.

4.4.1 Tensile Test

A two dimensional, rectangular tensile specimen (3.048 mm by 55.88 mm by 0.254 mm) was modeled and implemented in the FE SMA model described previously. The model geometry was based on the dimensions of actual tensile specimens presented in Section 5.2.1.1 and used to validate the accuracy of the FE model. The average stress and strain data was computed at each step of the

incremental FE SMA model and plotted in comparison to that of experimentally acquired stress-strain data from actual SMA tensile specimens and presented in Figure 41 and Figure 42. The material parameters required by the model were measured from the experimental data shown.

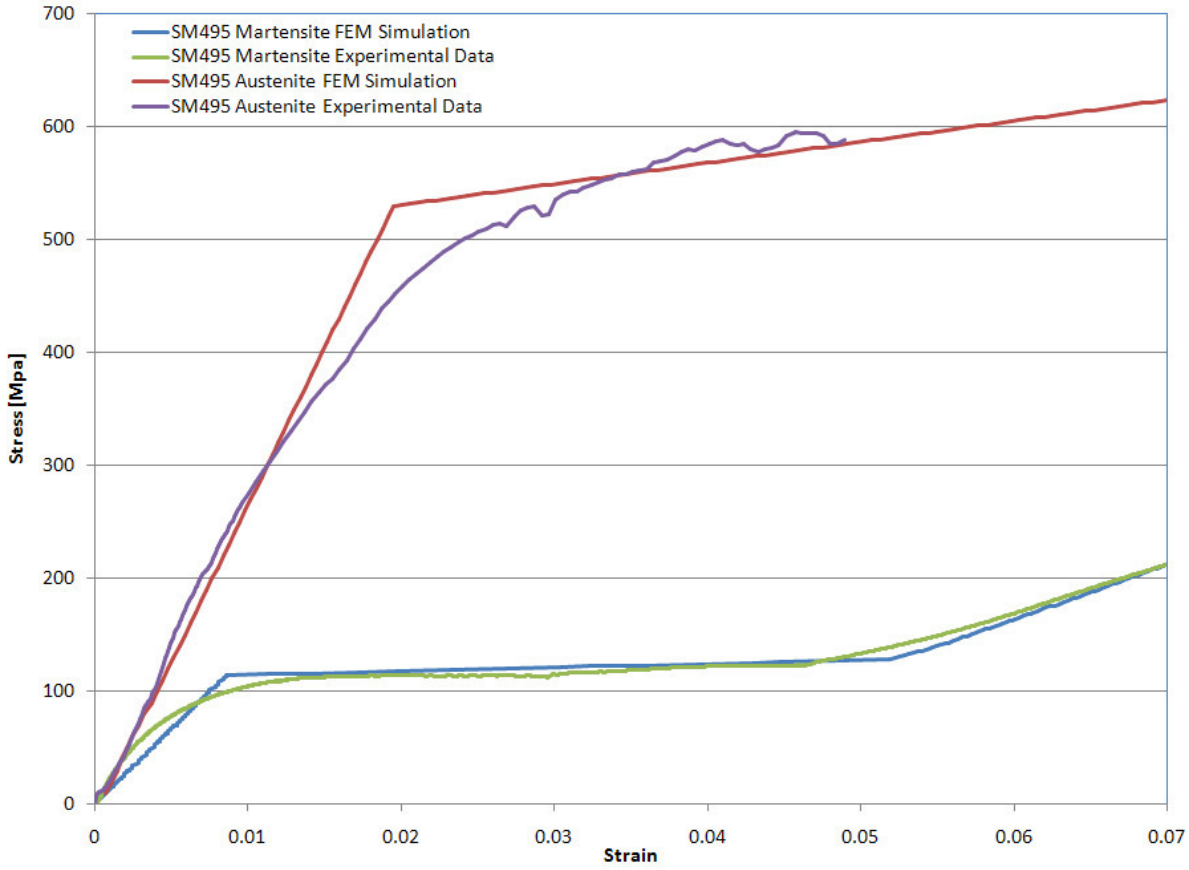

Figure 41: FEM simulation data versus experimental results for SM495 alloy

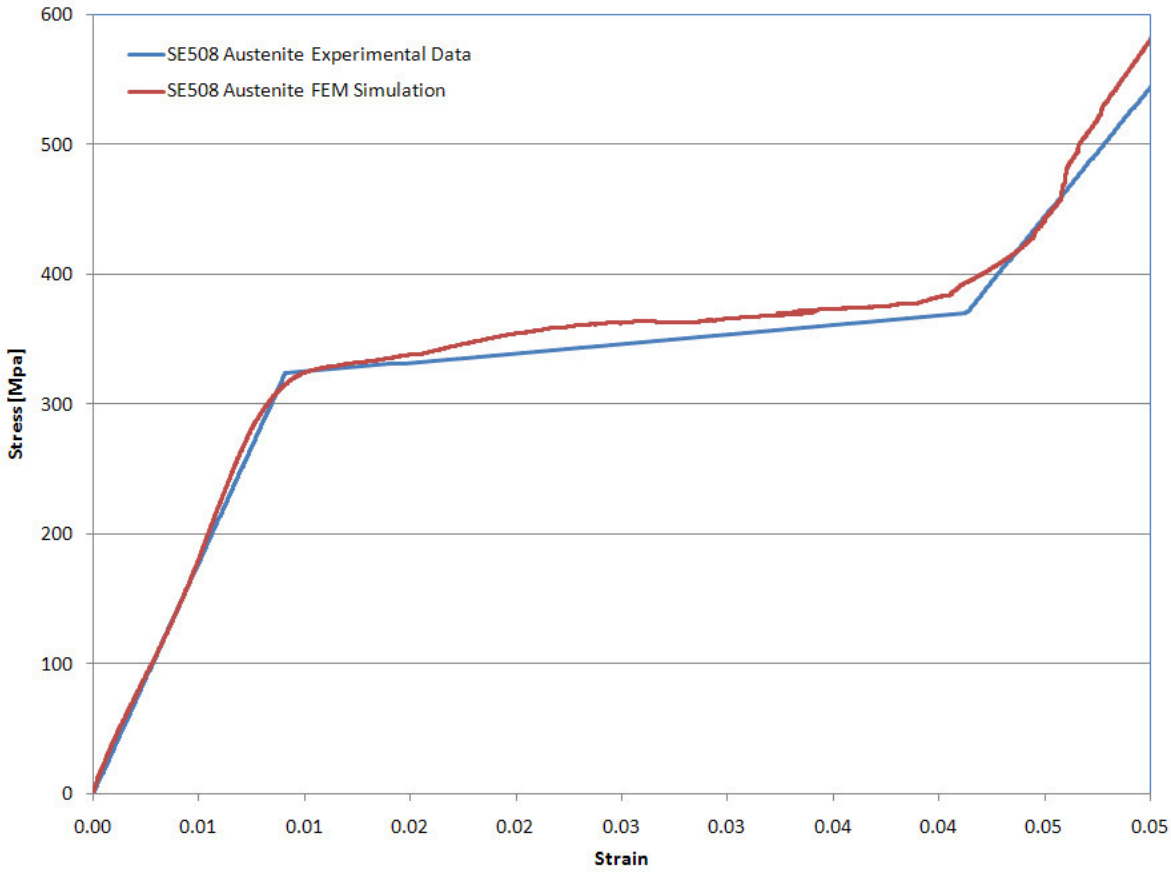

Figure 42: FEM simulation data versus experimental results for SE508 alloy

As seen in Figure 41 and Figure 42, the model agrees well with the experimentally measured data under tensile load.

4.4.2 Comparison with Previous Actuator Design Model

To further validate the model, a more complex three dimensional geometry that includes bending is required. A planar hybrid SMA actuator designed and modeled by Leslie Toews [4] using a lumped-element approach was chosen and implemented in the FE SMA model.

4.4.2.1 Actuator Geometry and Design

A schematic of the actuator dimensions are provided in Figure 43. The actuator was fabricated from a ribbon of cold worked, as received, NiTi that did not exhibit the shape memory effect. Local annealing and shape setting was imparted into a selective region of the planar actuator as indicated by the shaded regions of Figure 43. The constrained geometry during shape setting is provided in Figure 44, position a.

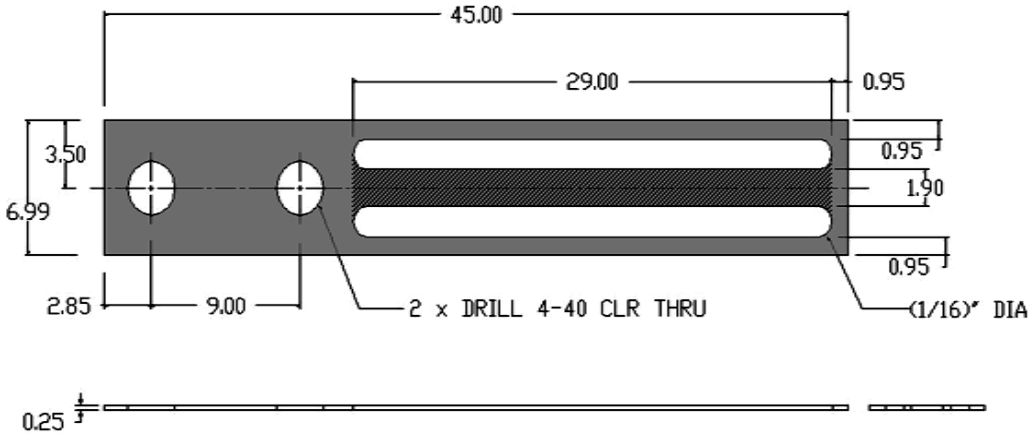

Figure 43: Planar hybrid actuator design (dimensions in mm unless otherwise stated) [4]

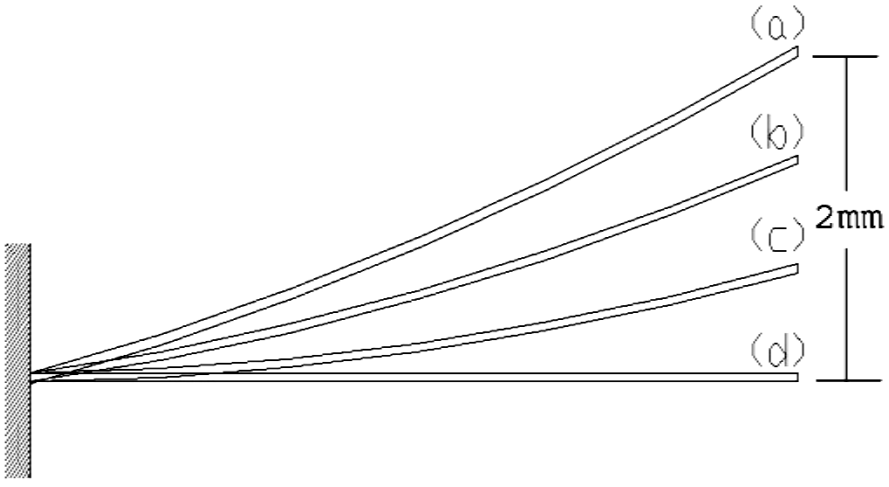

Figure 44: Conceptual actuator operation [4]

The annealed centre region, now exhibiting the shape memory effect, acted as the actuation member while the as received side members, not exhibiting the shape memory effect, acted as the bias or reset mechanism. Figure 44 shows the conceptual operation of the actuator. As illustrated previously, during annealing of the center beam, the actuator is constrained in a curved position with a tip deflection of 2 mm out-of-plane (position a). This sets the memorized shape of the beam at a tip deflection of 2 mm relative to the flat position (position d), while simultaneously storing energy in the as received side members. As the beam cools and martensite forms, the energy stored in the side members causes the tip deflection to decrease (position c). When the center beam is subsequently heated, the transformation to austenite causes it to want to return to its annealed shape, increasing the tip deflection and storing energy in the reset mechanism (position b). Thus, the actuator generates an out-of-plane change in tip deflection during thermal cycling.

4.4.2.2 Simulation Results and Analysis

In order to model the actuator described above using the FE method described in this chapter, an additional modeling step to accommodate the selective annealing operation was performed. In a first step, the actuator was deformed based on the geometry of the annealing fixture (2 mm tip deflection), and annealing was simulated by resetting the stresses in the centre beam (SMA annealed region) while maintaining all other stresses and strains. Deflections at each of the phases were then simulated by running the FE simulation both below the martensite start temperature and above the austenite finish temperature.

The FEM implementation of the planar monolithic actuator is presented below in Figure 45, and summarized in Table 8. The actuator is shown in positions b and c, as defined in Figure 44 with position d represented by the hollow mesh image. The deflection is magnified by a factor of three as indicated. Additionally, the stress distribution is illustrated by surface gradient shading.

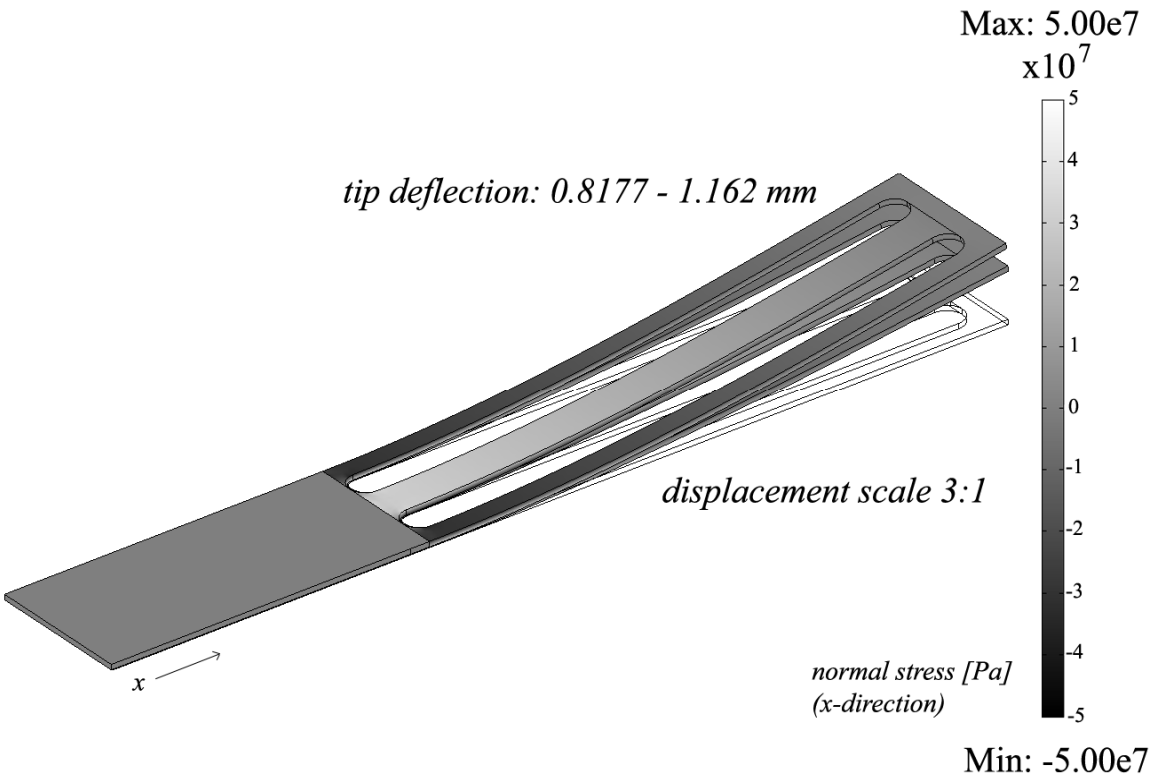

Figure 45: FEM results of monolithic actuator

Table 8: Comparison of predicted deflection from flat state using lumped-element and FE models

Model Type	Martensite Deflection	Austenite Deflection	Cyclic Tip Deflection
Lumped Element	2 – 1.176 = 0.824 mm	2 – 0.832 = 1.168 mm	0.344 mm
Finite Element	0.818 mm	1.162 mm	0.344 mm

As seen in Figure 45, and summarized in Table 8, the FE model results correlate well with the lumped model results obtained by Toews [4]. With only geometry and material properties as a common starting point, the degree to which the predictions correspond provides welcome validation of both the lumped model approach [38] and the FE modeling approach described previously.

Chapter 5

Hybrid Actuator Design and Prototype

Hybrid monolithic actuators offer several advantages over typical monolithic designs. Using the knowledge obtained from the powder metallurgy fabrication investigation in Chapter 3, and the finite element modeling tool developed in Chapter 4, a prototype hybrid monolithic actuator was designed and built. The prototype was designed based on a previous monolithic actuator with the intent of illustrating the improvements made possible by the implementation of hybrid design techniques.

5.1 Hybrid Monolithic Actuators

In this context, the term hybrid refers to a functionally graded material, in which the actuator may contain regions of shape memory, superelastic, and non-active intermetallics and alloys. It remains monolithic in the sense that it is mechanically one piece.

5.1.1 Advantages of Hybrid Monolithic Actuators

Monolithic actuators experience three major disadvantages. First, fabrication of the final shape from bulk material can be difficult and expensive due to the limitations of traditional machining. Secondly, it is difficult to impart local annealing only within the regions of the actuator in which the SME is desired. This thermal control becomes increasingly difficult as the overall size of the device is

reduced. Finally, due to the limited yield strain of the non-annealed restoring medium the range of motion is minimal in comparison with the recoverable strains achievable by most SMAs.

Hybrid monolithic actuators are capable of overcoming these three major disadvantages. These advantages will be outlined below with specific reference to the monolithic actuator developed by Toews [4] and briefly described in Section 4.4.2 of this document.

Fabrication

Utilizing powder metallurgy tape casting techniques we are able to avoid the difficult and expensive shaping methodologies typically used to create monolithic actuators. The chief advantage of the tape casting process is that it is capable of forming large-area, flat sheets that can be cut, stacked, and pressed to form complex planar geometries. Introducing sheets of varying compositions and materials provides a controllable method of manufacturing monolithic actuators with non-uniform, or hybrid, compositions. Once sintered, we are left with a planar near net shape hybrid monolithic actuator. In-depth details of the tape casting and sintering process can be found in Chapter 3 of this document.

Local Annealing

Introducing regions of pure Ni or Ti into the design presented in Section 4.4.2, we are able to eliminate the need for local annealing and precise temperature control. Since pure Ni and Ti do not experience the SME, they are unaffected by the annealing process that occurs at less than half the melting temperature of either metal. Therefore, using regions of either pure Ni or Ti as the restoring portal while maintaining the centre beam as an SMA, the entire actuator could be bulk annealed. However, this does not increase the range of motion of the actuator; in fact, running simulations using the finite element model described in Chapter 4, using both pure Ni and Ti result in reduced tip

deflections of 0.265 mm and 0.305 mm respectively. The reduction in achievable motion is due to the relatively high stiffness of the restoring medium in comparison to the recoverable strain of the SMA. SMAs typically have recoverable strains in the range of 7% [6], however Ni and Ti plastically deform at strains of only 0.03% and 0.12% respectively [52]. Additionally, within the gradient from NiTi to pure Ni or Ti, where the beam and portal join, undesired intermetallics (Ni_3Ti or $NiTi_2$) with poor mechanical properties would likely form, reducing the mechanical robustness of the actuator.

Range of Motion

In order to overcome the limitation imposed by the yield strain of the restoring material, one with strains similar to those recoverable through the SME is required. An actuator restoring medium designed using a material with typical yield strains would have to be tens to hundreds times thinner than the SMA in order to achieve the same degree of elastic deformation. At these thicknesses the recovery force generated is not large enough to reset the thicker SMA beam. By varying the elemental composition of NiTi only slightly, however, it is possible to obtain the so-called superelastic response, with strains of up to 8% recoverable upon unloading [53]. It is proposed, then, to use NiTi in a superelastic composition (typically 56 wt% Ni) as the restoring material. In addition to high yield strains, the similarity in composition reduces the possibility of mechanical problems at the material interface, since both superelastic and shape memory compositions are within the same material phase. However, the difficulty with using superelastic NiTi for the portal with the existing geometry is that local annealing is again required if the residual stresses required to restore the actuator are to remain in the portal after annealing. This is because superelastic NiTi material, unlike pure Ni or Ti, is susceptible to the annealing operation.

5.1.2 Design of Hybrid Monolithic Actuators

A design technique to incorporate the benefits of both bulk annealing and the addition of superelastic material is shown in Figure 46. The technique involves a partial separation of the actuator, allowing deformation of the SMA beam independent of the superelastic portal as seen in Figure 46b. Annealing in this state sets the desired shape of both materials. The left regions of the actuator are then secured together forming the final state of the actuator as seen in Figure 46c. Using the same physical dimensions as the monolithic actuator from Section 4.4.2, with the incorporation of hybrid design technology we are able to obtain simulated deflections in the range of 2.5 mm without the need for a complex manufacturing and annealing process. This was an increase in tip deflection of approximately 700 percent in comparison to that of the traditional monolithic actuator design. Figure 47 shows FEM simulations of displacements achievable with the traditional monolithic actuator and the hybrid monolithic actuator. The visual displacement is amplified by a factor of three in Figure 47a, so that the displacement of the monolithic actuator is visible.

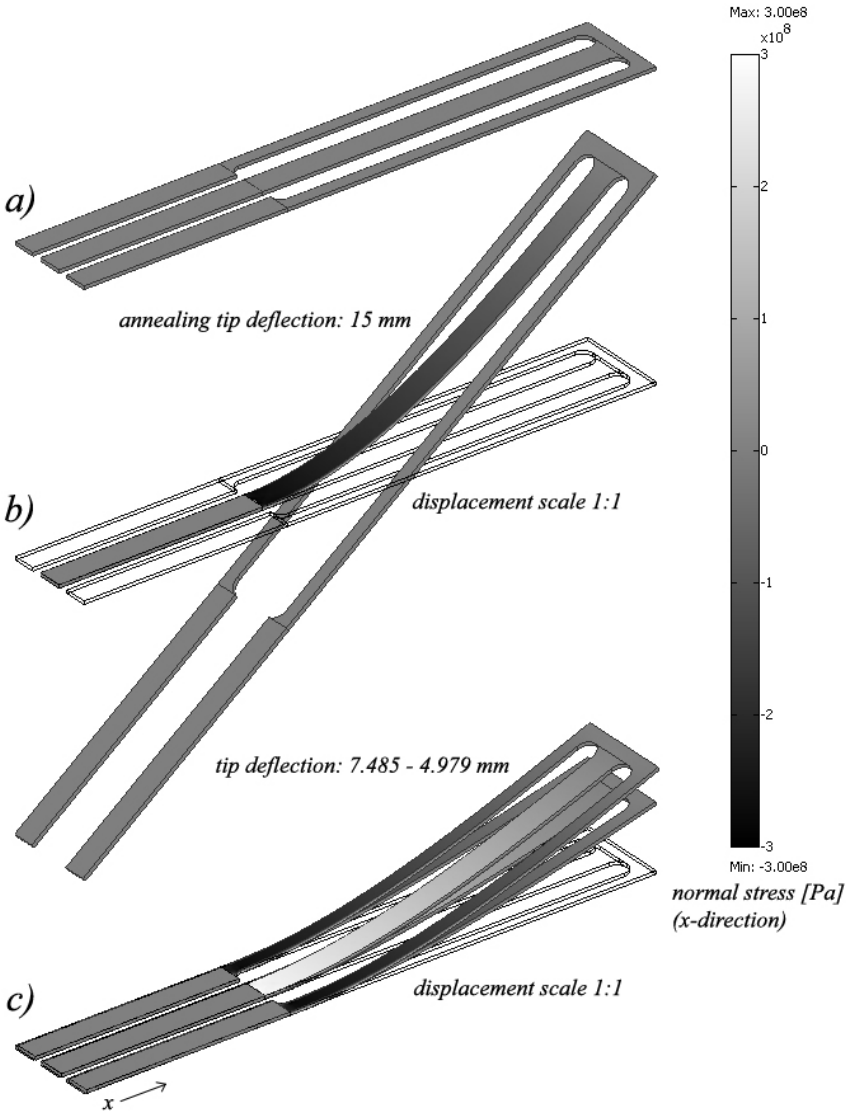

Figure 46: FEM model of hybrid monolithic actuator

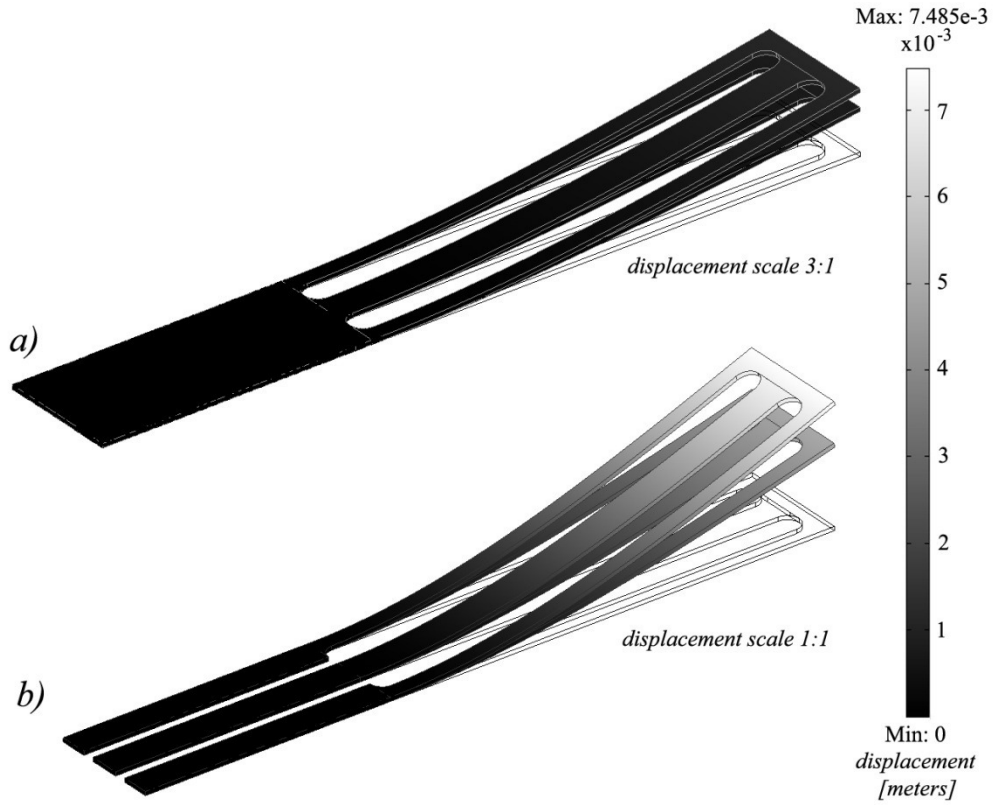

Figure 47: Actuator displacement comparison using FEM

Despite the significant increase in achievable deflection, the proof-of-concept hybrid actuator remains within the region of linear elastic deformation and does not take full advantage of the superelastic capabilities, as illustrated in Figure 48. It is also worth noting that the powder metallurgy approach allows the material composition to be precisely controlled. By tailoring the composition of the superelastic restoring material, the plateau stress can be controlled [12]. By exploiting this additional design flexibility and exploring different geometries, future actuators could theoretically attain even greater ranges of motion than the present proof-of-concept design presented in this section, as illustrated in Figure 49.

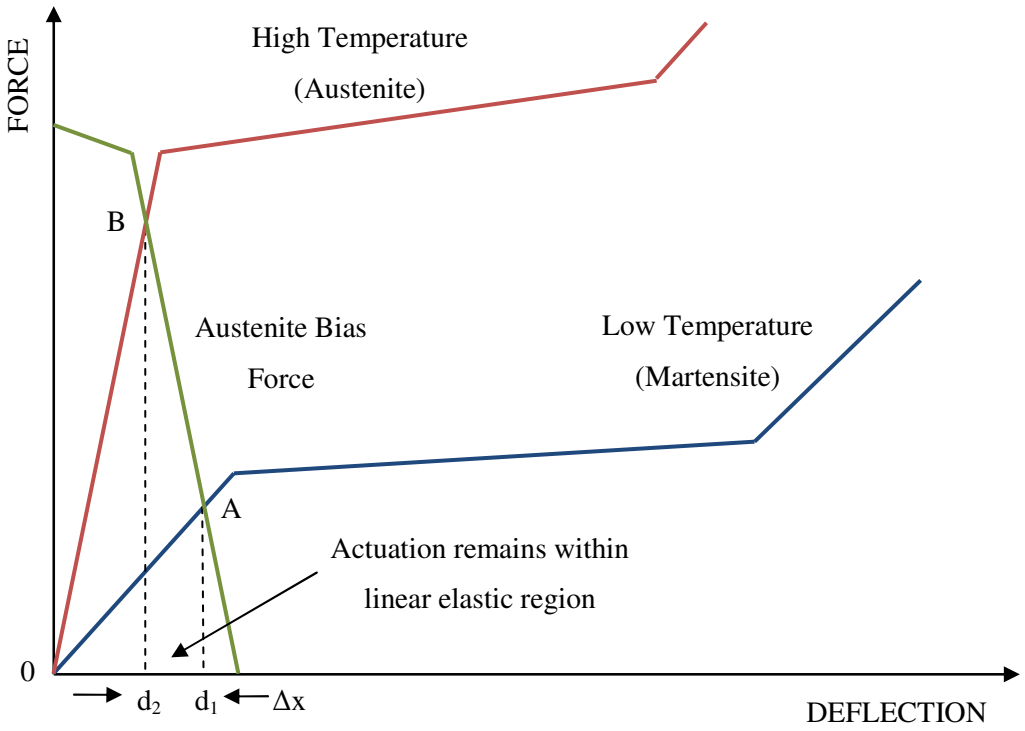

Figure 48: Hybrid actuator design within linear elastic region

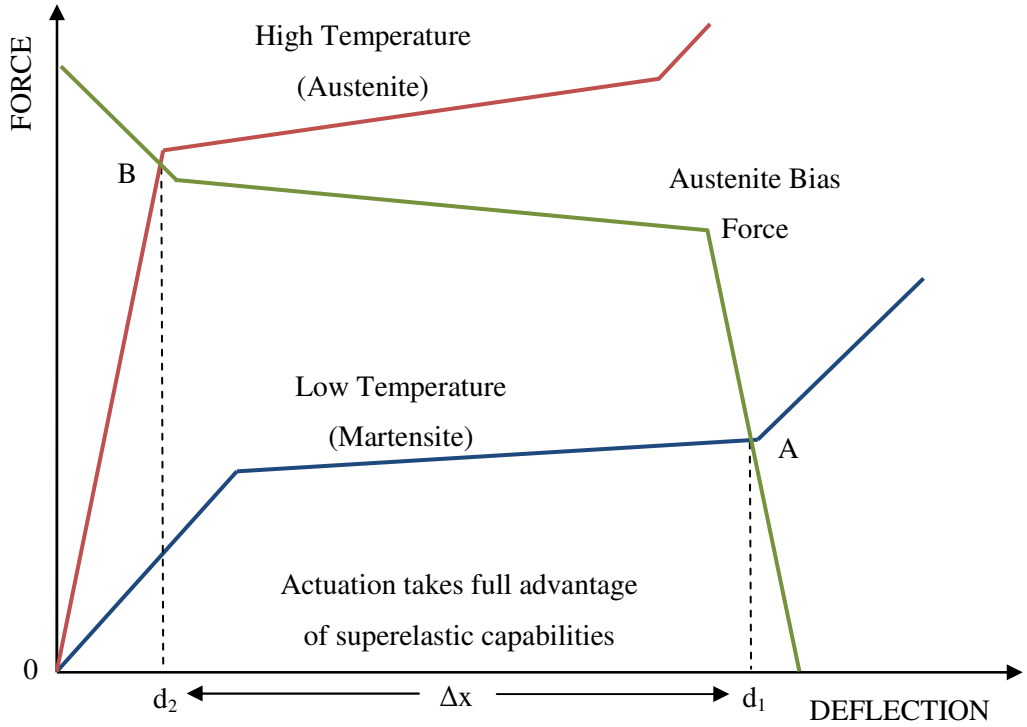

Figure 49: Optimized hybrid actuator design

5.2 Prototype Design

Based on the proof-of-concept hybrid monolithic actuator design presented in the previous section, a prototype was designed using materials and equipment available. The mode of operation was based on the three-beam, out-of-plane deflection actuator designed by Toews [4], with dimensions comparable to Toews' actuator. The tape casting powder metallurgy (PM) fabrication technique described in Chapter 3 was unable to produce NiTi material with mechanical properties comparable to that of commercially available bulk NiTi. Specifically, the material fabricated using the PM approach was prone to brittle failure and unsuitable for actuator fabrication at the time of this thesis.

Therefore, the actuator was designed and fabricated using two commercially available NiTi ribbons exhibiting both the SME and superelastic behaviour. This design was not a true hybrid

monolithic actuator in that several materials were joined using conventional joining techniques. However, the prototype was still capable of exhibiting the hybrid concept and mechanical attachment suitable for proof-of-concept purposes was not difficult with the prototype actuator dimensions.

5.2.1 Shape Memory Alloy Material Characterization

SMA material was acquired from Nitinol Devices and Components based on availability and similarity to the previously designed monolithic actuator. Superelastic material, part number SE508, was obtained in 0.5 inch wide ribbon with a thickness of 0.015 inches. SMA material, part number SM495, was obtained in 0.275 inch wide ribbon with a thickness of 0.010 inches. SM495 was the material used for the prototype monolithic actuator in [4].

5.2.1.1 Tensile Tests

Tensile specimens were water jet cut from the as-received material with dimensions shown in Figure 50. Two specimens were cut from each material type. The as-received material did not exhibit the superelastic or SME and it was therefore necessary to anneal the material before obtaining its material properties. All four samples were heat treated simultaneously in an open atmosphere furnace at a temperature of 500^{o}C for 15 minutes and water quenched. The samples exhibited a slight curvature, presumably from being stored on a roll, and were therefore constrained between two flat bricks during the annealing process.

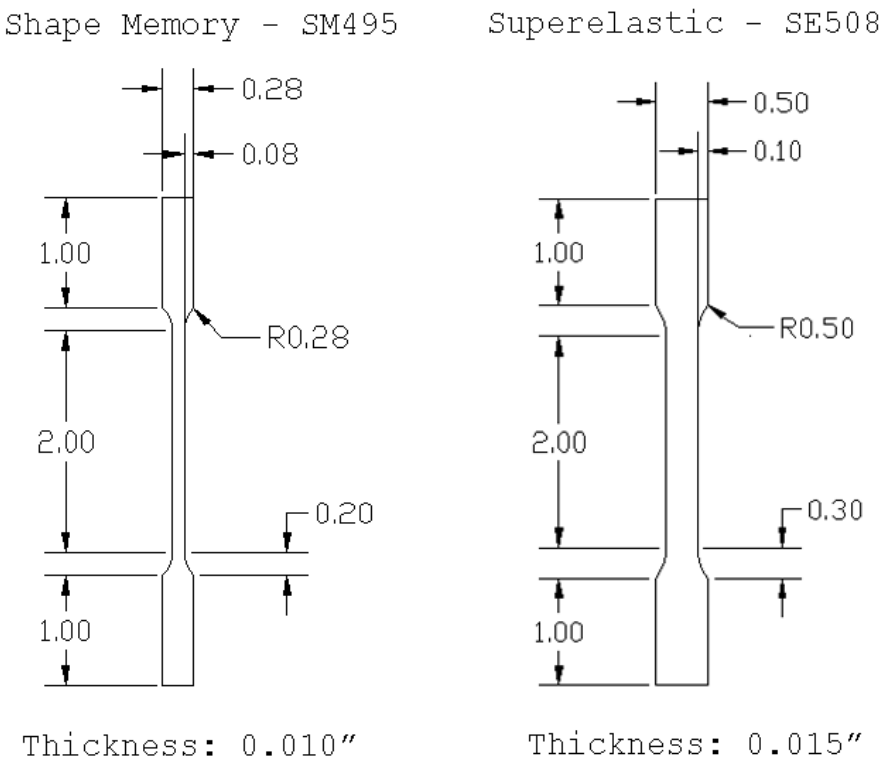

Figure 50: Tensile specimen. Dimensions given in inches.

Several tensile tests were performed at room temperature on each of the samples, which were re-annleaed at 500°C for 5 minutes and quenched between each pull. An Instron 4465 tensile tester was used in conjunction with a United Extensometer (model no. EZ5-50).

In order to obtain high temperature austenite data for the SM495 material (martensite at room temperature) the tensile specimen was heated using a 1100 W heat gun above its austenite finish (A_f) temperature during the tensile test. Specimen temperature was monitored by a thermocouple taped to the back of the specimen, centered vertically. Strain data was obtained directly from the grip displacement during the high-temperature tests, due to fears of damaging the extensometer. Again,

several pulls were performed on the same sample, which was re-annealed at 500°C for 5 minutes and quenched before each test. The apparatus is shown in Figure 51.

Figure 51: Tensile test apparatus; A - Instron tensile tester; B - Strain gauge

The results of the tensile tests are summarized in Figure 52 and Figure 53. The load displacement data returned by the tensile test software was used in conjunction with the samples' gauge length and cross-sectional areas to calculate their respective stress-strain curves. Data was not obtained for unloading conditions due to the limited capabilities of the tensile test apparatus. The Instron 4465 is only capable of position control and therefore incapable of maintaining a constant load under external influence.

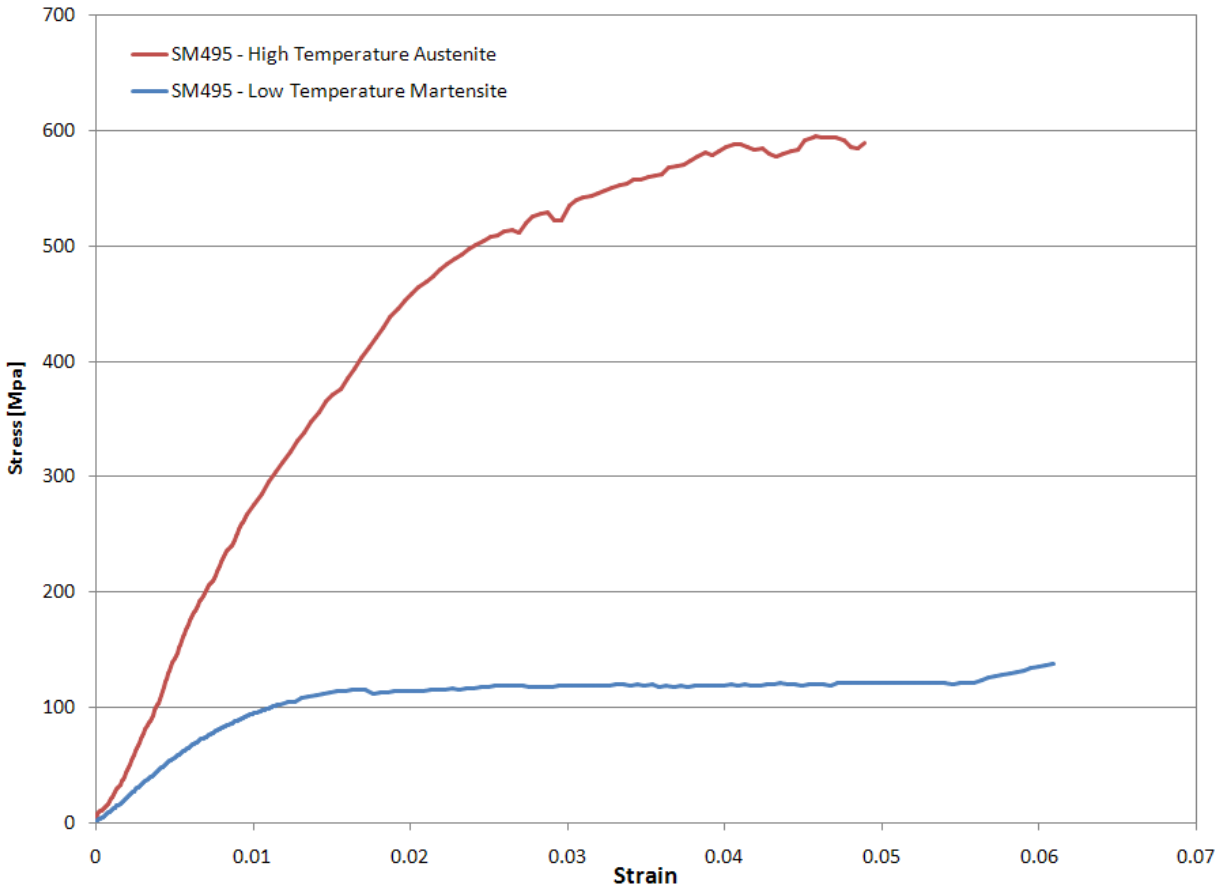

Figure 52: SM495 stress-strain curves

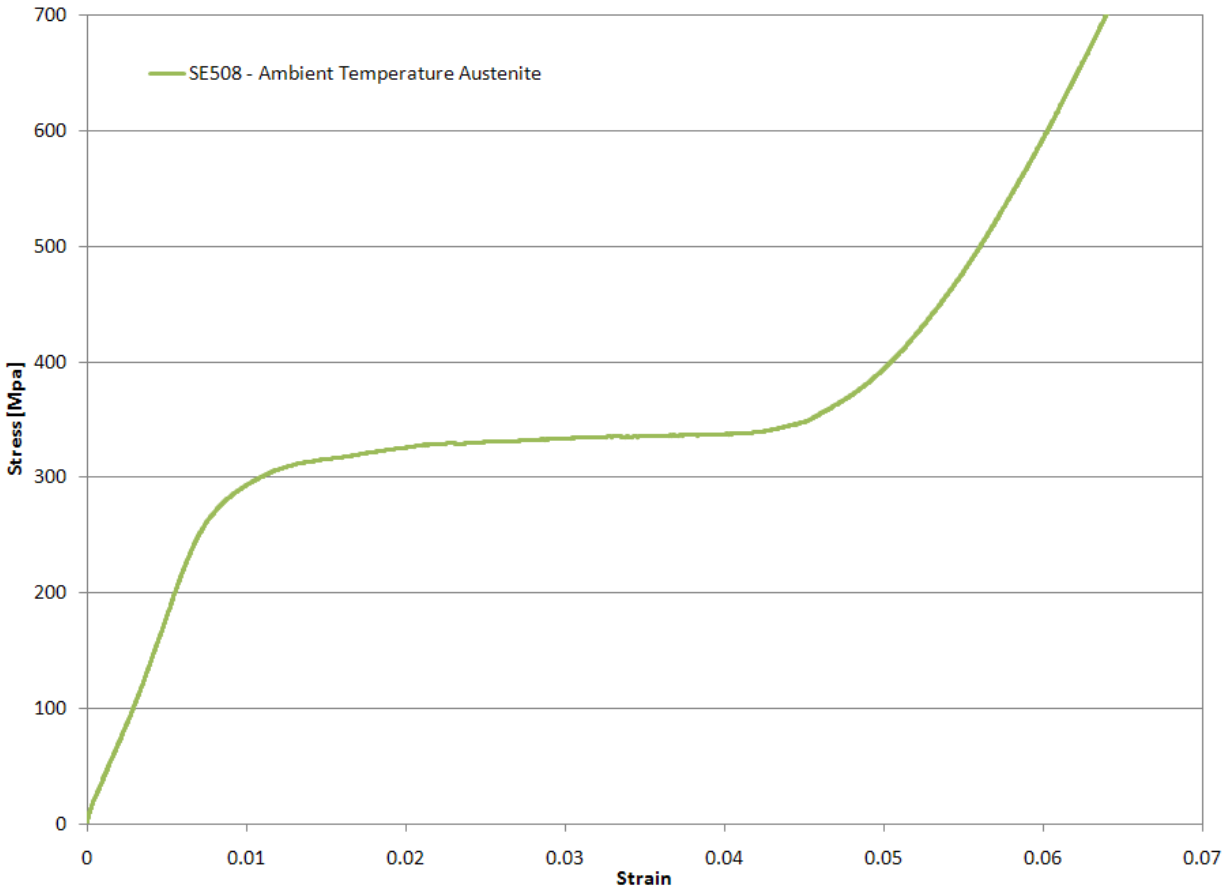

Figure 53: SE508 stress-strain curve

5.2.1.2 DSC Characterization

According to the manufacturer, the room temperature martensite material, SM495, has an austenite transformation temperature of 60°F. No other physical properties are provided by the manufacturer. In order to obtain more accurate data regarding the martensite and austenite start and finish temperatures (M_s, M_f, A_s, A_f) a DSC analysis was performed on the material. The results are presented in Figure 54, with the transformation temperatures summarized in Table 9.

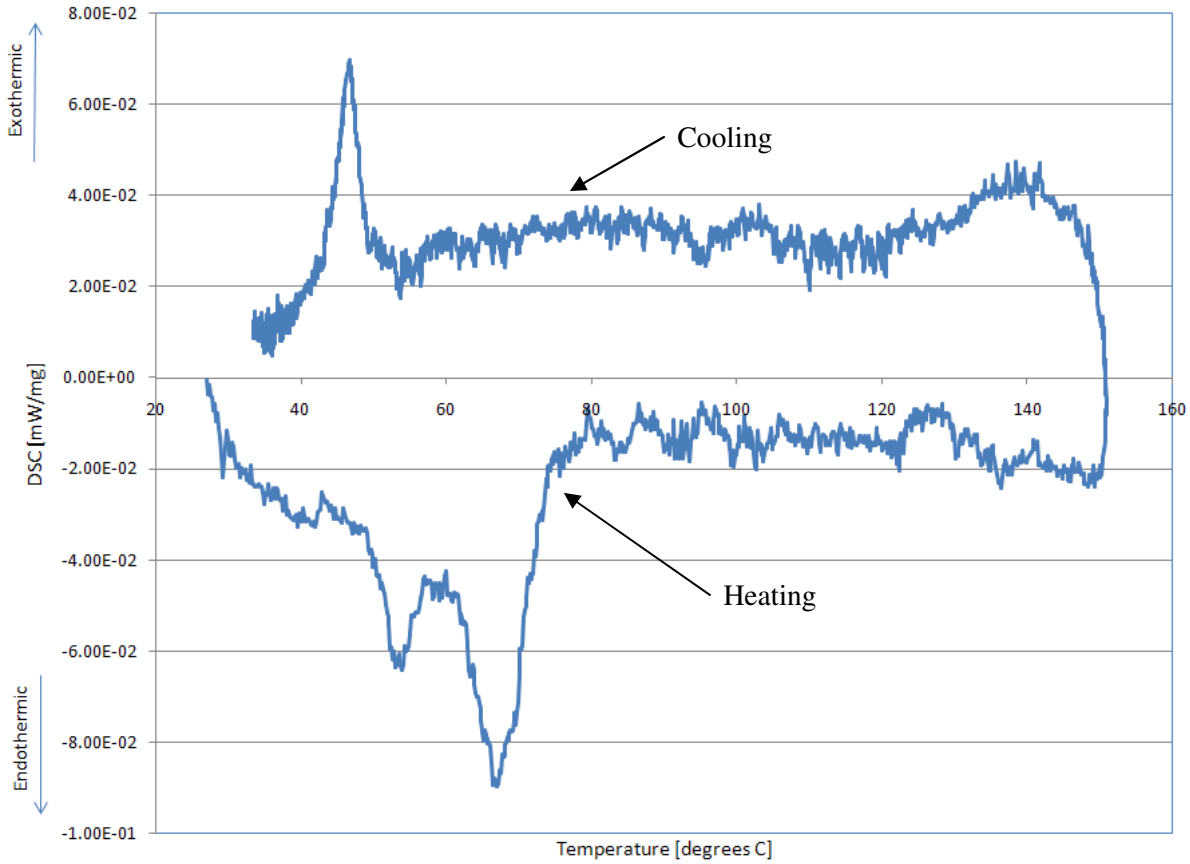

Figure 54: DSC curves for annealed SM495 material

Two distinct peaks are present on the heating portion of the DSC scan. The smaller first peak represents the martensite to R-phase transformation, followed by the larger R-phase to austenite transformation. Upon cooling only one peak is observed. This peak could represent the austenite to martensite transformation, but may also represent the austenite to R-phase transformation. The DSC was unable to obtain data below room temperature where the second cooling peak may exist.

Table 9: Transformation temperatures of SM495 material

Transformation	Temperature [^{o}C]
Austenite Start (A_s)	49
Austenite Finish (A_f)	75
Martensite Start (M_s)	50
Martensite Finish (M_f)*	40

*M_f value may only represent the finish of the Austenite to R-phase transformation. The R-phase to Martensite transformation may occur below the temperature limits of DSC.

5.2.2 Modeling and Design Data

Utilizing the data obtained in the previous section, material properties for both the superelastic and SMA material were determined and implemented into the FEM developed in Chapter 4. The FEM was then used to develop force displacement data under bending conditions in order to determine the final dimensions for the prototype SMA actuator.

5.2.2.1 FEM Material Parameters

The stress-strain curves illustrated in Figure 52 and Figure 53 provided the necessary data for determining the various elastic moduli of the piece-wise continuous curves used to model the SMA material. Transformation temperatures were obtained directly from the DSC results in Figure 54 and Table 9. The material parameters implemented in the FE model are summarized below in Table 10.

Table 10: FEM material parameters derived from experimental results

Parameter	Value	Units
SM495	**SM495**	**SM495**
E_m	13.17	Gpa
E_{mt}	301.78	Mpa
E_a	27.33	Gpa
E_{am}	2.93	Gpa
ϵ_y^m	0.00855	mm/mm
ϵ_d^m	0.0527	mm/mm
ϵ^{Ms}	0.019	mm/mm
SE508	**SE508**	**SE508**
E_a	35.65	Gpa
E_{am}	1.1	Gpa
ϵ^{Ms}	0.0091	mm/mm

5.2.2.2 Bending Design Curves

Using the FE modeling technique developed in Chapter 4, in conjunction with the material parameters in Table 10, the complex bending behaviour of the SMA material was simulated using only information determined from standard tensile tests. It should be noted that the model assumed the stress-strain behaviour in compression was the same as in tension. Bending simulations were performed using the dimensions and material properties of the available NiTi ribbon (SM495 and SE508). A beam length of 30 mm was used in all simulations in order to maintain comparability to the monolithic actuator developed by Toews [4]. An incremental perpendicular load was applied to one end of the beam and the other remained fixed as illustrated in Figure 55.

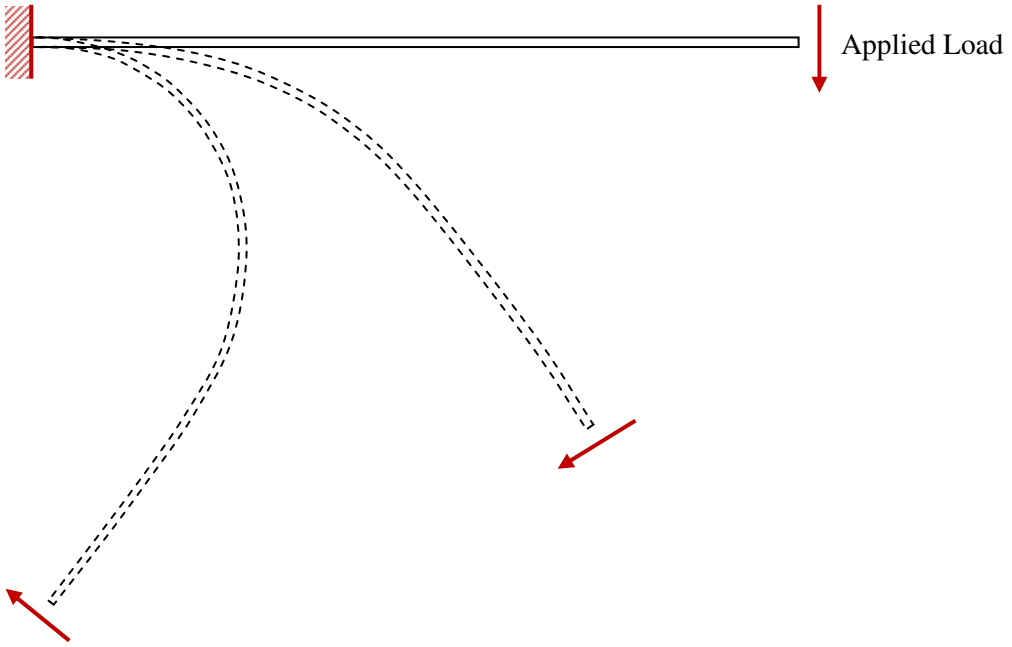

Figure 55: Beam simulation setup

The simulation data was used to obtain force versus tip deflection curves for the superelastic material (SE508), as well as both high and low temperature curves for the SMA material (SM495). Similar to the spring-biased actuator design presented in Section 2.7, the bending of the superelastic member acted as the restoring medium to reset the SMA material. The design is presented in Figure 56. The superelastic beam is annealed in a curved position labeled A in Figure 56, while the SMA beam is annealed in a flat position, labeled D. The flat shaded regions of the beams to the left are fixed to a stationary base, while the opposite ends (labeled A and D) are attached together. The beams then deform to an equilibrium position as defined by the force-displacement curves simulated previously. When the SMA is in its low temperature martensite state, the equilibrium position is defined by B and when heated to its high temperature austenite state the equilibrium position is defined by C in Figure 56. As the SMA is cycled between its martensite and austenite states, the

stiffness of the beam changes, thus changing the equilibrium position and providing cyclic actuator motion between positions B and C.

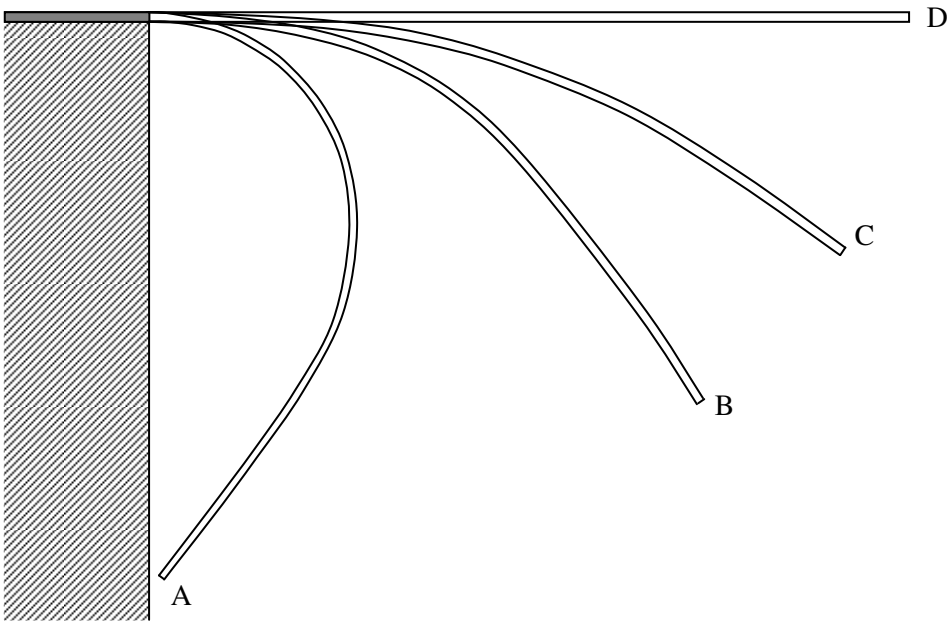

Figure 56: Bending actuator design

5.2.3 Final Prototype Design

The data obtained from the beam simulations described in the previous section were used to plot force versus displacement curves for the two alloys and their various states. Figure 57 plots the tip displacement along the y-axis versus the tangential tip load as illustrated in Figure 56 previously. The plot shows the behaviour of the SMA beam in both its martensite and austenite states deformed from its horizontal position, as defined by position D in Figure 56. The behaviour of the superelastic material is plotted as an opposition force as deformed from its curved annealed position, as defined by position A in Figure 56.

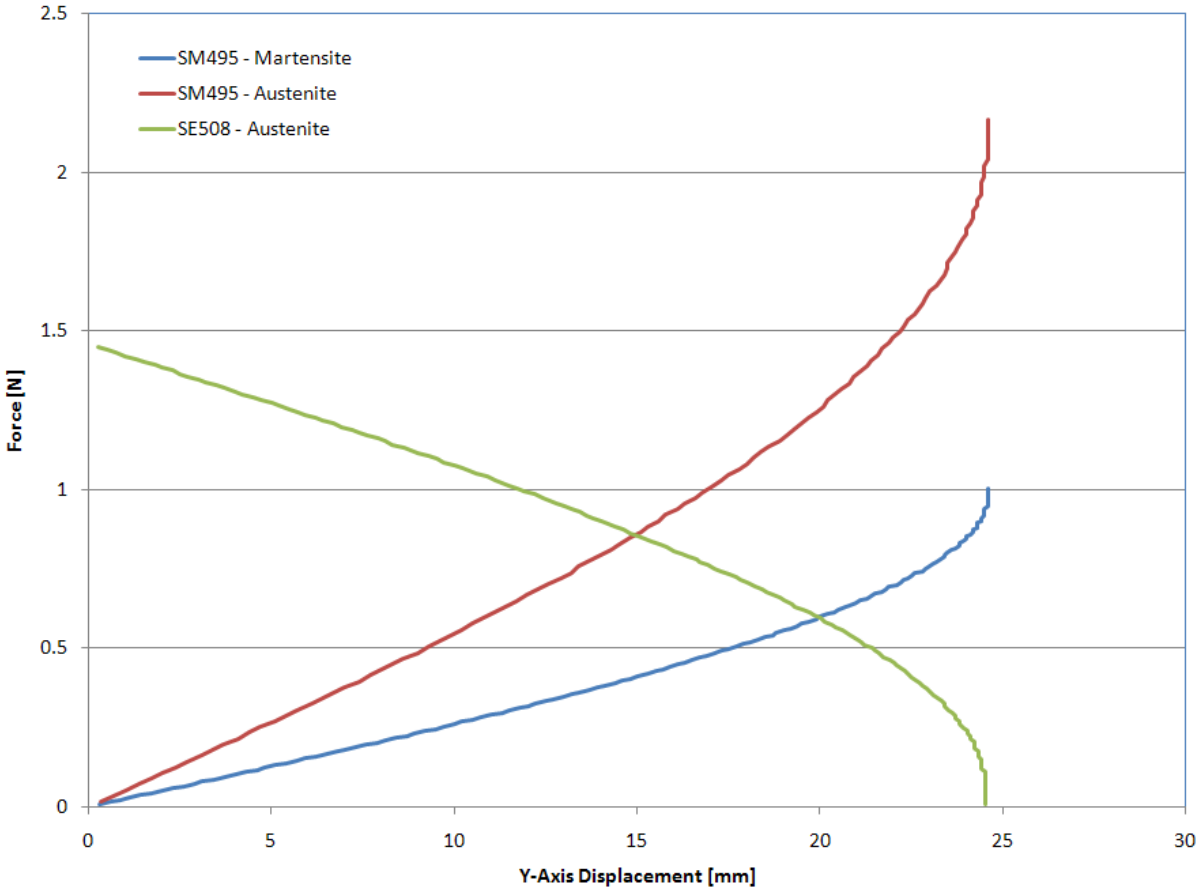

Figure 57: Y-axis tip deflection versus tip load (SM485 width = 14 mm; SE508 width = 2 mm)

The force versus displacement data provided by the FE simulations was performed in two dimensions for a given beam length and thickness. The length was chosen as 30 mm, corresponding to the previous monolithic actuator design, and the thickness according to material availability. However, the width of the beams remained a controllable design parameter. Adjusting the width of a beam has the effect of shifting the force up or down for a given displacement. For example, doubling the beam width would double the force value for a given y-axis displacement. Therefore, by varying the width of both the SMA and superelastic beams and referring to their respective force-displacement curves the range of actuation can be controlled.

The force displacement curves in Figure 57 are for a SMA beam width of 14 mm and a superelastic restoring beam of 2 mm. These values were chosen to maximize the range of actuation while remaining within the constraints imposed by the dimensions of the available SMA and superelastic material. Referring to the intersection points on Figure 57, an overall y-axis displacement of approximately 5 mm is predicted. The higher apparent stiffness in the superelastic restoring beam is partially due to the increase in beam thickness in comparison to that of the SMA beam.

Due to the greater thickness of the superelastic beam (SE508) in comparison to that of the SMA beam (SM495) and the inherent increase in bending stiffness, the width of the superelastic beam was much smaller than that of the SMA. Therefore, in contrast to the monolithic actuator design of Toews [4] the centre beam was made the superelastic restoring medium while the outer beams performed the SMA actuation. The symmetrical three beam design is again imposed rather than a two beam design in order to reduce axial twist in the actuator. The final design schematic of the hybrid monolithic actuator prototype is provided in Figure 58. The actuator is shown in its pre-annealed state with the dimensions described above.

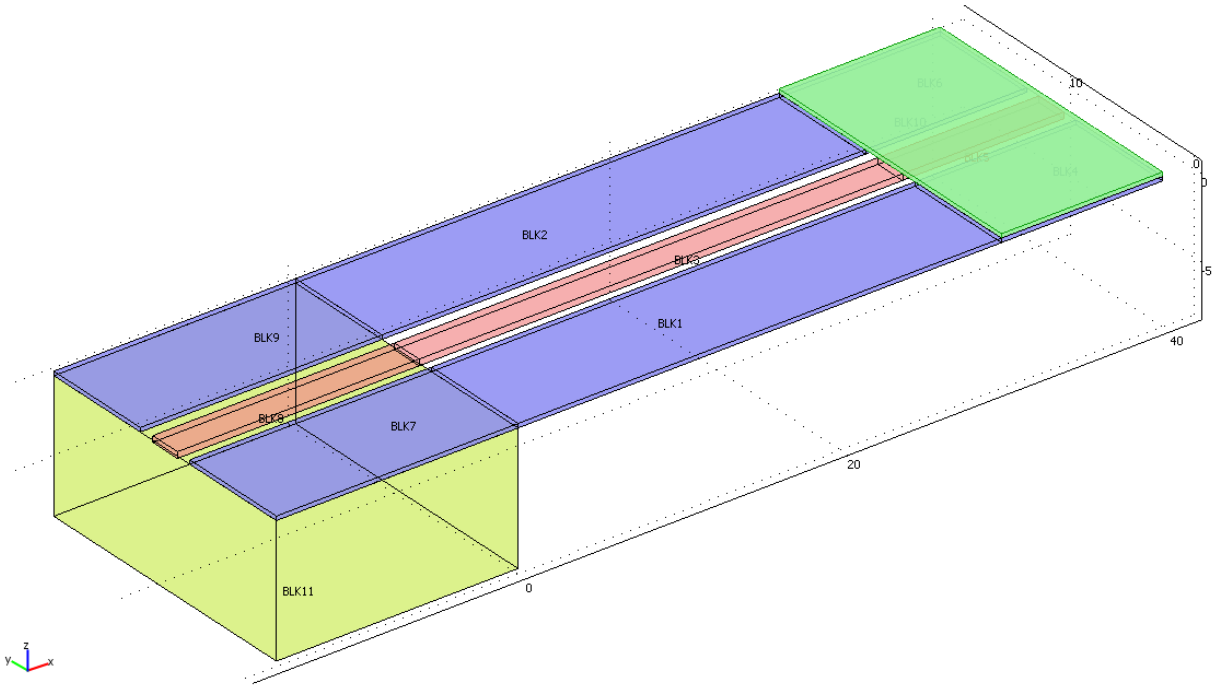

Figure 58: Hybrid monolithic actuator prototype schematic (dimensions in mm)

In Figure 58 the two SMA side beams are shown in blue and the superelastic centre restoring beam in red. Additional length was added to the beams in order to accommodate fabrication and fixation of the beams. The free ends of the beams are attached by a piece of 0.01 inch copper shim (shown in green) and the fixed ends are attached to a stationary base (shown in yellow) both using standard epoxy. The fabrication and annealing process is provided in detail in the following section.

5.3 Prototype Fabrication

5.3.1 Fabrication Procedure

Cutting

The superelastic and SMA beams were cut from the as-received strips SE408 and SM495 respectively, obtained from Nitinol Devices and Components. The beams were cut according to the dimensions chosen in Section 5.2 using a standard shear press. The cut components are shown in Figure 59.

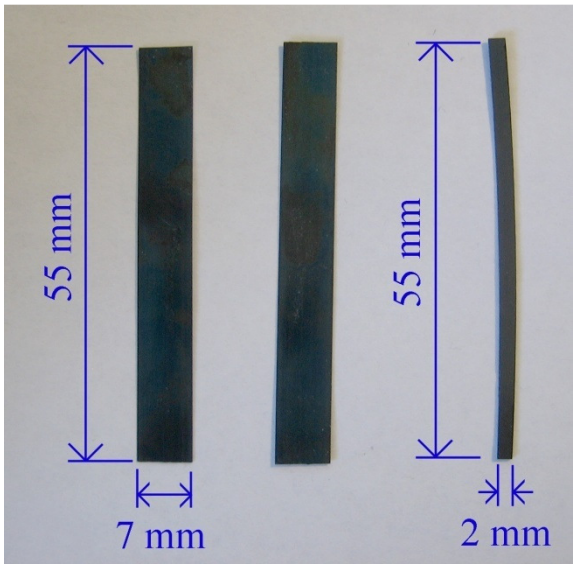

Figure 59: Unassembled prototype beams

Annealing

The beams were annealed in order to undo the effects of any cold working and manufacturing processing, and to set their memorized shapes. The SMA beams were held flat between two blocks and annealed at 500°C for 20 minutes in an air furnace, followed by a water quench. This set the

shape of the SMA beams corresponding to position D in Figure 56. The superelastic restoring beam had to be constrained in the shape corresponding to position A in Figure 56. In order to achieve this it was necessary to design and construct a die capable of holding the beam is the prescribed position during the annealing process.

The curved position labeled A in Figure 56 was based on the natural curve of the superelastic beam when subjected to a tangential tip load. Therefore, rather than undertaking the difficult manufacture of a solid die of this geometry, a free form die design was chosen to facilitate the constrained tangential tip load. Figure 60 illustrates the die design and constrained superelastic beam. The die and constrained beam where annealed at 500^{o}C for 20 minutes in an air furnace, followed by a water quench.

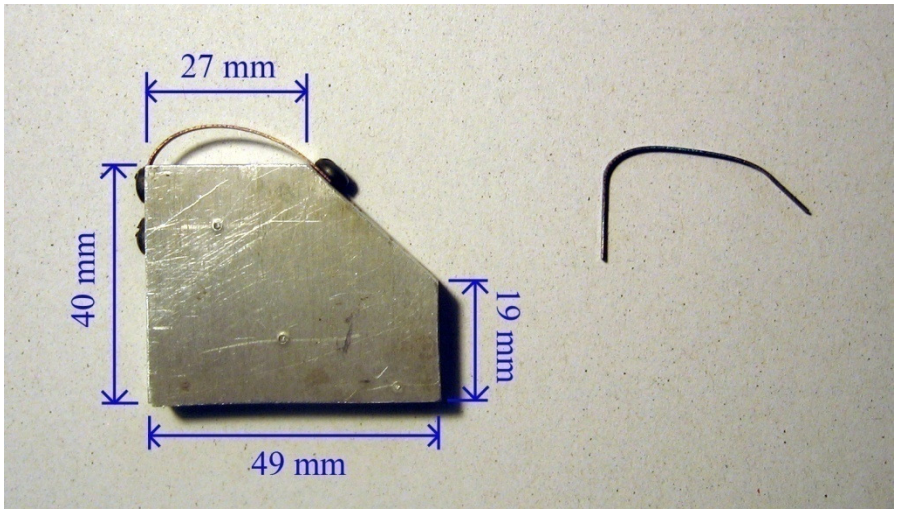

Figure 60: Superelastic beam die design (left) and annealed beam (right)

Several beams were annealed for the construction of several actuators. An annealed superelastic beam is shown in Figure 60. The curvature of the beams was not exactly as desired due

to the design of the free form die. As the material annealed, the stresses were allowed to relax and the curved geometry sagged. It was expected that this would alter the performance of the actuator, however it was believed the actuator would still deliver a measurable performance.

Assembly

The beams were attached at both ends to a strip of 0.01 inch copper shim using standard epoxy. The assembled actuator is shown in Figure 61. Soldering and welding were avoided to prevent the possibility of forming oxides and nitrides that form at elevated temperatures and have been shown to negatively impact the mechanical properties of the alloy. It should be noted that the design of hybrid monolithic actuators specifically aims to eliminate the necessity of mechanical attachment. However, the prototype presented here is developed in order to obtain range of motion predictions of future hybrid actuators.

Figure 61: Assembled prototype actuator

5.3.2 Prototype Performance

The assembled prototype was mounted at one end as illustrated in Figure 61, with the free end able to achieve cyclic deflection upon temperature cycling. A rig was created to mount the actuator and apply an external heat source capable of elevating the temperature of both SMA beams above their austenite transformation temperatures. The rig shown in Figure 62 utilized a Joule heated Nichrome wire below the actuator to apply activation heat. A side mounted fan was used to increase the rate of cooling, thus increasing the bandwidth of the prototype actuation during experiments.

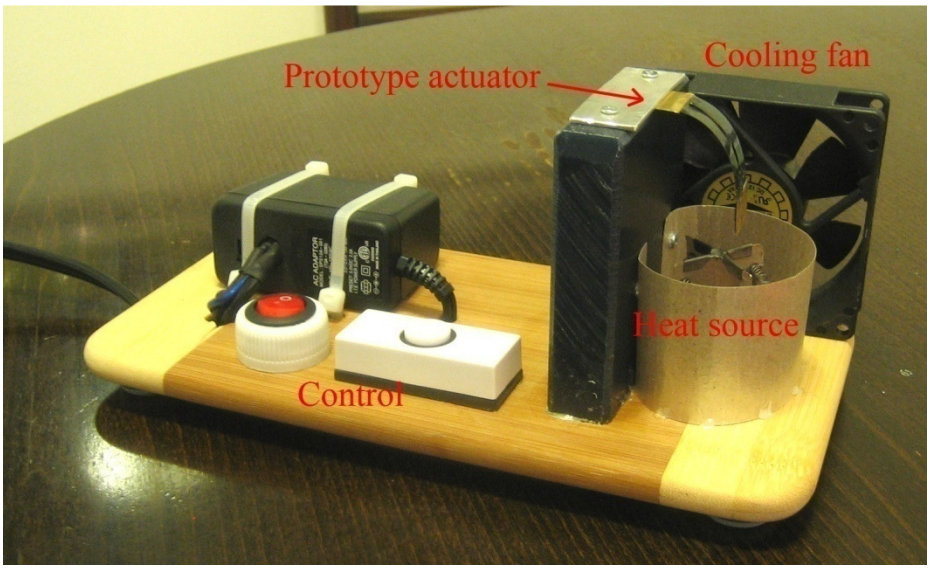

Figure 62: Prototype actuator experimental rig

The performance of the prototype actuator was measured visually in terms of tip displacement while subjected to various tip loads. Photographs of the actuator in both its martensite and austenite states were taken in front of a displacement reference, and deflection measurements were obtained using digital measurement software. An example measurement is illustrated in Figure

63 below. Typically actuators operate under some external load. Therefore, tip loads were applied to the free end of the actuator and the above tip displacement measurements were repeated. The tip deflection results are summarized in Figure 64 for the loaded actuator. The unloaded actuator was able to deliver a repeatable 18 mm horizontal and 14 mm vertical tip deflection.

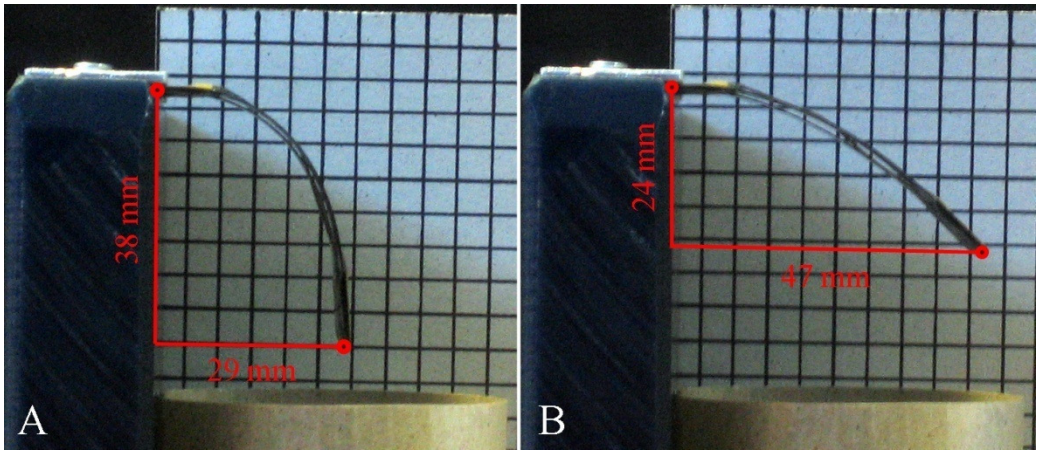

Figure 63: Prototype actuator tip deflection measurements. A – low temperature; B – high temperature.

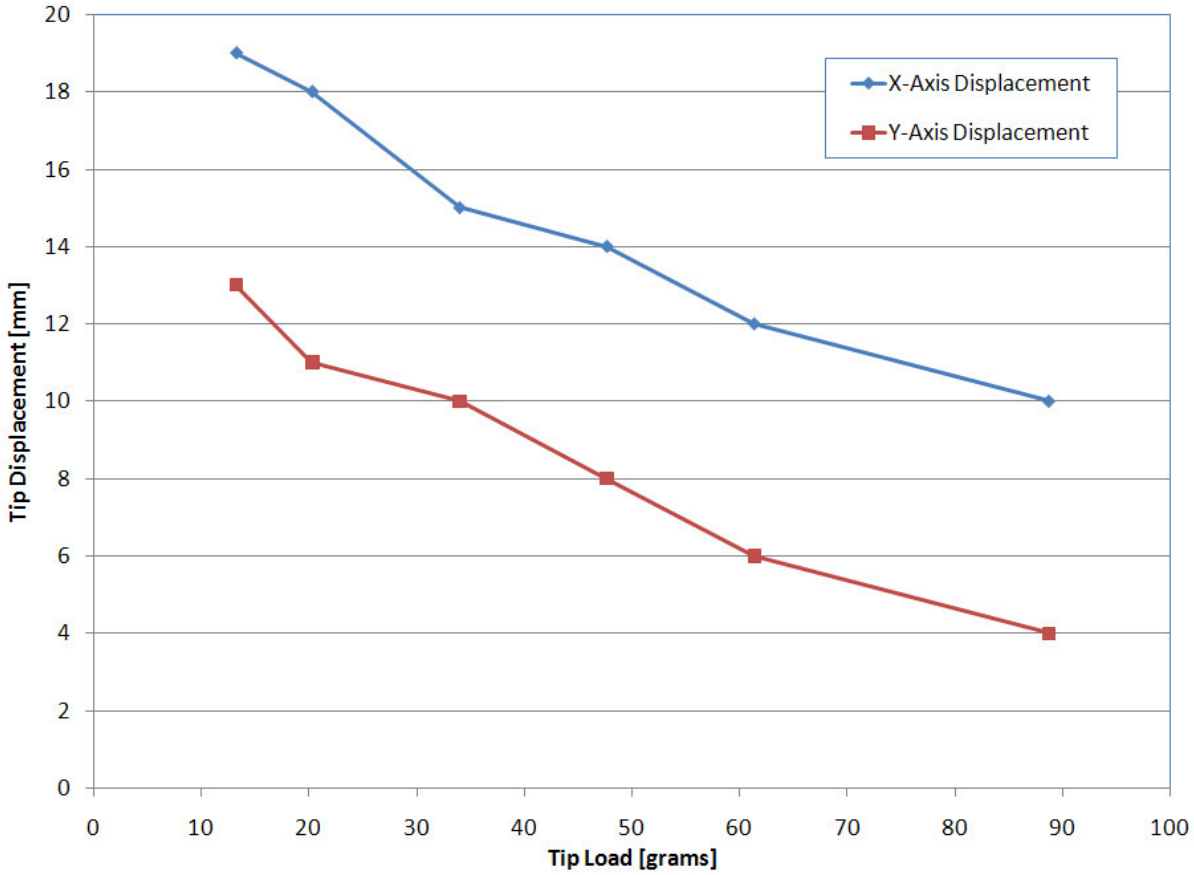

Figure 64: Loaded actuator tip deflection

5.3.2.1 Comparison to Model Predictions

The tip deflection achieved by the prototype actuator was much larger than the predictions made by the FEM simulations. The predicted vertical deflection of 5 mm was surpassed by an actual deflection of 14 mm. From a performance perspective these results are encouraging, however, from a design perspective a 280 percent error occurred.

5.3.2.2 Error Analysis

Several assumptions were made in the development of the FE model that likely contributed to the observed error. First, the material properties obtained for the SMA and superelastic alloys in Section 5.2.1.1 were all obtained in tension. These properties where then used as material parameters in the FE model. Of particular interest were the elastic and shear moduli for each of the piece-wise continuous segments. Since shear and compression data was not available for the SMA and superelastic alloys, it was assumed that all moduli were equal to those obtained in tension. However, referring to Figure 65 it is clear that this is not a valid assumption. More rigorous material characterization could help rectify this assumption and eliminate possible error.

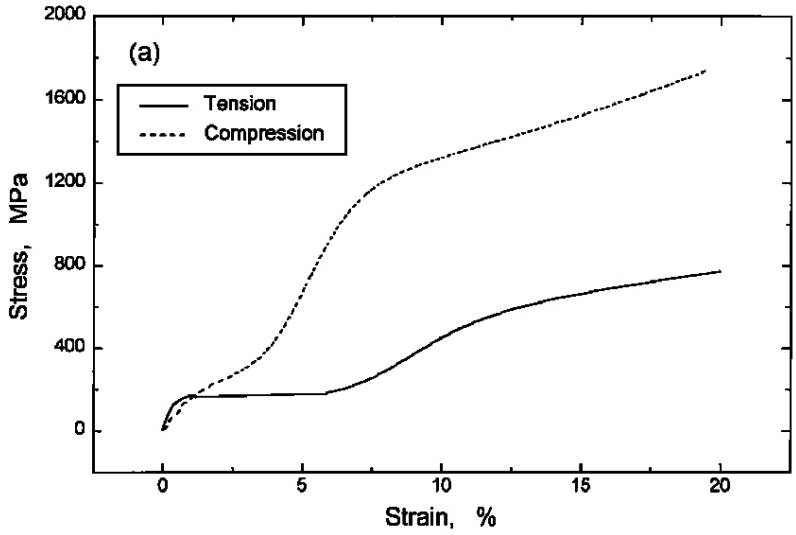

Figure 65: Stress-strain curves of NiTi SMA under tension and compression [54]

Secondly, the method used to obtain the high temperature SMA tensile data was prone to error. Available equipment made it difficult to accurately maintain and measure temperature during the tensile tests of the SM495 specimens, as described in Section 5.2.1.1. Maintaining a consistent

flow of hot air and the heat-sinking effect of the large specimen jaws contributed to the difficulty in maintaining a constant temperature. Therefore, the temperature for which the tensile data was obtained remains approximate. Since it is known that the properties of superelastic materials are highly dependent on temperature, as shown in Figure 66, it is reasonable to believe this contributed to the modeling error.

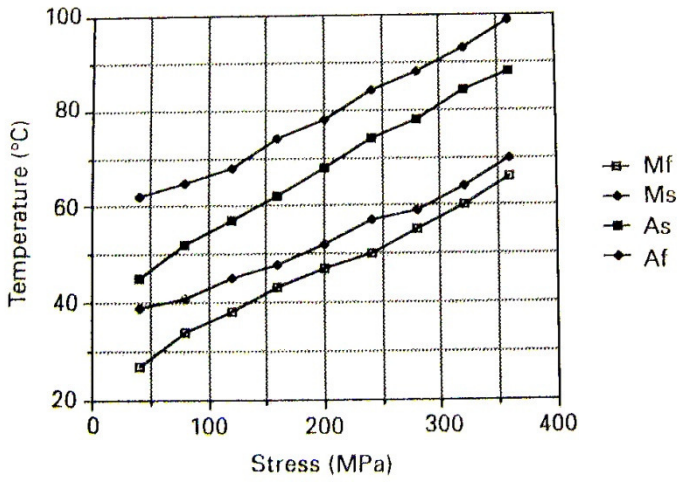

Figure 66: Stress-temperature dependence of transformation temperatures in NiTi [6]

Finally, all modeling assumed uniform temperature distribution throughout the actuator. However, due to the design of the test rig and method of heat application a uniform temperature distribution likely did not exist, again contributing to the modeling error.

Chapter 6

Conclusions

This research introduced the concept of hybrid monolithic shape memory alloy (SMA) actuators, including their fabrication, design, and performance. Hybrid monolithic actuators offer all the advantages of monolithic actuators while eliminating some of their disadvantages. Monolithic actuators can be difficult and expensive to machine from bulk material, are difficult to locally anneal as thermal control becomes increasingly difficult at smaller scales, and have a minimal range of motion restricted by the properties of the non-annealed restoring medium. Hybrid design, which incorporates varying material compositions within a single monolithic component, is capable of overcoming these limitations.

Powder metallurgy tape casting fabrication techniques are capable of forming large-area, flat sheets that can be cut, stacked and pressed to form complex planar geometries. The introduction of sheets with varying compositions and materials provides a controllable method of manufacturing monolithic actuators with non-uniform, or hybrid, compositions. NiTi tape recipes and sintering profiles were developed, and their resulting specimens analyzed. A high degree of NiTi homogeneity and up to 90 percent dense components were observed using the scanning electron microscope. However, the NiTi exhibited no observable shape memory or superelastic effect above room temperature and had poor mechanical properties. These results provide the first steps towards integrating shape memory and superelastic tapes into a single hybrid component.

Designing hybrid monolithic actuators with complex geometries necessitated the development of a new design tool. A previously developed lumped-element model was modified for

implementation into a finite element solver. The lumped-element model, coded as a series of Matlab functions, was integrated into the COMSOL Multiphysics finite element (FE) environment. The SMA FE model was validated, and used to design and predict the performance of a prototype hybrid actuator.

The prototype hybrid monolithic actuator was designed based on a previous monolithic actuator with the intent of illustrating the advantages of hybrid design. Since the powder metallurgy techniques were not yet capable of producing NiTi with good performance characteristics, the hybrid actuator was built using commercially available SMA ribbon and standard joining techniques. The mechanical properties of the commercially available SMA were obtained and used within the FE model to design a three-beam out-of-plane bending actuator. The prototype hybrid actuator displayed tip deflections several orders of magnitude larger than those achieved by a previously developed monolithic actuator with similar overall dimensions and without the need of local annealing. These results are promising from a performance perspective, however, the range of motion did not agree well with FE predicted performance. Several sources of error did exist that contributed to the inaccuracy, yet despite this, the modeling technique provided a prototype with excellent performance.

Bibliography

[1] A. Menciassi, A. Moglia, S. Gorini, G. Pernorio, C. Stefanini, P. Dario, "Shape memory alloy clamping devices of a capsule for monitoring tasks in the gastrointesyinal tract," Journal of Micromechanics and Microengineering, vol. 15, pp. 2045-2055, 2005.

[2] A. Menciassi, C. Stefanini, S. Gorini, G. Pernorio, B. Kim, J. O. Park, P. Dario, "Locomotion of a Legged Capsule in the Gastrointestinal Tract: Theoretical Study and Preliminary Technological Results," Proceedings of the 26th Annual Internation Conference of the IEEE EMBS, San Francisco, 2004.

[3] Y. Bellouard, T. Lehnert, J. E. Bidaux, T. Sidler, R. Clavel, R. Gotthardt, "Local annealing of complex mechanical devices: a new approach for developing monolithic micro-devices," Materials Science and Engineering, pp. 795-798, 1999.

[4] L. M. Toews, "The development of a monolithic shape memory alloy actuator," Thesis, Electrical and Computer Engineering, University of Waterloo, Waterloo, 2004.

[5] Hirose et al., VSP, 1989.

[6] T. W. Duerig, K. N. Melton, D. Stockel, C. M. Wayman, Engineering Aspects of Shape Memory Alloys, Butterworth-Heinemann, 1990.

[7] M. Es-Souni, M. Es-souni, H. Fischer-Brandies, "Assessing the biocompatibility of NiTi shape memory alloys used for medical applications," Anal Bioanal Chem, vol. 381, pp. 557-567, 2005.

[8] M. H. Wu, Memry Corporation, "Fabrication of Nitinol Materials and Components," Proceedings of the International Conference on Shape Memory and Superelastic Technologies. Kunming, China, pp. 285-292, 2001.

[9] D. A. Miller, D. C. Lagoudas, "Influence of cold work and heat treatment on the shape memory effect and plastic strain development of NiTi," Materials Science and Engineering, vol. 308, pp. 161-175, 2001.

[10] N. Zhang, P. B. Khosrovabadi, J. H. Lindenhovius, B. H. Kolster, "TiNi shape memory alloys prepared by normal sintering," Materials Science and Engineering, vol. 150, pp. 263-270, 1992.

[11] J. A. Shaw, S. Kyriakides, "Thermomechanical aspects of NiTi," J. Mech. Phys. Solids, vol. 43, no. 8, pp. 1243-1281, 1995.

[12] Memry Corporation, “Wire Spec Sheet,” Available at http://www.memry.com/productsservices/pdfs/wirespec.pdf (accessed January 2007).

[13] J. A. Shaw, "A thermomechanical model for a 1-d shape memory alloy wire with propagation instabilities," International Journal of Solids and Structures, vol. 39, pp. 1275-1305, 2002.

[14] A. D. Johnson, V. V. Martynov, Proceedings, International Conference on Shape Memory and Superelastic Technologies, Pacific Grove, California, pp. 149, 1997.

[15] J. Peirs, D. Reynaerts, H. Van Brussel, "Shape memory micro-actuators for medical purposes," Proceedings of the International Conference on Advanced Robotics, pp. 155-160, 1997.

[16] M. Barrabes, P. Sevilla, J. A. Planell, F. J. Gil, "Mechanical properties of nickel-titanium foams for reconstructive orthopaedics," Materials Science and Engineering, vol. 28, pp. 23-27, 2008.

[17] W. A. Johnson, J. A. Domingue, S. H. Reichman, J. de Physique,Coll. C4, Tome 42, Supp. 12, p. C4-285, 1992.

[18] D. E. Aslanisdis, Proceedings, International Conference on Shape Memory and Superelasticity Technologies, Antwerp, Belgium, 1999.

[19] Y. Suzuki, K. Yamauchi, K. Suzuki, K. Tabei, T. Katoh, K. Kusaka, J. Kobayashi, Proceedings, International Symposium on Shape Memory Alloys, Guilin, China, pp. 405, 1986.

[20] D. Goldstein, "Production of Shaped Parts of Nitinol Alloys by Solid State Sintering," Report NSWC TR 84-326, Naval Surface Weapons Center, 1986.

[21] V. I. Itin, V. E. Gynter, S. A. Shabalovskaya, R. L. C. Sachdeva, Mater. Characterization, vol. 32, pp. 179, 1994.

[22] E. Schuller, O. A. Hamed, M. Bram, D. Sebold, H. P. Buchkremer, D. Stover. "Hot Isostatic Pressing (HIP) of Elemental Powder Mixtures and Prealloyed Powder for NiTi Shape Memory Parts," Advanced Engineering Materials, vol. 5, no. 12, pp. 918-924, 2003.

[23] H. Kato, T. Koyari, M. Tokizane, S. Miura, Acta Metall. Mater., vol. 42, no. 1351, 1994.

[24] J. Mentz, M. Bram, H. P. Buchkremer, D. Stover, "Improvements of Mechanical Properties of Powder Metallurgical NiTi Shape Memory Alloys," Advanced Engineering Materials, vol. 8, no. 4, pp. 247-252, 2006.

[25] R. E. Mistler, E. R. Twiname, Tape Casting Theory and Practice, Westerville, Ohio: The American Ceramic Society, 2000.

[26] M. Achenbach, "A model for an alloy with shape memory," International Journal of Plasticity 5, no. 4, pp. 371-395, 1989.

[27] S. Seelecke, I. Muller, "Shape memory alloy actuators in smart structures: Modeling and simulation," Applied Mechanics Review, vol. 57, no. 1, pp. 23-46, 2004.

[28] J. Boyd, D. Lagoudas, "A thermodynamical constitutive model for shape memory materials, Part 1," International Journal of Plasticity, vol. 12, no. 6, pp. 805-842, 1996.

[29] Y. Ivshin, T. J. Pence, "Thermomechanical model for a one variant shape memory material," Journal of Intelligent Materials Systems and Structures, vol. 5, pp. 455-473, 1994.

[30] B. Goo, C. Lexcellent, "Micromechanics-based modeling of two-way memory effect of a single crystalline shape memory alloy," Acta Materialia, vol. 45, no. 2, pp. 727-737, 1997.

[31] F. Preisach, "Uber die magnetische Nachwirkung," Zeitschrift fuer Physik, vol. 94, pp. 277-302, 1935.

[32] K. Tanaka, S. Kobayashi, Y. Sato, "Thermomechanics of transformation, pseudoelasticity and shape memory effect in alloys," International Journal of Plasticity, vol. 2, no. 11, pp. 59-72, 1986.

[33] C. Laing, C. A. Rogers, "One-dimensional thermomechanical constitutive relations for shape memory materials," Journal of Intelligent Material Systems and Structures, vol. 8, no. 4, pp. 285-302, 1997.

[34] L. C. Brinson, "One-dimensional constitutive behaviour of shape memory alloys: thermomechanical derivation with non-constant material functions and redefined martensite internal variable," Journal of Intelligent Materials Systems and Structures, vol. 4, no. 2, pp. 229-242, 1993.

[35] K. Ikuta, M. Tsukamoto, S. Hirose, "Mathematical model and experimental verification of shape memory alloy for designing micro actuator," Proceedings of IEEE MEMS, Nara, Japan, pp. 103-108, 1991.

[36] D. Madill, D. Wang, "Modeling and L2-stability of a shape memory alloy position control system," IEEE Trans. Control Systems Technology, vol. 6, no. 4, pp. 473-481, 1998.

[37] A. Pai, R. B. Gorbet, "Extension of Madill's SMA model to include time-varying stress," Proceedings of International Workshop Smart Materials and Structures (Cansmart), Toronto, Canada, 2006.

[38] A. Pai, "A phenomenological model of shape memory alloys including time-varying stress," Thesis, Electrical and Computer Engineering, University of Waterloo, Waterloo, 2007.

[39] L. C. Brinson, R. Lammering, "Finite element analysis of the behavior of shape memory alloys and their applications," Int. J. of Solids Structures, vol. 30, no. 23, pp. 3261-3280, 1993.

[40] M. L. Boubakar, S. Moyne, C. Lexcellent, P. Boisse, "SMA pseudoelastic finite strains: Theory and numerical application," ASME J. of Engineering Materials and Technology, vol. 121, pp. 44-47, 1999.

[41] F. Trochu, Y. Y. Qian, "Nonlinear finite element simulation of superelastic shape memory alloy parts," Computers and Structures, vol. 62, no. 5, pp. 799-810, 1997.

[42] B. Peultier, T. Ben Zineb, E. Patoor, "Macroscopic constitutive law for SMA: Application to structure analysis by FEM," Materials Science and Engineering, pp. 454-458, 2006.

[43] X. M. Wang, Z. F. Yue, "FEM prediction of the pseudoelastic behavior of NiTi SMA at different temperatures with one temperature testing results," Computational Materials Science, vol. 39, pp. 697-704, 2007.

[44] H. Zhang, Y. Bellouard, T. Sidler, E. Burdet, A. Poo, R. Clavel, "A monolithic shape memory alloy microgripper for 3-D assembly of tissue engineering scaffolds," Proceedings of SPIE, pp. 50-60, 2001.

[45] M. A. Whitney, "A study of the sintering behaviour of Ni-Ti powder compacts using differential scanning calorimetry," Thesis, Mechanical Engineering, University of Waterloo, Waterloo, 2008.

[46] C. L. Yeh, W. Y. Sung, "Synthesis of NiTi intermetallics by self-propagating combustion," Journal of Alloys and Compounds, vol. 376, pp. 79-88, 2004.

[47] B. Y. Li, L. J. Rong, Y. Y. Li, V. E. Gjunter, "Synthesis of porous Ni-Ti shape-memory alloys by self-propagating high-temperature synthesis: Reaction mechanism and anisotrophy in pore structure," Acta Materialia, vol. 48, no. 15, pp. 3895-3904, 2000.

[48] B. Bertheville, M. Neudenberger, J. E. Bidaux, "Powder sintering and shape-memory behaviour of NiTi compacts synthesized from Ni and TiH_2," Materials Science and Engineering, vol. 384, pp. 143-150, 2004.

[49] B. Bertheville. "Porous single-phase NiTi processed under Ca reducing vapor for use as a bone graft substitute," Biomaterials, vol. 27, pp. 1246-1250, 2006.

[50] COMSOL, "COMSOL Multiphysics Modeling Guide Version 3.3," 2006.

[51] M. M. Ghomshei, A. Khajepour, N. Tabandeh, K. Behdinan, "Finite element modeling of shape memory alloy composite actuators: theory and experiment," Journal of Intelligent Material Systems and Structures, vol. 12, pp. 761-773, 2001.

[52] www.matweb.com.

[53] Memry Corporation, “Nitinol FAQ,” Available at http://www.memry.com/nitinolfaq/nitinolfaq.html (accessed January 2007).

[54] Y. Liu, Z. Zie, J. Van Humbeeck, L. Delaey, “Asymmetry of stress-strain curves under tension and compression for NiTi shape memory alloys,” Acta mater., vol. 46, no. 12, pp. 4325-4338, 1998.